Simultaneous PIV and balance measurements on a pitching aerofoil

M. Klein Heerenbrink

May 30, 2011

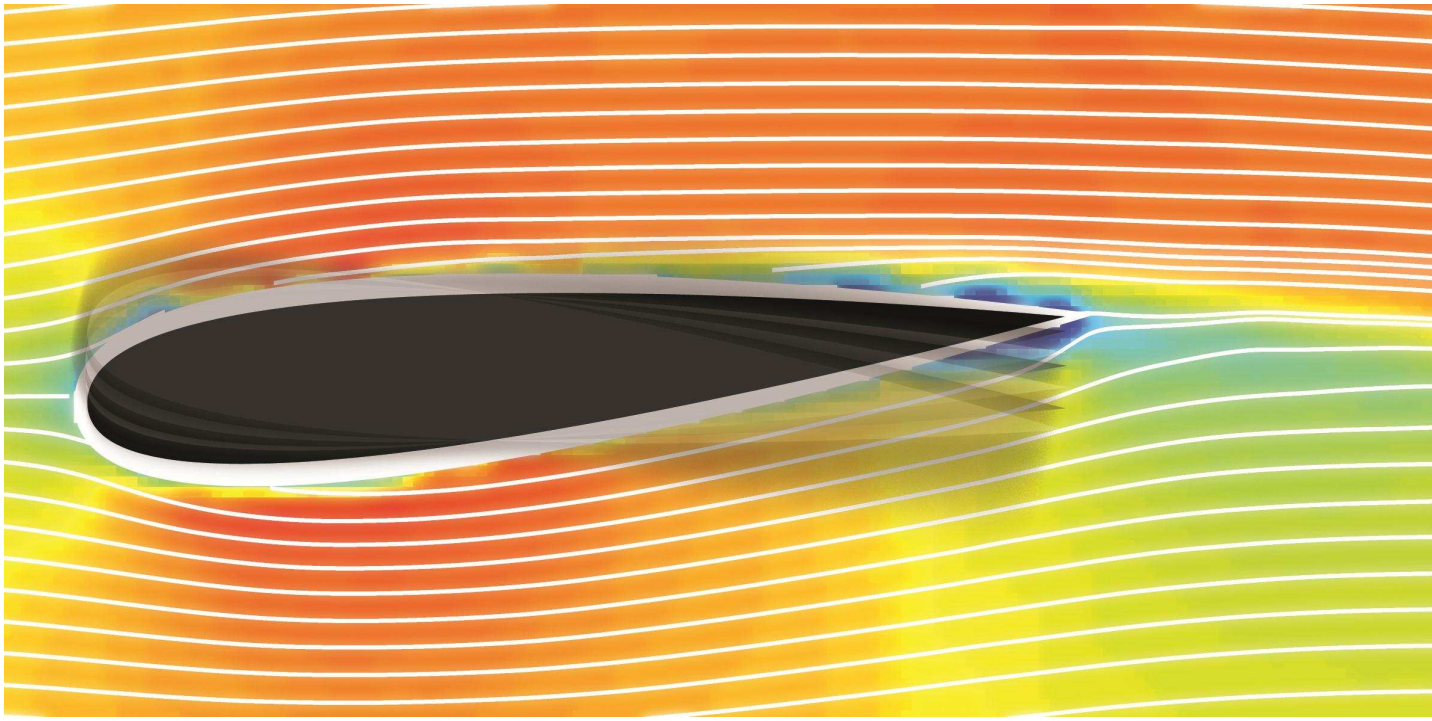

Master of Science Thesis

Faculty of Aerospace Engineering · Delft University of Technology

Simultaneous PIV and balance measurements on a pitching aerofoil

Master of Science Thesis

For obtaining the degree of Master of Science in Aerospace Engineering at Delft University of Technology

M. Klein Heerenbrink

May 30, 2011

Faculty of Aerospace Engineering · Delft University of Technology

Delft University of Technology

Delft University Of Technology
Department Of
Aerodynamics

The undersigned hereby certify that they have read and recommend to the Faculty of Aerospace Engineering for acceptance a thesis entitled **"Simultaneous PIV and balance measurements on a pitching aerofoil"** by **M. Klein Heerenbrink** in partial fulfillment of the requirements for the degree of **Master of Science**.

Dated: May 30, 2011

Exam Committee :

prof.dr. F. Scarano

:

dr.ir. B. W. van Oudheusden

:

ir. R. de Kat

:

ir. E. G. M. Geurts (NLR)

Abstract

Unsteady aerodynamics deals with air flows that can not be sufficiently described without considering the time dependence of the flow. Unsteady flow phenomena are encountered with wind turbines, helicopter rotors and aeroplane propellers. It is also an important factor in the study of animal flight, with birds, bats and insects flapping to produce lift and propulsion. Recently also micro aerial vehicles (MAV's) have been constructed that use those same mechanisms for flight.

With the availability of high-speed particle image velocimetry (PIV) systems, it is now possible to quantitatively measure unsteady flow fields in a time-resolved manner. Methods have been developed that enable to determine the unsteady aerodynamic forces on an object from the measured flow velocity field around it, using a control volume approach. For steady flows, these methods have been extensively validated previously by comparison to balance measurements. For unsteady flows, however, such a validation has not been made before. The present thesis investigation involves an experimental study of an aerofoil subjected to an oscillating pitch motion. Unsteady loads were determined from instantaneous velocity fields, that were obtained using a high-speed PIV system. Additionally it has been attempted to validate these loads by means of force balance measurements.

The experimental set-up involved an actuated sinusoidally pitching aerofoil, with a NACA0018 profile. Eight strain-gauge bending-beam sensors formed a balance for the mechanical reference force measurements. With a PIV system, consisting of 4 high speed cameras, with partially overlapping fields-of-view, and a high speed laser, time-resolved velocity data was obtained in the cross-sectional plane of the aerofoil. Reynolds numbers near 80 000 and pitch frequencies of 10 and 20 Hz were investigated.

The forces obtained from PIV agreed well with the balance data for the static cases. For the oscillating cases, they were comparable to those predicted using Theodorsen's theory. The latter, a solution of the potential flow problem for a harmonically pitching and heaving flat plate, is an often used prediction method for unsteady aerofoil problems. The similarity between the PIV results and Theodorsen's method, supports the credibility of the PIV results.

The balance measurements were less successful for the aerofoil pitching at high frequencies. They suffered from the actuation forces and resonance with higher frequencies present in the aerofoil motion. This meant that many corrections had to be applied, which were based on estimations of the mechanical properties of the set-up.

Preface

This report describes the experimental investigation of a pitching aerofoil, more specifically about obtaining the aerodynamic forces on such an aerofoil. The study was conducted as part of my graduation project at the chair of Aerodynamics of the Department of Aerospace Engineering at Delft University of Technology (TU Delft).

I would like to express my gratitude first of all to my supervisors Roeland de Kat and Bas van Oudheusden for their advice and support. Special thanks to Robbie Stevens, from Queens University, with whom I conducted the wind tunnel experiments involving the PIV measurements. Thanks also to Rob van der List, Ed Roessen and Peter den Dulk for their advise and constructing of the set-up, and Jos van Driel from the MeetShop (3mE), for his advise on sensors. I would also like to thank Andrea Nati and Joost Sterenborg for sharing their experience on moving aerofoils. I like to thank the technical staff of the high speed lab., Eric de Keizer, Frits Donker Duyvis, Peter Duyndam and Nico van Beek for their assistance with the wind tunnel, electronics and last minute modifications of parts of the set-up. And not to be forgotten all the Masters students from the basement of the high speed laboratory.

Last, but certainly not least, I would like to thank my parents for their support, my brother for the elaborate discussions on the back of paper beermats and my friends for providing the possibilities for distractions every now and then.

Marco Klein Heerenbrink
Delft, May 16, 2011

Contents

List of Figures

List of Tables

Nomenclature

Latin Symbols

b	Half chord (as conventional in aeroelasticity), $b = c/2$	[m]
b	Wing span	[m]
$C(k)$	Theodorson's function or circulation function	$[-]$
c	aerofoil chord	$[m]$
$C_{L(D)}$	Lift (or drag) coefficient $L(D)/\rho V^2 S$	[-]
C_ℓ	Sectional lift coefficient $\ell/\rho V^2 c$	[-]
f	Pitch oscillation frequency	[Hz]
k	reduced frequency $\frac{\omega c}{2U}$, which is the ratio of periods for oscilation and wake convection	$[-]$
k	spring stiffness	$[N/m]$
L	Aerodynamic force	$[N]$
ℓ	Sectional lift force	[N/m]
Re	Reynolds number	$[-]$
St	Strouhal number $St = fL/U$	$[-]$

Greek Symbols

α	angle of attack or pitch angle	$[deg]$
κ	tortional spring stiffness	$[Nm]$
ω	angular frequency	$[rad/s]$

θ	pitch angle (equal to angle of attack for parallel freestream flow$[rad] or [deg]$

Abbreviations

(TR-)PIV	Time-Resolved Particle Image Velocimetry
DSV	Dynamic Stall Vortex
FOV	Field of view
MAV	Micro Aerial Vehicle
RMSE	Root Mean Square Error
rms	root-mean-square
TEV	Trailing Edge Vortex

Chapter 1

Introduction

Unsteady aerodynamics is an area of increasing interest. It deals with air-flows that can not be sufficiently described without considering the time dependence of the flow. It has long been important in the field of aeroelasticity, the interaction between the air and structure, where the objective is to identify and predict dangerous situations like flutter, an amplified harmonic response of the wing. For that reason, unsteady aerodynamics is also relevant when designing wind turbines, but even when not considering the distortion of the structure, the rotors of the turbine will likely experience varying flow conditions over the rotation cycle. In conventional wind turbines, with horizontal axis of rotation, when the oncoming air is not perpendicular to the rotor plane, the blades will experience a varying angle of attack through a cycle. For vertical axis wind turbines the varying angle of attack is always present. The rotor blades of helicopters experience a similar varying angle of attack. The pitch angle is actually actively controlled during the cycle, in order to give directional control. More recently, many bio-inspired micro aerial vehicles (MAV's) are being developed. Animals that fly actively, flap their wings in order to generate thrust, so here as well there is unsteady aerodynamics involved.

Time-dependency of the described cases does not have to be significant for the description of the flow. In case the time history of the flow has a marginal contribution to the description of the instantaneous flow, the flow is often called quasi-steady. The flow can than be treated as a steady flow at each separate time instant. Another note on unsteady flows is that a submerged object does not necessarily have to be moving for unsteady effects to appear. A clear example is the singing of wires in the wind. Vortices are shed periodically thereby generating small pressure perturbations that we perceive as sound.

The experiments performed for this project are primarily focused on developing/exploring a method to measure the aerodynamic forces on an aerofoil undergoing a high frequency oscillating pitch motion, simultaneously using a mechanical balance and through time-resolved particle velocimetry ((TR-)PIV). More specifically the aim is to validate forces derived from TR-PIV data using mechanical force measurements. Both methods are already well established tools for determining forces for steady aerodynamic problems. Applying these methods for determining unsteady forces is less well explored, especially

not comparative to each other, as it is in this work. PIV methods are known to give good results for steady flow situations. The most interesting regime will therefore be that of real unsteady flow, where the flow can not be treated as if it were stationary. The project is not so much set out to determine the characteristics of a pitching aerofoil itself, but more to determine how well these characteristics can be quantified using different methods. If one does want to have a reference for a practical application of the experiments, the set-up is most similar to a vertical axis wind turbine.

This report is divided up into several chapters. The next chapter will elaborate on some background information. First an overview of some related studies is given. This is followed by some theory of unsteady aerodynamics, where Theodorsen's function is introduced. Further the general method of deriving forces from a velocity field and the general principles Particle Image Velocimetry is covered. Chapter 3 will present the wind tunnel set-up that was used. Both the physical construction of the set-up and a description of how the experiments were performed. The following chapter, 4, continues this process description, explaining how the obtained raw-data was modified to get to the aerodynamic forces. Then in chapter 5 the obtained results will be presented and discussed. The conclusions of the report can be found in chapter 6. Here an evaluation of the set-up will be provided. Finally chapter 7 will provide recommendations for possible improvements on the current experimental set-up and for further research.

Chapter 2

Background

This chapter will elaborate on underlying theory for unsteady aerodynamics as well as the operating principles of the PIV-based load determination method. First, however, some other studies related to pitching aerofoils are shortly described and compared to the current work. Then section 2.2 elaborates on Theodorsen's function, a solution to an unsteady potential flow problem. This theory is generally used for predicting unsteady forces on harmonically pitching and plunging aerofoils. Section 2.3 explains about the method of deriving the aerodynamic loads on an object submerged in a flow from the velocity field around that object. For obtaining this velocity field experimentally, a method called Particle Image Velocimetry (PIV) is used. The basic principles of PIV are described in section 2.4.

2.1 Similar studies

There have been numerous studies on different shaped objects pitching (and plunging) in a fluid. The following list will shortly mention some of these and elaborate on differences as well as similarities with the current case.

Read [2003] describes a study of thrust generation by a pitching and plunging NACA 0012 foil towed through a water tank, at a Reynolds number of Re $= 4 \times 10^4$. In this study the main parameter is named the Strouhal[1] number based on heave amplitude $\mathrm{St}_{h0} = 2h_0 f/U$, with h_0 the heave amplitude, f the oscillation frequency in s^{-1} (another definition is given, $\mathrm{St}_{h0} = 4\pi h_0 \omega/U$ $(= 8\pi^2 h_0 f/U)$, but this one does not correspond to values provided later) and U the velocity in meters per second. This parameter should be interpreted as the ratio between vortex shedding frequency

[1]Strouhal number St, named after Vincenc Strouhal, who experimented with vortex shedding from wires (wires singing in the wind). It is usually defined as vortex shedding frequency f times a characteristic length L of the obstacle from which the vortices are shed (e.g. wire diameter), divided by the free stream velocity U. This definition is significantly different from the one used by Read [2003].

times the width of the wake and the convecting speed. The maximum obtainable pitch frequency was 1.2 Hz, corresponding to a reduced frequency $k = 0.94$ ($k = \omega c/2U$, based on a chord of 0.1 m and a velocity of 0.4 m/s). The difference between the used form of the Strouhal number and the reduced frequency is essentially the characteristic length scale, repectively the heave amplitude and the chord length. In this research forces are measured mechanically, using piezo-electric sensors. No PIV is used. Essentially different from the current work is that the fluid is water and that the trajectories are much more complex, with pitch angles up to 90°. Due to the use of water, one can work with lower flow speeds, which allow for high reduced frequencies to be obtained with relatively low pitch frequencies.

Panda & Zaman [1994] presents an experimental investigation of the flow field of a sinusoidally pitching NACA0012 aerofoil. The reduced frequencies were in the range $0 \leq k \leq 1.6$ at Reynolds numbers of 22 000 and 44 000. Here the pitching was around the quarter chord axis. Focus is on dynamic stall, attention is paid to the interaction of dynamic stall vortex (DSV) and trailing edge vortex (TEV) which combine in a mushroom like structure shed into the wake. Measurements were performed using hot-wire anemometry and qualitative flow visualisation was achieved with smoke wires.

Rival & Tropea [2010] investigated a pitching and plunging SD7003 aerofoil under dynamic-stall conditions. The aerofoil oscillated with a angular amplitude up to 10° around a centre position of 5° and 10°. The maximum pitch-plunge frequency obtainable for the system was 3 Hz. The experiment involved direct force measurements and (qualitative) flow visualisation. The force measurements were achieved by connecting two one-component Kistler piezo-electric force sensors to the aerofoil (in lift direction). One positioned at the quarter-chord position (pitch axis) and the other at the trailing edge. The motion was controlled by linear motors attached to the force sensors. Both aerodynamic and inertial forces are measured by the sensors, and for higher reduced frequencies ($k > 0.2$) the accuracy of the results deteriorated. Therefore only force data from Reynolds numbers $Re > 60\ 000$ ($U_\infty \approx 7.5$ m/s) was presented. On the other hand the flow visualisation only gave sufficient quality for $Re < 30\ 000$ ($U_\infty \approx 3.75$ m/s). A transition from bluff-body-type to a mushroom-type wake was observed at a reduced frequency $k = 0.2$. With the latter type of wake, a vortex is formed from the leading edge (DSV). This vortex then transports and grows downstream, where it leaves the aerofoil together with a trailing edge vortex. The two vortices are counter rotating, which gives the wake the appearance of a mushroom.

Kang et al. [2009] compares numerical to experimental investigations of a pitching and plunging aerofoil at a reduced frequency of $k = 0.25$ for Reynolds numbers from 10 000 to 60 000. They used a SD7300 aerofoil as well as a 2.3% thickness flat plate aerofoil. The numerical part involved Shear Stress Transport (SST) turbulence closure modelling, using Menter's original definition and a modified version. The experimental part involved Particle Image Velocimetry techniques in two different water tunnel facilities. The pitch motion was described by a 8.42° pitch amplitude around a 8° mean geometric pitch angle. The plunge motion had an amplitude of $0.5c$ and preceded the pitch motion by a quarter cycle period Ol et al. [2009].

Comparing the different methods, a conclusion was that the original SST model performed better for attached flow while the modified SST model resembled the experimental results better in case of separated flow. Besides the comparison of methods, a few other remarks were made considering the flow dynamics. For the blunt aerofoil, SD7300, the pitching and plunging case only has leading edge separation for $Re < 10\ 000$. The pure plunge case always showed leading edge separation. The flat plate aerofoil showed leading edge separation in all cases. Measurements of the lift force showed that both mean as maximum lift increases with Reynolds number. The blunt aerofoil is more susceptible to Reynolds number than the flat plate aerofoil. The maximum lift force is, however, much larger for the flat plate aerofoil.

McCroskey [1982] gives an extensive overview of work done on unsteady aerofoils, both theoretical as experimental. It also shortly mentions the work of Theodorsen, as described in more detail in 2.2 and modifications and extensions of this theory.

Tsang et al. [2008] investigated dynamic stall behaviour on a oscillating NACA 0012 aerofoil, using direct force measurements with piezoelectric load cells. The experiments were carried out at Reynolds numbers of 77 000 with reduced frequencies from 0.005 to 0.04. With a chord of 6 cm and a velocity of 18.8 m/s this corresponds to a maximum frequency of 4 Hz, which is much lower than the intended frequencies in this thesis. The aerofoil was actuated on both sides by servo actuators, to avoid twisting of the aerofoil. The aerofoil was pitched around a mean pitch angle ranging from 0 to 15° with a pitch amplitude of 5° to 10°. Increasing the reduced frequency resulted in an extended hysteresis loop in the lift curve. During the pitch up motion the stall is delayed compared to the static curve as well as to lower reduced frequencies. The recovery from the stall also delays for higher frequencies, i.e. the pitch angle had to be reduced further before the lift curve would return to the static curve values.

Raffel et al. [1995] describes a similar experiment as Tsang et al. [2008], a NACA 0012 aerofoil pitching (and heaving) under deep dynamic stall conditions. In this investigation the instantaneous flow field was measured using PIV, thereby focusing more on the flow structure around the aerofoil. The used system was able to obtain a maximum pitching frequency of 15 Hz, however, it was operated at 6.67 Hz. With a chord of 20 cm and a free-stream velocity of 28 m/s, the Reynolds number was 373 000, which is much higher than the intended Reynolds number in this project, and the reduced frequency 0.15. The aerofoil was pitched around a mean pitch angle of 15° with an amplitude of 10°. This study presented velocity fields with a high spacial resolution, which clearly show the formation of a large separation bubble near the aerofoil surface followed by the shedding of large vortical structures from the leading edge accompanied by separated flow. Comparison between different data sets recorded in successive periods at the same phase angle indicated a strong aperiodicity in the flow (or at least, not at the same frequency as the aerofoil motion).

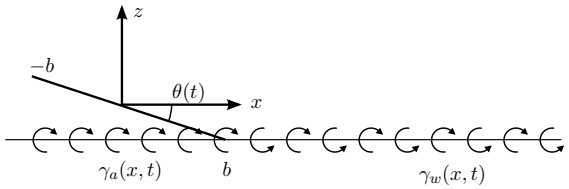

Figure 2.1: Vortex model pitching flat plate

2.2 Theodorsen's function

Aeroelastic problems, like flutter, were reason for studying unsteady aerodynamics as early as the beginning of the 20th century. The first theoretical solutions were formulated in the 1920's. In Theodorsen [1934] expressed a solution to the harmonically pitching aerofoil problem explicitly in terms of Hankel functions. The following theory in this section is taken from the lecture notes of the aeroelasticity course (AE4930, TU Delft) by Hulshoff [2009].

In unsteady aerodynamics the wake behind the aerofoil affects the velocity field near the aerofoil and therefore the forces acting on it. Therefore the entire wake has to be evaluated to get to a solution. A potential flow is linearised and split into a thickness, camber and flat-plate solution. Only the flat-plate solution is time dependent. The other parts can be obtained from the static solution. A linearised model of a pitching flat plate, with a vortex distribution projected on a line parallel to the flow, is shown in figure 2.1. The vorticity on the aerofoil is denoted as $\gamma_a(x,t)$ and the vorticity in the wake as $\gamma_w(x,t)$. The flat-plate solution then needs to satisfy four conditions.

1. zero perturbation in the far field
2. the flow has to be tangent to the aerofoil
3. there can be no pressure jump across the wake
4. Kutta condition using Kelvin's Theorem, $\Gamma(t) = \int_{-b}^{b} \gamma_a(\xi, t)$

The first condition ensures perturbations to vanish far removed from the aerofoil and its wake. The second states that no flow can pass through the aerofoil. These two conditions are also known from steady thin aerofoil theory. The third one is a new requirement arising from having to consider the wake. The wake is free to move, so a pressure difference over the wake can not be sustained. The fourth condition is again a condition known from steady thin aerofoil theory, which ensures the flow separates at the trailing edge of the aerofoil. This condition is required after neglecting viscous forces.

The flow will be modelled by two governing equations, which are forms of the continuity equations for mass and momentum

$$\begin{aligned} \nabla^2\phi &= 0 \\ p - p_\infty &= -\rho_\infty \left(\frac{\partial \phi}{\partial t} + U_\infty \frac{\partial \phi}{\partial x} \right) \end{aligned}$$

The aerofoil and its wake can be represented by a sheet of vortices with strength $\gamma(x,t)$ (x in flow direction) lying on the plane $z=0$, which is parallel to the flow. Each of these vortices is an elementary solution of $\nabla^2\phi=0$, where $\phi(x,z)$ is the perturbation potential. The perturbation potential induced by the vortex sheet can then be expressed as

$$\phi(x,z) = -\int_{-b}^{\infty} \frac{\gamma(\xi)}{2\pi} \arctan\left(\frac{z}{x-\xi}\right) d\xi$$

For harmonic excitation, with the aerofoil vortex sheet $\gamma_a(x,t) = \hat{\gamma}_a(x)\, e^{i\omega t}$ and a similar response in the wake $\gamma_w(x,t) = \hat{\gamma}_w(x)\, e^{i\omega t}$, the following expression can be derived by implementing the four conditions above

$$-\frac{1}{2\pi}\int_{-b}^{b} \frac{\hat{\gamma}_a(\xi)}{x-\xi} d\xi + \frac{i\omega}{2\pi U_\infty}\hat{\Gamma}\int_{b}^{\infty} \frac{e^{i\omega\left(\frac{b-\xi}{U_\infty}\right)}}{x-\xi} d\xi = i\omega\hat{z}_a(x) + U_\infty \frac{\partial \hat{z}_a(x)}{\partial x}$$

This expression has been solved analytically for $\hat{\gamma}_a(x)$ by Theodorsen [1934], with $\hat{z}_a(x)$ defined for a harmonically pitching and plunging flat plate. Solutions are usually expressed in terms of Theodorsen's function $C(k)$, which is a combination of Hankel functions of the second kind:

$$C(k) = \frac{H_1^{(2)}(k)}{H_1^{(2)}(k) + iH_0^{(2)}(k)}$$

where the parameter k is the reduced frequency

$$k = \frac{\omega b}{U} = \frac{\omega c}{2U}.$$

This parameter k is often used to categorise the type of flow. It can be viewed as the ratio between the period of oscillation and the convection time. The convection time, U/b, is the time it takes for the perturbations, with characteristic time scale $1/\omega$, to have been convected half a chord length. If this ratio is low, the perturbations are convected relatively quickly, such that the flow behaves as if it were steady a steady flow. This case is called quasi-steady. A high ratio, i.e. high oscillation frequency to a relative low transport velocity, can give a true unsteady flow. In that case previous cycles of perturbations are having significant influence on the aerofoil before being convected to the far wake.

In figure 2.2 the components of Theodorsen's function, $C(k) = F(k) + iG(k)$, are shown as function of k. For $k=0$, the static case, the real component is one and the imaginary part is zero. For any other value of k the imaginary part is negative up to a magnitude of approximately -0.2. The complex valued function $C(k)$ will cause a decrease in amplitude and a phase shift of the harmonic response relative to the excitation.

For a combined pitch and plunge case the lift force on the flat plate can be expressed as

$$\begin{aligned} \ell &= \hat{\ell} e^{i\omega t} \\ &= \pi\rho b^2 \left[\ddot{h} + U\dot{\theta} - ba\ddot{\theta}\right] \\ &\quad + 2\pi\rho U b C(k) \left[\dot{h} + U\theta + b\left(\frac{1}{2} - a\right)\dot{\theta}\right] \end{aligned}$$

where $b = \frac{c}{2}$ and ab is the position of the pitch axis defined aft of the mid-chord position. This project only deals with a pitching motion, so the plunging terms h can be removed.

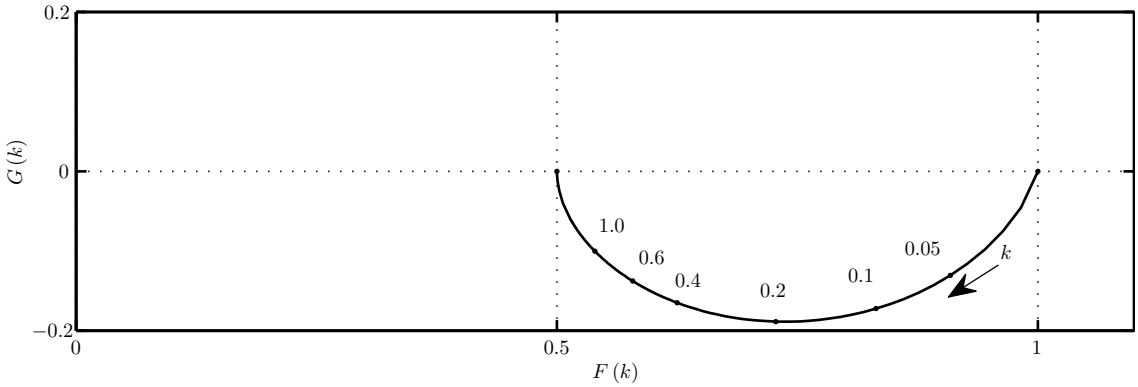

Figure 2.2: Components of Theodorsen's function $C(k) = F(k) + iG(k)$

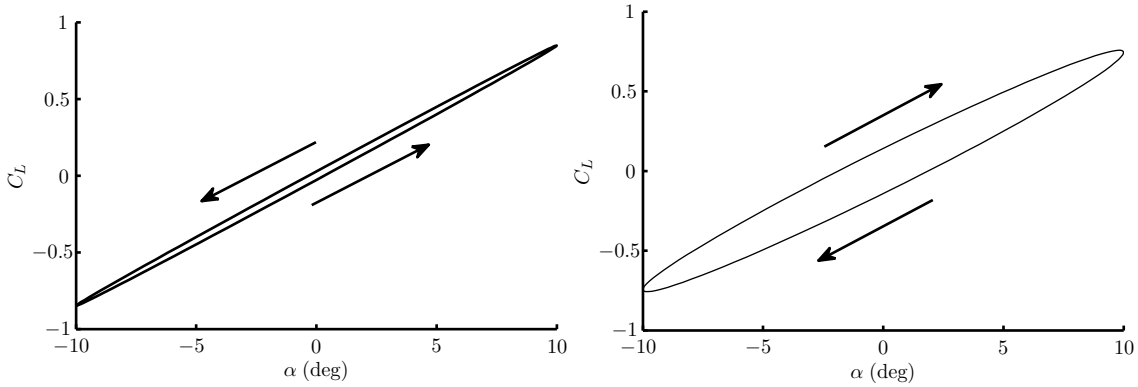

Figure 2.3: Lift curves following Theodorsen's function for a flat plate in pure pitch motion. Left a reduced frequency k of 0.168 and right for 0.335, both with an amplitude of 10 degrees. The arrows indicate the direction in time.

The pitch motion is of the form $\theta = \hat{\theta}e^{i\omega t}$, so the derivatives can be replaced by $\dot{\theta} = i\omega\hat{\theta}e^{i\omega t}$ and $\ddot{\theta} = -\omega^2\hat{\theta}e^{i\omega t}$. The expression can than be rearranged to

$$\hat{C}_\ell = \pi\left[ki + ak^2 + C(k)\left(2 + (1-2a)\,ki\right)\right]\hat{\theta},$$

where $\frac{\omega b}{U}$ has been replaced by the reduced frequency k and the entire expression has been divided by $\rho U^2 b (= \frac{1}{2}\rho U^2 c)$ to immediately obtain an expression for the lift coefficient. As will be explained in chapter 3.1, the pitching axis in the experimental set-up is placed at 3.5 cm from the leading edge. With a chord of 8 cm, this means the pitching axis is 0.5 cm in front of the mid chord position, which corresponds to $a = -0.125$. The experiments involving PIV have been performed at reduced frequencies of 0.168 (10 Hz) and 0.335 (20 Hz). The intention was to have a pitch amplitude of 10 degrees. For those two situations the lift curves obtained with Theodorsen's function are shown in figure 2.3. It follows that for the 10 Hz case it is predicted that there is a very narrow loop, where the down stroke gives higher lift than the upstroke. For 20 Hz, the loop is much wider, while the maximum lift coefficient is slightly lower than for the 10 Hz case. Another important difference is that the lift generated during the upstroke is now higher than during the down stroke, which appears as a reversal of the loop.

As the actual pitch motion of the aerofoil in the experiment is not perfectly sinusoidal, and therefore also the wake will not be perfectly sinusoidal, the previous expression for the lift would not apply exactly. The pitch motion can, however, be approximated by a sum of harmonic functions. Assuming that this linear property still holds in the wake, in view of the linearisations involved in the perturbation theory, the lift can than also be expressed as a linear sum of harmonic functions. Describing the pitch angle by

$$\theta(t) = \sum_{n=1}^{N} \alpha_n \cos(n\omega t) + \beta_n \sin(n\omega t)$$

the lift coefficient from Theodorsen's function can be written as

$$C_L(t) = \mathfrak{Re}\left(\pi \sum_{n=1}^{N} \left[nki + a(nk)^2 + C(k)(2 + (1-2a)nki)\right] \alpha_n e^{in\omega t}\right) \ldots + \mathfrak{Im}\left(\pi \sum_{n=1}^{N} \left[nki + a(nk)^2 + C(k)(2 + (1-2a)nki)\right] \beta_n e^{in\omega t}\right) \quad (2.1)$$

2.3 Aerodynamic forces from a velocity field

The output from PIV measurements is a desciption of the flow in terms of instantaneous velocity fields. This section describes the theory of how to derive the aerodynamic forces from these flow fields. The method is based on Newton's second law, $\mathbf{F} = \frac{d}{dt}(m\mathbf{V})$, in integral form. Taking an arbitrary control volume, the force $\mathbf{F}$ can be expressed as a combination of, a pressure force acting at the surface of the volume (III), body forces, like gravity, acting inside the volume (IV), and viscous forces (V). The time rate of change of momentum, $\frac{d}{dt}(m\mathbf{V})$, is a combination of the time rate of change of momentum due to unsteady fluctuations inside the volume (I) and the net flow of momentum out of the control volume (II) (across the surface of the control volume). Newton's second law can thus be expressed as

$$\underbrace{\iiint_{\mathcal{V}} \rho \frac{\partial}{\partial t}\mathbf{V} d\mathcal{V}}_{I} + \underbrace{\oiint_{\mathcal{S}} (\rho \mathbf{V} \cdot \mathbf{n} d\mathcal{S})\,\mathbf{V}}_{II} = \underbrace{-\oiint_{\mathcal{S}} p\mathbf{n} d\mathcal{S}}_{III} + \underbrace{\iiint_{\mathcal{V}} \rho \mathbf{f} d\mathcal{V}}_{IV} + \underbrace{\oiint_{\mathcal{S}} \boldsymbol{\tau} \cdot \mathbf{n} d\mathcal{S}}_{V},$$

the integral momentum equation for incompressible flows [Anderson, 2007]. In this equation $\mathcal{V}$ is the control volume, $\mathcal{S}$ is the surface of the control volume, and $\mathbf{n}$ is the outward normal of the control volume surface. Now defining the control volume around an object, such that the object's surface is part of the control volume surface (the object itself is outside the volume!). Calling this part of the control volume surface $\mathcal{S}_B$ and the remaining surface $\mathcal{S}$. For an impermeable object it is known that $\mathbf{V} \cdot \mathbf{n} = \mathbf{0}$. Neglecting the body forces the equation can be rearranged to

$$\iiint_{\mathcal{V}} \rho \frac{\partial}{\partial t}\mathbf{V} d\mathcal{V} + \oiint_{\mathcal{S}} (\rho \mathbf{V} \cdot \mathbf{n} d\mathcal{S})\,\mathbf{V} = -\oiint_{\mathcal{S}} p\mathbf{n} d\mathcal{S} + \oiint_{\mathcal{S}} \boldsymbol{\tau} \cdot \mathbf{n} d\mathcal{S} \underbrace{- \oiint_{\mathcal{S}_B} p\mathbf{n} d\mathcal{S} + \oiint_{\mathcal{S}_B} \boldsymbol{\tau} \cdot \mathbf{n} d\mathcal{S}}_{-\mathbf{F}(t)}.$$

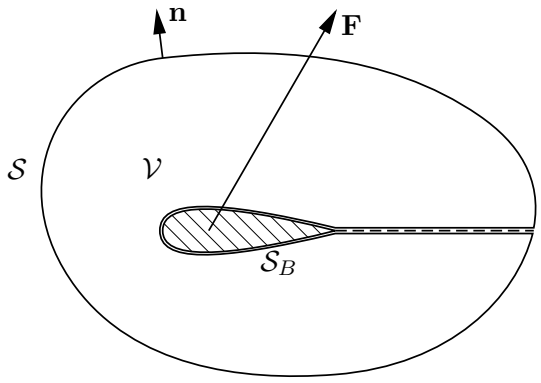

Figure 2.4: A control volume around an object. Notice the aerofoil actually being outside the control volume.

The last two terms in this equation together form the force the object is exerting on the flow, i.e. this is equal and opposite to the resultant aerodynamic force acting on the object. Now an expression for the instantaneous aerodynamic force is found

$$\mathbf{F}(t) = -\rho \iiint_{\mathcal{V}} \frac{\partial}{\partial t}\mathbf{V} d\mathcal{V} - \rho \oiint_{\mathcal{S}} (\mathbf{V}\cdot\mathbf{n})\,\mathbf{V} d\mathcal{S} - \oiint_{\mathcal{S}} p\mathbf{n} d\mathcal{S} + \oiint_{\mathcal{S}} \boldsymbol{\tau}\cdot\mathbf{n} d\mathcal{S}, \tag{2.2}$$

where the control volume is taken fixed in time and the flow to be incompressible (Noca [1997]; Casimiri [2006]; Oudheusden et al. [2007]; Kurtulus et al. [2007]).

Returning to the PIV velocity fields, it is obvious that the above expression requires more information than immediately available from a velocity field. Usually the viscous forces are negligible when sufficiently far from the aerofoil, so that this term can be ignored. However, the pressure term will be very significant. By making use of the momentum equation, the pressure can be explicitly evaluted by integration of the pressure gradient

$$-\nabla p = \rho\frac{\partial}{\partial t}\mathbf{V} + \rho(\mathbf{V}\cdot\nabla)\mathbf{V} - \mu\nabla^2\mathbf{V},. \tag{2.3}$$

as was done by Oudheusden et al. [2007]; Unal [1997]; Kurtulus et al. [2007]. For 2-D incompressible flow the instantaneous pressure gradient can be derived directly from the velocity field. The pressure can be obtained by integrating this gradient along the contour (for 2-D velocity fields, the surface integral becomes a contour integral). This pressure can then be used in equation 2.2. Integrating only along the contour does present the problem of error propagation. This can be partly remedied by integrating the pressure gradient over the entire domain by using a more elaborate scheme where the pressure at each location is determined from multiple neighbouring locations. This way the errors in the pressure gradient might be averaged out to some extent. Another method, as used by Kurtulus et al. [2007], is to use an integral form of the inviscid equation for those parts of the flow that are approximately irrotational

$$p(s) = \frac{\partial\phi}{\partial t} + p_0 - \frac{1}{2}\rho|\mathbf{V}(s)|^2 \tag{2.4}$$

The time derivative of the potential ϕ is neglected, which was possible since the experiment involved a static square cylinder so that the far field perturbations would be constant in

time. The result is a form of the Bernoulli equation. This expression was used to determine the pressure along the contour where it was appropriate to neglect the viscous term, i.e. everywhere outside the wake. The viscous expression for the pressure gradient (2.3) was then used to integrate over the wake region, thereby restricting the error propagation only to the wake region.

2.4 Principles of Particle Image Velocimetry

Particle image velocimetry (PIV) is a method to quantify kinematic flow properties based on (digital) photographic images. The flow is visualised using tracer particles, which have to be small enough to follow the fluid motion and should not change the properties of the flow, though they have to be large enough to be distinguishable in the recorded images. The displacement of the particles between two sequentially taken images indicates the velocity of the particles and therefore of the flow. Most of the information in this section is taken from the lecture notes of the course on experimental methods (AE4180, TU Delft) Scarano [2007].

With PIV the particles are not tracked all individually, but instead the full field of view (FOV) is divided up into smaller cells, for each of which a velocity vector is determined. The particle pattern in one such an interrogation window is compared to the pattern in the same window in the subsequent image one time instant later, by using cross-correlation[2]. The peak position of the cross-correlation map that follows, indicates the statistically most probable average displacement of the particles in that window.

The tracer particles used for this experiment were produced by a smoke generator (glycol-water solution) at the wind tunnel air intake (upstream of the settling chamber) to create a flow seeding as homogeneous as possible. The time separation between two subsequent images is very small, in the order of micro seconds. Therefore the exposure times for the cameras are very small. To get sufficient exposure and to illuminate only the particles in the plane of interest, a double pulsed high energy laser is used. One laser fires for the first image and the other for the second, so that very short image pair separation times are possible. The laser beam is then shaped into a flat sheet of light through optical elements.

The diameter of a glycol based particle is typically 1 μm. The image is projected onto the sensor. A magnification factor in the typical range for PIV would be $M = 0.16$, which means a single particle would measure 0.16 μm on the sensor. The pixels on the sensors of the HighSpeedStar6 cameras are 20 μm, about a 100 times larger than the geometric image of the particle. Fortunately there is an optical effect, called diffraction, which apparently bends light waves around small openings, such as the lens opening. The projected image of the particle due to the diffraction effect can be described by

$$d_{\text{diff}} = 2.44\lambda\,(1 + M)\,f_{\#}$$

[2]Cross-correlation is a statistical operation that repeatedly shifts one dataset, and then quantifies how well the shifted image fits the other dataset. If the shifted dataset is identical to the second dataset, the correlation value is maximum, while if there are no identical data points at all, the correlation value is minimum. The correlation values for all shifts form a cross-correlation map, of which the peak location indicates the displacement of the particle pattern.

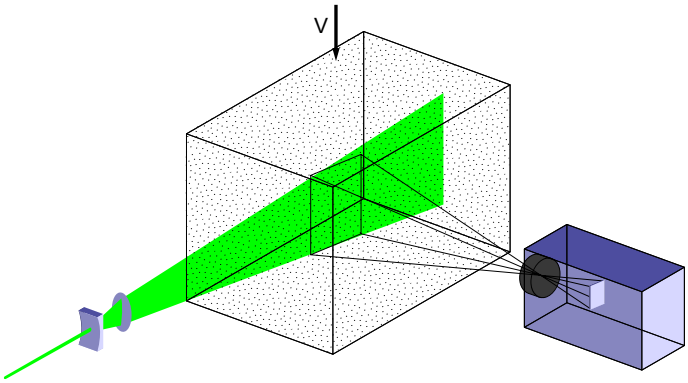

Figure 2.5: Typical PIV setup

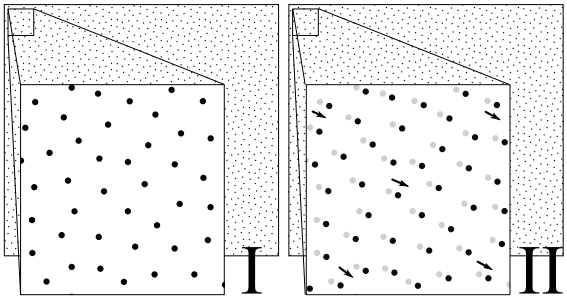

Figure 2.6: Schematic representation of the principle of PIV

where λ is the wavelength of the light, M the optical magnification and $f_{\#}$ the aperture number, which is the focal length of the lens divided by the aperture diameter. For a laser with a wavelength of 527 nm, a magnification of 0.16 and a minimum value for the aperture number of 2.8 (diaphragm fully opened), the resulting image diameter of a single particle becomes 4.18 μm, twenty times larger than the magnified image, but still smaller than one pixel.

For the most accurate prediction of the location of a particle, the particle image should have a diameter roughly double the size of a single pixel. Having a particle image smaller than one pixel results in an uncertainty for the location of the size of a pixel (any location within the pixel gives the same excitation of the pixel). If the image covers also the surrounding pixels, a more precise location of the particle can be determined by interpolation of the pixel intensities. For the example given above, the aperture number should be increased ten times, to about 28. In that case the aperture of the lens then gets really small, which means the image intensity decreases. The exposure time can not be increased much, because of motion blur and a limited separation time between two images. Therefore the particle illumination needs to be intensified, hence the use of high power lasers.

Chapter 3

Experimental Setup

A large part of the current project involved designing the set-up of the experiment. Therefore the a major part of this chapter will be about the final design of the experimental set-up and to explain why certain choices were made. The last part of this chapter will describe the experiments that were performed with this set-up.

3.1 Design of the test-section

The setup was designed specifically to fit the W-tunnel at TU Delft Aerospace Engineering's High Speed Lab (HSL). A steel frame was constructed in accordance to the dimensions of the tunnel exit. The frame was intended to be stiff and heavy such that there would be a solid base to mount all the moving parts on. Right from the start the aim was to obtain as high as possible pitch frequencies, since it is known that unsteady phenomena become prominent at high reduced frequencies.

The initial requirements of the set-up were

- 20 Hz (maximum) oscillating frequency
- low flow velocity (for high reduced frequencies and low Reynolds numbers)
- Good optical access for PIV (4 High speed cameras for overlapping fields-of-view)
- Simultaneous force measurements and PIV measurements
- 2D flow (as much as possible), such that the sectional PIV measurements and the direct force measurements are comparable

A choice was made to position the aerofoil vertically, to eliminate the effects of gravity forces on the oscillating structure. A three way view of the set-up is shown in figure 3.1. The next sections describe and motivate the different parts of the set-up.

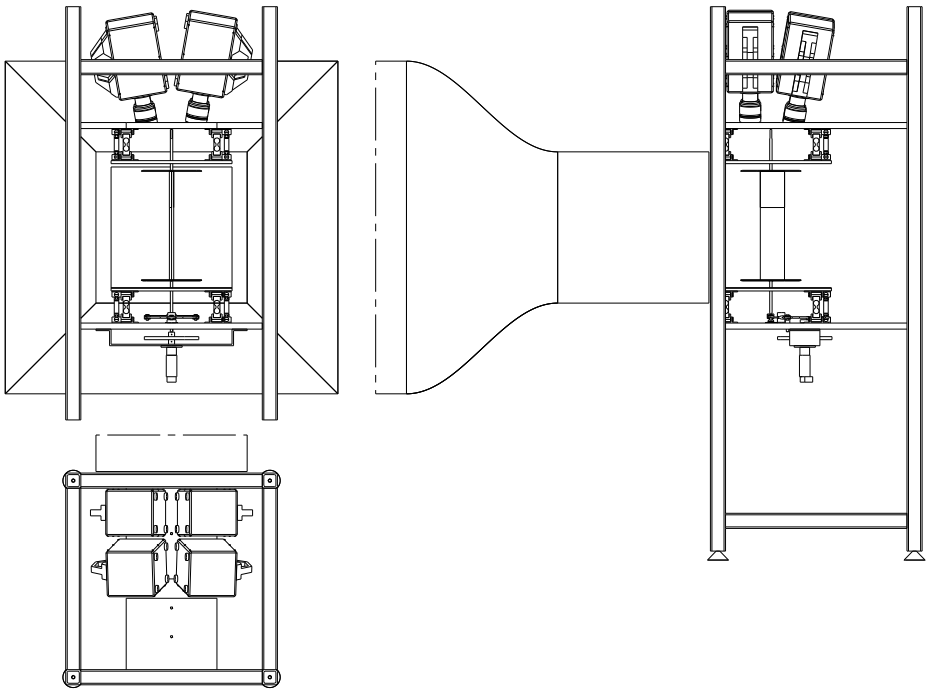

Figure 3.1: Three way view of the test-section. Left top is a front view, looking upstream into the wind tunnel. In the side view (right) the wind tunnel exit is shown. The lower left view is a top view.

3.1.1 Wind tunnel

The W-tunnel at TU Delft Aerospace Engineering's High Speed Lab (HSL) is an open-jet facility with an exit of 40×40cm. Maximum possible flow speeds are approximately 35 m/s. The tunnel is driven by a large centrifugal fan after which the air moves through a diffuser. The flow is slowed down and turbulence is reduced. The flow enters the settling chamber after which it is accelerated by a contraction (1:8) exiting at the wind tunnel exit. The wind tunnel exit has a turbulence level of 0.2%. In Kuik [2007] a boundary layer thickness of 24 mm was found on the lower wall of the tunnel for a test-section velocity of 9.8 m/s.

3.1.2 NACA0018 Aerofoil

For this set-up it was chosen to work with a NACA0018 aerofoil, for several reasons. First of all, a very practical reason was that an extruded aluminium profile was already available from other experiments. The fact that the NACA 4 series profiles are extensively investigated, makes it better comparable to studies. Further the symmetric NACA 4 series profiles are commonly used in rotor and propeller blades. These applications involve unsteady flows (pitching and heaving), which relate back to the background of this project. An additional advantage of this profile is that it is relatively thick, which is good against deformations of the aerofoil under high loads. This provides many possibilities for mounting the aerofoil. Also the thickness reduces the amount of deformation

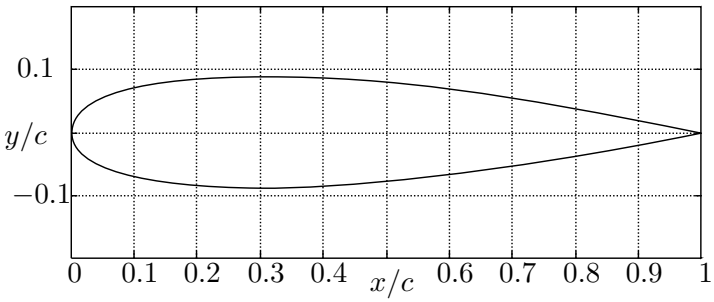

Figure 3.2: NACA0018 thickness profile

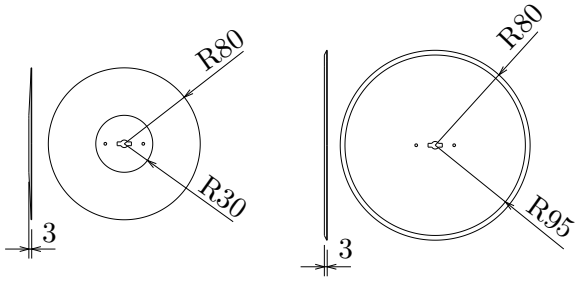

Figure 3.3: Comparison between old (left) and new (right) end-plates.

when experiencing high loadings, in this case especially torsional loads from the high pitch frequencies.

The thickness distribution of the symmetric NACA 4 series are described by the formula

$$\frac{y}{c} = \frac{t}{0.2}\left(0.2969\sqrt{\frac{x}{c}} - 0.1260\frac{x}{c} - 0.3537\left(\frac{x}{c}\right)^2 + 0.2843\left(\frac{x}{c}\right)^3 - 01014\left(\frac{x}{c}\right)^4\right),$$

where c is the aerofoil chord and t the maximum thickness ($t = 2\frac{y_{\max}}{c}$). The contour is shown in figure 3.2. The thickness of the NACA0018 profile is 18% and the chord of the extruded aluminium aerofoil 0.08 m.

For obtaining an as high as possible signal to noise ratio for the mechanical measurements, it makes sense to make the wing as large as possible such that generated forces are as large as possible. Starting out with the extruded profile, the chord was already fixed to 0.08 mm. The flow exits the tunnel with a boundary layer of significant thickness developed, meaning that close to the wall the velocity is not uniform. Therefore the span of the wing was restricted to 0.36 m, leaving 2 cm spacing on each side of the tunnel exit.

To maintain two dimensional flow conditions, end-plates were required. However, these end-plates had to be transparent in order to satisfy the optical access requirement. The end-plates used in the first experiments, with the aluminium aerofoil, had a radius of 80 mm and were 3 mm thick. The edges were sloped on the outside. These end-plates were transparent, but due to the slope and limited radius of the disk, the PIV images would become very distorted. So for the subsequent measurements involving PIV, end-plates with a radius of 100 mm and a smaller sloped edge were used. The two versions of the end-plates are shown in figure 3.3.

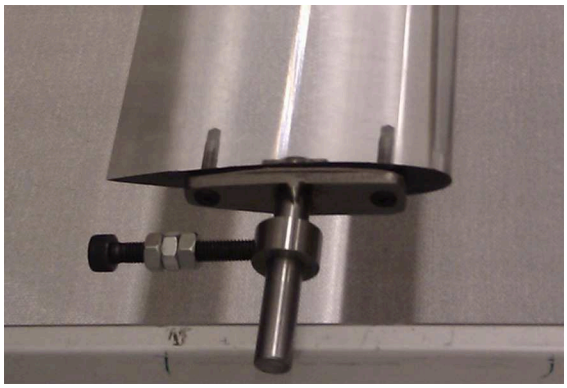

Figure 3.4: Balance weights on the transparent aerofoil.

Table 3.1: Overview of inertia around pitching axis.

Aluminium		Makrolon	
part	J_{alu}	part	J_{mak}
shaft ($\sim 1.5\times$)	$1.701 \cdot 10^{-7}$	shaft ($\sim 1.5\times$)	$1.701 \cdot 10^{-7}$
small end-plate ($2\times$)	$9.91 \cdot 10^{-5}$	large end-plate ($2\times$)	$5.206 \cdot 10^{-4}$
Alu profile	$9.69 \cdot 10^{-5}$	makrolon profile	$1.243 \cdot 10^{-4}$
balance weights ($2\times$)	$1.785 \cdot 10^{-6}$	balance weights ($2\times$)	$6.379 \cdot 10^{-7}$
total	$0.299 \cdot 10^{-3}$	total	$1.167 \cdot 10^{-3}$

Also for the PIV measurements, it was needed to have sufficient illumination everywhere around the aerofoil. One way of getting the laser light at both sides would be to have mirrors to fill up the areas blocked by the aerofoil. However, the aluminium aerofoil would block too much of the light sheet to get sufficient light on the back side. Therefore a second aerofoil was manufactured out of transparent Makrolon (polycarbonate), having the same dimensions as the first one.

The pitch axis is not positioned at the conventional quarter chord point, but at centre of gravity of the very first design[1] (not described here). The axis had to be placed at the centre of gravity to minimise inertial forces due to the pitching accelerations, which would otherwise be registered as lift and drag forces. After changing the design, the location of the pitch axis was maintained. To get the centre of gravity and the axis to coincide, balance weights were added to the axis, figure 3.4.

3.1.3 Actuation

The chosen method of actuation was to have motor driving an eccentric connected rocker as shown in figure 3.5. The eccentric is driven by a Maxon Motor RE35 motor (table 3.2) at a constant speed. The eccentric mechanism transforms this into an almost sinusoidal

[1] Initially a combination of the extruded aluminium aerofoil and the transparent aerofoil was intended. Here only the centre part of the wing would have been transparent. This aerofoil had its centre of gravity at 0.035 m from the leading edge. Advantage of this aerofoil would be a lighter wing, but manufacturing considerations favoured the fully transparent aerofoil.

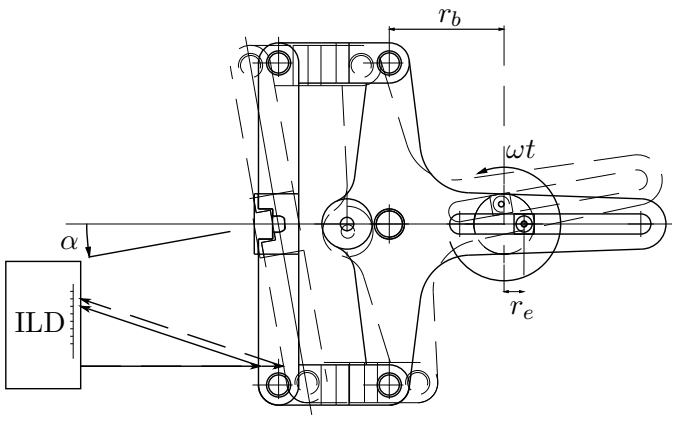

Figure 3.5: Actuation mechanism and the triangulating laser for measuring the angle of incidence.

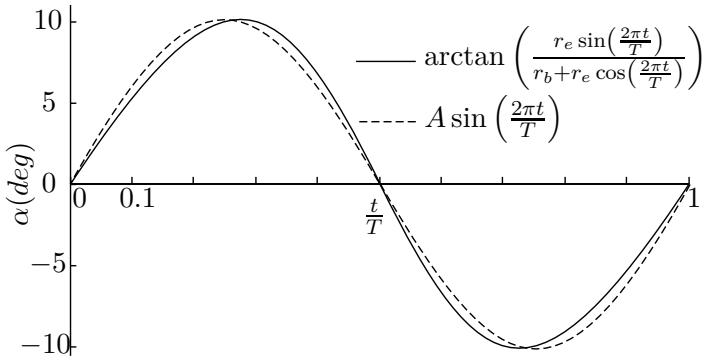

Figure 3.6: Almost sinusoidal motion of the actuator/aerofoil for $r_b = 5.7$ and $r_e = 1$ cm, resulting in an amplitude $A = 10.1°$.

motion, $\arctan\left(\frac{r_e \sin \omega t}{r_b + r_e \cos \omega t}\right)$, where ω is the eccentric angular frequency, r_e the eccentric radius and r_b the distance between the eccentric axis and the aerofoil pitching axis. The difference between the actual motion and a sinusoidal motion with the same amplitude and frequency is shown in figure 3.6, for the configuration used during the experiments (amplitude of approximately 10.1 degrees).

As mentioned, the actuation was driven by an electric motor, a Maxon Motor RE35 motor with graphite brushes. A 500 counts per turn (CPT) encoder provided control of the motor position. Using manufacturer provided libraries for LabView, the motor control was integrated with the Pitching Aerofoil Control and Acquisition program as described in section 3.1.5. To increase the available torque and increase the rotation precision, a gear-head was mounted to the motor axis. Two gear-heads were used (on two identical motors), one for frequencies up to 7 Hz (676/49 reduction) and the other for frequencies up to 20 Hz (24/5 reduction). The latter combination performed not as accurate at lower frequencies.

Since these type of motors are designed for the purpose of actuation, they have a little

Table 3.2: Specifications of the Maxon Motor RE35 electric motor.

	Maxon Motor RE35*
max rpm	5970
max torque	110 Nm
rotor inertia	63 gcm^2
assigned power rating	90 W

*closest match in Maxon catalogue, 273757 (actual motor was custom ordered)

rotor inertia. It was considered to directly have the motor actuate the pitching motion, but due to the inertia of the aerofoil itself, this turned out to be impossible. Especially for high frequencies the motor would not be able to produce accurate prescribed motions. Therefore the method of actuation explained at the start of this section was chosen. This means that the motor now can turn at constant speed. Constantly accelerating and decelerating the aerofoil does produce a large fluctuation in the required torque. Now the little inertia of the motor becomes a problem, since all this fluctuating torque has to be counteracted by the electrical torque of the motor. To solve this problem a flywheel, a 10 mm thick disk with a radius of 90 mm, is connected to the motor axis, to increase the inertia.

To measure the pitch angle during pitch motion, initially it was considered to read out the motor position. This method was very precise for static measurements, but dynamically the readout time proved not reliable. Therefore an additional pitch angle measurement was needed. It was decided to use a triangulating laser, a Micro-Epsilon ILD1401-50/ILD1300-50, normally used for measuring surface reliefs, to measure the displacement of the axis connector, as visualised in figure 3.5. The device works by sending out a small (red) laser beam to a surface. The light spot appearing on the surface spreads omnidirectional light. The device has a sensor array which, by use of a lens, only captures light coming from a known angle, so that the location where the array is excited is a measure for the distance between the laser spot and the device. This distance is then transformed to the pitch angle by the simple relation

$$\alpha = \arctan\left(\frac{dm - dm_0}{b}\right),$$

where dm is the distance measured by the device (and dm_0 this distance when $\alpha = 0$) and b is the distance between the emitted laser beam and the pitch axis. There is a small error in this expression, since the axis connector has a finite width of 2 cm. Calling this width $2e$, the exact expression should be

$$\tan\alpha \;=\; \frac{dm - dm_0}{b} + \frac{e}{b}\left(\frac{1}{\cos\alpha} - 1\right)$$

The ratio e/b is approximately 1/7. Additionally the pitch angle ranges from -15 to 15 degrees at most. within this range the term $(\cos^{-1}\alpha - 1)$ can be approximated by the quadratic relation, $\frac{1}{2}\alpha^2$ (with α in radians), which corresponds to a value of 0.035 for an angle of 15 degrees. So the maximum error in $\tan\alpha$ is around 0.005, while $\tan\alpha|_{15^\circ} \approx 0.27$, meaning that the maximum error is 1.87%.

Table 3.3: Specifications of the Micro-Epsilon ($\mu\varepsilon$) optoNCDT ILD1300-50 and ILD1401-50 laser displacement sensors.

	ILD1300-50 / ILD1401-50*
Measurement range (mm)	45 ... 95
Linearity (%FSO)	0.2
Static resolution (μm)	10 / 5
Dynamic resolution (μm)	25 / 25
Measurement rate (Hz)	500 / 1000
Output (mA)	4 ... 20
Supply (VDC)	11 ... 30 (used 24)
Electronics	Integrated signal processor

* used ILD1401-50 during first campaign and ILD1300-50 during second with PIV

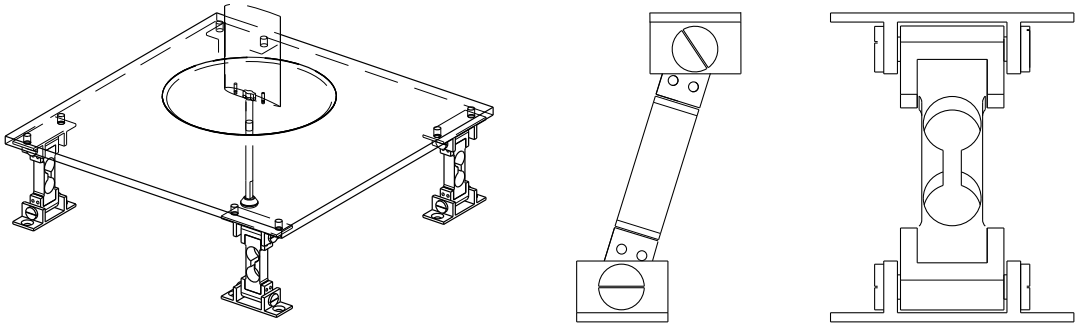

(a) Isometric view of the lower sensor platform. The platform on the other side of the aerofoil is identical.

(b) Bending beam load sensor hinging in the direction normal to the load sensitivity of the load cell.

Figure 3.7: Force transfer platform

3.1.4 Force measuring

The forces on the aerofoil are measured on both ends, top and bottom. This way the measurements also contain information about the moment around the span-wise centre of the aerofoil. Assuming a uniform span-wise aerodynamic force distribution, there should be no (aerodynamic) moment around the span-wise centre of the aerofoil, meaning that any moment that does exist is a result of the actuation force.

For the force measurements 8 Scaime EP2 single point load cells are used, which each have a nominal capacity of 2 kgf. These sensors work with strain gauges in a full Wheatstone bridge, placed in such a way that they are temperature compensated (and insensitive to any force other than the single point load). There are four load-cells corresponding to forces inline with the flow (drag) and also four in the direction perpendicular to the flow (lift).

The force on the aerofoil is transferred to the sensors via a transparent platform, to facilitate the PIV measurements. Strictly looking at mechanical measurements, this platform

should be as small and lightweight as possible, but the load-cells have to be connected to a stable base platform while also rigidly attached to the axis of the aerofoil. On the top side there has to be a clear field of view, and also physical space for the PIV cameras. This led to the size of the force transfer platform being 400 × 400 mm. This is also the width of the test-section exit of the wind tunnel, so that the platforms essentially become the walls of the test-section. The lower force transfer platform was made identical to maintain symmetry.

The top and bottom platform are identical, both having two sensors in drag direction and two in lift direction. The sensors are connected to the platform by hinges, figure 3.7b, allowing the sensor to move freely in the direction to which it is not sensitive. Two bearings on each side connected to an axis which was screwed tightly such that there was no movement in the direction to which the sensor was sensitive.

3.1.5 LabView Acquisition programming

A control and acquisition system was custom programmed in National Instruments LabView for the pitching aerofoil experiments. The purpose of this program was to combine as many of the tasks to be performed in a single interface. In the end the program had the following functions

- Controlling the motor speed or position. The user supplies the program with the required pitch angle or pitch frequency of the aerofoil, which are translated to commands for the motor encoder.
- Monitoring of wind tunnel conditions: the tunnel speed from the pitot pressure, the air temperature, and air density
- Monitoring of the forces registered the force sensors
- Monitoring the pitch angle from the ILD sensor
- Record above mentioned monitored values (by pressing a button)
- Send a trigger signal to the PIV system when starting a recording
- Read a signal from the PIV system of when it is recording. The start and end time (on base clock of force sensors) are recorded.

There were three hardware systems connected to the PC

- the motor controller, connected by a COM-port
- the NI SCXI-1520 8-Channel Universal Strain Gage Input Module, for reading the force sensors. This module was connected to a NI PCI 6250 card. Two of the digital channels not used by the NI SCXI-1520 module were used for the PIV triggering
- a cDAQ-9172 chassis with a NI 9215 module for the pitot pressure, temperature and ILD measurements. This chassis was connected to the PC through a USB connection.

The control and read-out of each of the above mentioned hardware systems is programmed in separate process loops in order to facilitate parallel processing. This was not only convenient, but really necessary, because otherwise the internal buffer of some systems (in particular the NI PCI 6250 card) would be full while waiting for another device (usually the motor controller, which uses a relatively slow COM-port connection for communication) to finish. Simply put, the different loops were created to allow for different processing times for each device. A fourth loop was used for handling the interface (user-inputs). This loop would wait for a user input and act there on, to conserve computing power.

It was chosen to work with a sample rate of 5 kHz for the force measurements. For a 20 Hz pitch frequency this leads to 250 samples per cycle. The cDAQ-9172 was also read at this frequency, because the measurement of the pitch angle was connected to it. The ILD devices used for the measurement of pitch angle use a lower sample rate, but this is transformed into an analog signal. Reading this analog signal at the highest possible sample rate, means the signal change is detected as accurate as possible. The other quantities measured with the cDAQ-9172 module, velocity, temperature and density, are not depending on time and were therefore averaged over time.

The test-section flow velocity was determined using Bernoulli's equation for incompressible flows

$$p + \frac{1}{2}\rho V^2 \quad = \quad p_0 \rightarrow V = \sqrt{2\frac{\Delta p}{\rho}}$$

where Δp is the difference between the total pressure p_0 in the settling chamber (which is equal to the total pressure in the test section, since it is constant along a streamline) and the static pressure p in the test section. This construction avoids having a pitot tube in the test section, which would influence the flow. The density is determined from the atmospheric pressure p_{atm} which is read from a digital barometer before each measurement, and the room temperature, according to the equation

$$\rho = \rho_s \frac{p_{\text{atm}}}{p_s} \frac{T_s}{T_{\text{room}}}$$

where the index s indicates standard atmosphere conditions, with $\rho_s = 1.225$ kg/m^3, $p_s = 1013.25$ hPa and $T_s = 288.15$ K. [Anderson, 2007]

3.1.6 PIV setup

Two PIV set-up were used, which are described in section 3.2. The main set-up, with four cameras, for the actual experiment and a secondary set-up to evaluate the two dimensionality of the flow. The cameras were mounted on a separate frame, so physically detached from the pitching aerofoil set-up, to avoid vibrations of the cameras.

The main set-up involved four HighSpeedStar6 high-speed CMOS cameras mounted above the aerofoil set-up, looking down through the aperture in the upper base platform. The physical dimensions of the cameras prevented positioning these perpendicularly to the measurement plane, while still getting enough overlap between each FOV. Therefore the cameras were tilted up to 8°, for which a Scheimpflug was used to tilt the focus plane.

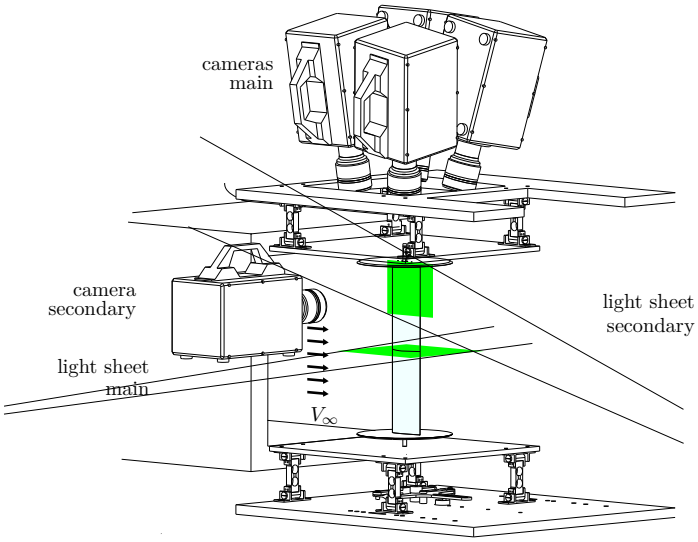

Figure 3.8: Positioning of the cameras and laser sheets for the main set-up (A) and the secondary set-up (B).

For such an angle the perspective error is estimated by $\cos 8° \approx 0.99 \rightarrow \varepsilon < 1\%$. The measurement plane, and therefore the laser sheet, was positioned horizontally (cross-sectional) at the span-wise centre of the aerofoil, as indicated in figure 3.8. A calibration plate was constructed by aligning a millimetre grid on paper with the laser sheet. This calibration grid was used for mapping the camera images, i.e. pixel coordinates, to real world coordinates.

A secondary set-up was used as a control for the effectiveness of the end-plates, i.e. qualifying the spanwise variation of the flow. These experiments used a single HSS6 camera pointing perpendicularly to the aerofoil plane at the region near the end-plate. The laser sheet was directed into the wind tunnel from a position upstream of the test-section.

The laser system used for particle illumination was a Quantronix Darwin-Duo diode-pumped (Nd:YLF) laser:

	Quantronix Darwin-Duo
Wavelength	527 nm
Total Energy	>50 mJ
Average Power @ 3 kHz	>80 W
Repetition Rate	0.1 to 10 kHz
Pulse duration	190 ns
Energy Stability	0.5% RMS
Beam Quality	M^2 <20

Quantronix, 2011

3.2 Measurement campaigns

For this study two measurement campaigns were held. First in June 2010, to examine the operation of the set-up for the full range of possible Reynolds numbers and pitch frequencies, i.e. from wind tunnel speeds from 0 to 30 m/s and pitching frequencies from 0 to 20 Hz. For these experiments not PIV measurements were performed. The second campaign in October 2010 was aimed primarily on performing the PIV measurements with simultaneous force measurements. Based on the results of the first campaign, a selective number of cases was chosen, in view of the large volume of PIV data and associated processing effort.

3.2.1 Full range measurements

The first experiments were performed with the aluminium aerofoil. Three types of measurements were performed. First of a calibration of the sensors, where the response is referenced to known forces. Secondly, for comparison with numerous available data of the NACA 0018 aerofoil, measurements of the non-oscillating aerofoil were performed. The third type were measurements of the actual oscillating aerofoil.

A static calibration was performed where a pulley was mounted to the frame. This pulley guided a thin metal string wire from the horizontal plane in which the sensors are sensitive to the vertical plane. The wire was connected to the aerofoil by a broad strap in such a way that the wire was in line with the aerofoil axis. The other end of the wire (vertical) was connected to a tray. Four weights of each 500 grams were placed onto the tray sequentially and then also again removed sequentially. Finally also the weight tray was lifted. With this procedure the response of the sensors to a known force is determined. In lift direction, both positive and negative forces could be calibrated, but because the set-up is positioned closely to the wind tunnel exit, only the positive drag direction was calibrated.

For the static aerofoil measurements were performed at velocities ranging from 0 to 30 m/s in steps of 5 m/s and the incidence angles from -10 to 10 degrees in steps of 1 degree. The aerofoil was first put to the required angle. A force from the actuation is now present in the measurement, so this is the 0 m/s measurement that will finally be subtracted from the actual measurements. Then the wind tunnel was started at 5 m/s. When the forces had stabilised, a measurement was taken after which the velocity was further increased. When all velocities were performed the tunnel was shut down, and the same procedure was performed for the next pitch angle.

The oscillating cases were build up from low pitching frequencies, 1 Hz, to high frequencies, 20 Hz, in steps of 3 Hz. This order was chosen because of the chances of the system failing would increase when testing at higher frequencies. For each frequency the the entire range from 0 to 30 m/s is ran through multiple times, giving 5 independent measurements for each case.

Table 3.4: PIV parameters for cross-flow measurements

	0°	10°	-10°
Field of view (mm^2)	181 × 181	171 × 171	181 × 181
$f_\#$		2.8	
Optical magnification	0.177	0.167	0.176
Digital magnification (px mm^{-1})	8.83	8.37	8.82
Pulse delay (μs)		100	
Free stream pixel displacement	13.25	12.55	13.23
Image pairs		1000 @ 1 kHz	
Pre-processing		subtract sliding minimum over 3 images	
Final interrogation window (px)		32 × 32	
Overlap (%)		75	
Grid spacing (mm)	0.906	0.956	0.907

3.2.2 PIV measurements

For the measurements with PIV measurements the transparent aerofoil was installed in the set-up. The force sensors were again calibrated as described in the previous section. From the results obtained in the previous session it followed that the repeatability[2] of the experiments was acceptable for velocities above 10 m/s, so the experiments were performed at 15 m/s.

First it was checked whether the flow over the aerofoil was sufficiently two-dimensional, meaning spanwise uniform mean flow, so that sectional lift obtained from PIV would be comparable to the integral lift measured by the force sensors. The spanwise measurements were performed on three pitch angles: 0°, 10° and -10°. The negative angle was viewed from the same side, so that essentially, the pressure and suction side of the aerofoil were examined. The PIV parameters are summarised in table 3.4.

Then the primary set-up was built for performing measurements in the cross-sectional plane at the spanwise centre of the aerofoil. The parameters of this set-up are shown in table 3.5. With this set-up again first the static case was tested, this time with simultaneous PIV and direct force measurements. To limit the amount of data and processing time, only 5 pitch angles were tested: 0°, 5°, 10°, -5° and -10°.

Finally the oscillating pitch cases were performed with PIV and direct force measurements performed simultaneously. Measurements on the aerofoil oscillating at 20 Hz were performed one time in air at rest and two times in air moving at 15 m/s. At 10 Hz measurements were performed one time in air at rest and three times in air moving at 15 m/s.

[2]The repeatability of the measurements was based on multiple independent measurements. However, at the time the decision for the second measurement campaign had to be made, the correction, as described in chapter 4.1.1 was not yet applied. The spread in the results decreased once this correction was applied, so a lower velocity could have been used.

Table 3.5: PIV parameters main set-up

	Main FOV
Field of view (mm^2)	208 × 198 (4 × (114 × 114) overlapping)*
$f_\#$	2.8
Optical magnification	0.1842
Digital magnification (px mm^{-1})	9.209
Pulse delay (μs)	50
Free stream pixel displacement (px)	6.9
Image pairs	1000 @ 1 kHz (static) and 2000 @ 2 kHz (oscillating)
Pre-processing	subtract sliding minimum over 3 images
Final interrogation window (px)	32 × 32
Overlap (%)	75
Grid spacing (mm)	0.869

* effective usable FOV is 140 × 160

Chapter 4

Data Processing

This chapter describes the steps taken to get from the acquired raw experimental data to a form in which it is possible to interpret. There were used two different measurement techniques, and so this chapter is divided into two sections. The first section treats the processing of the force measurement data. This process is not as straightforward as might be expected from balance measurements, due to several complicating factors arising when introducing an actuated pitching aerofoil. The second section discusses the post processing of the PIV measurements, covering the vector field computation, stitching of the four overlapping fields and the process of determining the aerodynamic forces from these stitched vector fields.

4.1 Post processing force balance data

The data obtained during the experiments was not immediately in the form of lift and drag forces. Besides the common calibration corrections, additional corrections related to the dynamic behaviour of the experiment were needed. First of all, the absolute force measured by the load cells was not equal to the applied force, since part of this applied force was transferred to the connection to the actuation system. Additionally, this actuation, while pitching, actually introduced a force to the measurement. This is discussed in 4.1.1. The correction that follows is extended in 4.1.2 for the dynamic system, where the frequency response of the sensor assembly comes in to play. In 4.1.3 a description of the calibration methods is given. Finally section 4.1.5 deals with determining the pitch angle during the experiment.

4.1.1 Static force correction

The connection to the actuation system added an unknown force to the equation. On the one hand this force absorbed part of the aerodynamic force applied to the aerofoil. Additionally, this connection also introduced forces during actuation. To compensate for

this, the assumption is made that the aerodynamic force acts symmetrically between the top and lower force transferring platforms, while the force on the actuator acts below the below the bottom platform. Assuming it is valid to use superposition, this means that the aerodynamic force registers equally strong on the top and on the lower transducers, while the actuation force registers asymmetrically. The simplified model gives the following two equations

$$\begin{aligned} \sum F: \quad & L - R_T - R_B - R_a &&= 0 \\ \sum M_{aer}^{\curvearrowleft}: \quad & \frac{b}{2}R_T - \frac{b}{2}R_B - \left(\frac{b}{2} + d\right) R_a &&= 0 \end{aligned}$$

from which it follows that

$$\begin{aligned} R_a &= \frac{b}{b+2d}\left(R_T - R_B\right) \\ L &= R_T + R_B + \frac{b}{b+2d}\left(R_T - R_B\right) \\ &= \frac{2b+2d}{b+2d}R_T + \frac{2d}{b+2d}R_B \end{aligned}$$

where R_a is the actuator force and R_T and R_B are the forces measured by the sensors, b is the wing span and d is the distance between the connection to the actuator and R_B (figure 4.2).

The effectiveness of this correction becomes clear when looking at the calibration measurements, table 4.2 and 4.3. Without the correction applied, the force registered by the sensors in drag direction has to be increased by 18%. When the asymmetry correction is applied, only an increase of 3-7% is needed. Additionally also a reduction in scatter is observed, demonstrated by a decreased root mean square error (RMSE).

4.1.2 Dynamic response correction

The correction obtained in the previous section had to be expanded for the pitching case. Figure 4.1a shows the results of applying only the static force correction on a measurement with 20 Hz oscillating frequency. The coefficient values are incredibly high. Figure 4.1b shows the force coefficient measured by the top and bottom force sensors. There is a phase shift between the two signals. This phase shift means either that the aerofoil is twisting, thereby creating spanwise varying loads, or that the balance system suffers from a harmonic response effects. Twist is observed, as discussed in section 4.1.5, but the observed twist can be modeled by assuming a rigid aerofoil and a twisting axis.

Figure 4.2 shows how the setup is modelled as a system of masses and springs. The corresponding values can be found in table 4.1. The load cells are modelled as springs with stiffness k. Further four masses are included:

- Aerofoil mass m_{ae}, which is the combined mass of the aerofoil, end plates and axis.
- Mass of the top force platform $m_{(T)}$
- Mass of the lower force platform $m_{(B)}$

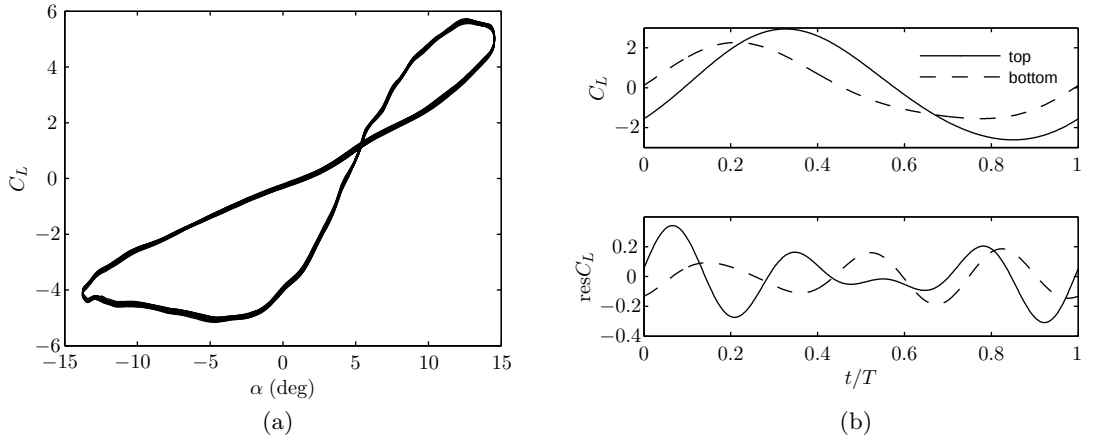

Figure 4.1: *Preliminary* result for a 20 Hz measurement at 15 m/s; 4.1a shows $C_L - \alpha$ curve, where the force data was obtained with the force balance, by just applying the static correction (The pitch angle was obtained from PIV data). 4.1b shows a Fourier fit through the data points from top and bottom force sensors, with the residual plotted underneath.

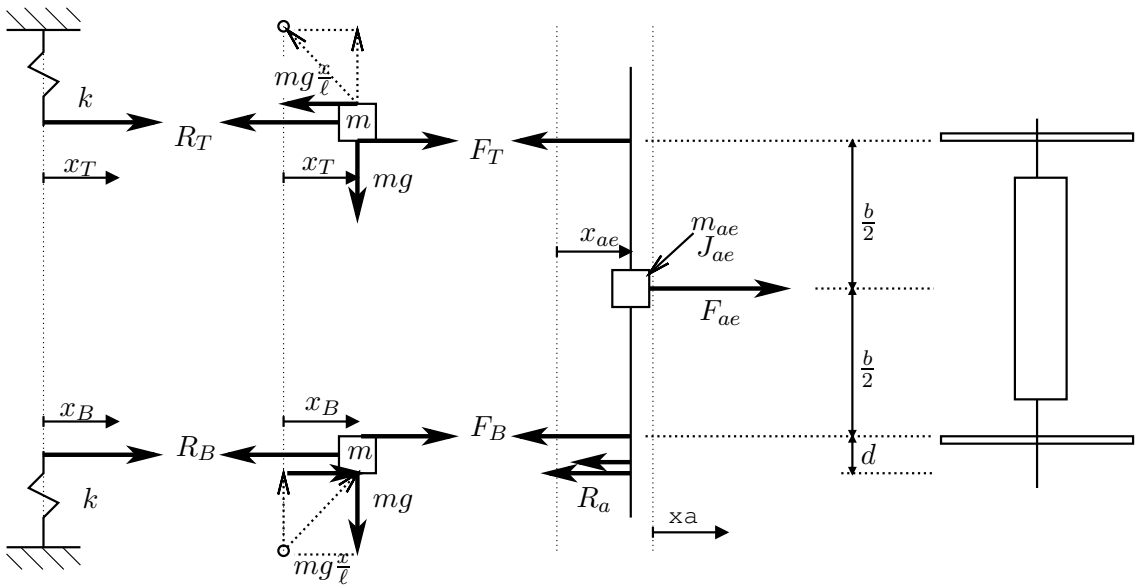

Figure 4.2: Visual representation of the mass-spring model used for the dynamic response correction.

Table 4.1: Properties relevant for frequency response correction of balance forces

		aluminium / Makrolon
masses		
aerofoil mass	m_{ae}	0.35 / 0.59 kg
force transfer platform mass	$m_{(T/B)}$	2.5 kg
mass inertia around aerofoil center	J_{ae}	0.008 / 0.014 kg·m^2
distances		
distance between sensor platforms	b	0.41 m
distance R_a and R_B	d	0.089 m
distance between sensor hinges	ℓ	0.082 m
stiffness		
sensor stiffness (combined sensor pairs)	k	$1{\cdot}10^5$ N/m

The equations describing this model can be written as

$$[\mathbf{M}] \left\{ \begin{array}{c} \ddot{x} \\ \ddot{\theta} \end{array} \right\} + [\mathbf{K}] \left\{ \begin{array}{c} x \\ \theta \end{array} \right\} = \left\{ \begin{array}{c} L - R_a \\ \left(\frac{b}{2} + d\right) R_a \end{array} \right\}$$

The eigenfrequencies of this system are found from $\det\left(\mathbf{K} - \omega_n^2 \mathbf{M}\right) = 0$, and for both aerofoils the eigenfrequencies for (coupled) modes of rotation and translation are around 30 Hz. The displacements x and θ can be translated into the forces registered by the load cells. Assuming an excitation and response of form $\exp\left(i\omega_a t\right)$ the system of equations can be written as

$$\underbrace{\left[\mathbf{K} - n^2\omega_a^2\mathbf{M}\right] \cdot [\mathbf{R}]}_{[\mathbf{C}]} \left\{ \begin{array}{c} R_{T,n} \\ R_{B,n} \end{array} \right\} = \left\{ \begin{array}{c} L - R_a \\ \left(\frac{b}{2} + d\right) R_a \end{array} \right\}$$

where $[\mathbf{R}]$ is the transformation matrix from measured forces to displacements. The matrix on the left hand side is the correction matrix $[\mathbf{C}]$ to get from measured forces to the actual forces. This system can now be solved for the aerodynamic force L:

$$\begin{aligned} L &= C_T R_T + C_B R_B \\ C_T &= \frac{2b+2d}{b+2d}\left(1 + \frac{mg}{k\ell} - \frac{n^2\omega_a^2}{k/m}\left(1 + \frac{1}{4}\frac{b+2d}{b+d}\frac{m_{ae}}{m} + \frac{b}{b+d}\frac{J_{ae}/b^2}{m}\right)\right) \\ C_B &= \frac{2d}{b+2d}\left(1 - \frac{mg}{k\ell} - \frac{n^2\omega_a^2}{k/m}\left(1 - \frac{b+2d}{d}\frac{m_{ae}}{m} - \frac{b}{d}\frac{J_{ae}/b^2}{m}\right)\right) \end{aligned}$$

The step by step derivation can be found in Appendix A. The effect of gravity is very small, i.e. $mg/k\ell = \mathcal{O}\left(10^{-3}\right)$. For the static case, $\omega_a = 0$, the same correction is obtained as in 4.1.1.

4.1.3 Calibration

Since the force sensors were built into a structure, it can not be assumed that the forces measured by the load cells are equal to the forces applied to the aerofoil. Therefore

Table 4.2: Force calibration for the October sessions, with the Makrolon aerofoil

(a) No asymmetry correction applied

	Cal. factor	RMSE [N]
D	1.1756	0.1277
L	0.9757	0.7501

(b) Asymmetry correction applied

	Cal. factor	RMSE [N]
D	1.0507	0.0532
L	1.0656	0.1329

reference measurements were performed with calibration weights up to 2 kg e.g. 19.6 N in steps of 0.5 kg. Also the weight of the balance tray was used as calibration weight, having a weight of 0.334 kg. The force in lift direction could be calibrated in two directions, positive and negative, simply by moving the calibration rig to the other side. In drag direction only the 'positive' drag could be calibrated, since on the other side there was no space due to the presence of the wind tunnel exit.

The correction is applied as

$$[\mathbf{A}]\{\mathbf{R}\} = \{\mathbf{F}\}$$

where $[\mathbf{A}]$ is the calibration matrix to be determined and vectors $\{\mathbf{R}\}$ and $\{\mathbf{F}\}$ represent respectively the measured forces and the applied forces,

$$\{\mathbf{R}\} = \begin{Bmatrix} R_D \\ R_L \end{Bmatrix}, \quad \{\mathbf{F}\} = \begin{Bmatrix} F_D \\ F_L \end{Bmatrix}$$

with indices D and L respectively. indicating drag and lift direction. As mentioned in the previous sections, there is an unknown force at the point of actuation, which should be eliminated by the asymmetric correction. In the equation above, the measured values R need to have this already correction applied, i.e. $\{\mathbf{R}\} = C_T\{\mathbf{R}_T\} + C_B\{\mathbf{R}_B\}$. Calibration matrix $[\mathbf{A}]$ is found by means of a least squares method.

It was found that the forces in the separate directions acted sufficiently independent. The small dependency that does exist could as likely be due to a misalignment of the calibration rig as due to a actual correlation between the separate directions. Therefore the applied calibration factors are determined from

$$\begin{aligned} A_D R_D &= F_D \\ A_L R_L &= F_L \end{aligned}$$

The result is displayed in table 4.3b for the sessions with the aluminium aerofoil and table 4.2b for those with the Makrolon aerofoil (these calibrations are related to the separate measurement campaigns, not so much to the aerofoils).

Parasitic drag correction The end plates at the ends of the aerofoil, the force transferring plates and the axis are parts of the test setup that do experience aerodynamic forces, which are registered by the force sensors. Since only the forces on the aerofoil are of interest, all other forces, hereby defined as parasitic drag, were measured separately by performing measurements with the aerofoil removed. Because the end plates are circular and centred on the pitching axis, it was assumed that the parasitic drag would be

Table 4.3: Force calibration for the June sessions, with the Aluminium aerofoil

(a) No asymmetry correction applied

	Cal. factor	RMSE [N]
D	1.1803	0.1003
L	1.0721	0.1347

(b) Asymmetry correction applied

	Cal. factor	RMSE [N]
D	1.0378	0.0427
L	1.0395	0.0642

Table 4.4: Parasitic drag

(a) Setup June

V	$C_{D,\text{par}}$	$(\pm\sigma)$
5.1	0.07727	(0.02163)
10.0	0.07724	(0.03333)
15.1	0.07294	(0.01768)
20.0	0.07172	(0.01508)
25.0	0.06845	(0.02246)
30.2	0.06769	(0.01427)

(b) Setup October

V	$C_{D,\text{par}}$	$(\pm\sigma)$
15.2	0.08652	(0.01680)

independent of angle of attack and pitch rate, so that only static measurements would suffice.

Because the upper and lower force sensors were now not connected, it makes no sense to apply an asymmetry correction. The lower sensors are still affected by the connection with the actuator. The top sensors are only influenced by the effect of gravity. The effect of gravity was found to be in the order of 10^{-3} N. When the assumption is made that the top sensors indicate the correct value for the parasitic drag the coefficients, $C_{D,\text{par}} = \frac{D}{\frac{1}{2}\rho V^2 cb}$ (so with the aerofoil dimensions used for reference), are shown in table 4.4. For 15 m/s, the flow velocity at which the PIV experiments were performed, the coefficient has to be multiplied by approximately 4 to obtain the actual force, so then the parasitic drag is larger than 0.3 N. This means the effect of gravity is 2 orders of magnitude smaller. This is also well within one standard deviation (including signal noise and unsteadiness of the flow) of the obtained value. Therefore this parasitic drag value is assumed to be valid (at least for flow velocities above 15 m/s).

4.1.4 Clock errors

In the experimental setup several measurement systems were used, as described in chapter 3. This means that different quantities were measured using different clocks for reference. When relating the angle of attack to the force data the use of different clocks presented to be a problem. The phase shift between the pitch angle data and the force data varied between repeated measurements.

To quantify this error, the cases with low pitch frequencies are examined for the observed phase shifts. The corrected pitch angle measurement (corrected for twist, section 4.1.5)

Table 4.5: Phase shifts of the lift force for 3 Hz cases with the aluminium aerofoil.

V (m/s)	k	t'_L ($\pm\sigma$) (ms)		$t'_{L,\max}$ (ms)	t'_{Th} (ms)
10	0.074	4.71	(6.93)	11.45	6.91
15	0.050	-3.37	(4.76)	6.73	6.60
20	0.037	-4.71	(5.04)	8.75	6.12
25	0.030	3.37	(2.13)	3.37	5.76
30	0.025	4.71	(4.57)	8.75	5.37
average		-2.39	(4.61)	7.82	

is taken as reference, with the upstroke through zero as t_0. The crossing positive zero crossing of the lift force, as found after applying the correction described in section 4.1.2, is then taken as the phase shift. Some phase shift is expected, as it is predicted by Theodorsen's function. Table 4.5 shows the phase shifts for the 3 Hz case with the aluminium aerofoil, from the experiments performed in June 2010. The second column shows the reduced frequency, $k = \omega c/2U$. The third column shows the mean and standard deviation of the observed phase shift between force and pitch data, each averaged over five independent measurements. The fourth column is the maximum encountered deviation from the mean value, which in this case might be a better indicator than the standard deviation, because of the low sample size. The last column shows the phase shift expected from Theodorsen's function.

It follows that the phase shifts are of the same magnitude as the expected phase shifts due to unsteady flow, however, the trend and even the sign do not correspond. Further the spread in phase shifts between measurements is also of the same order, around 5 ms and in some cases even 10 ms. Especially the latter observation is an indication of the unreliability of the timing of these measurements. This timing issue is independent of the pitching frequency. For 3 Hz, 5 ms is 1.5% of the cycle time, so that might be considered acceptable. Increasing the pitch frequency to 10 Hz, however, this percentage is 5% and for 20 Hz even 10% of the pitch cycle.

4.1.5 Twisting axis

Another problem arose when comparing the angles of attack determined from PIV images (4.2.2) with the measured angles of attack at the actuation level, i.e. the base of the axis. The significant difference between the two methods can for a large extent be explained by twisting of the axis. Table 4.6 shows the result of mechanical deformation simulations in Dassault's CATIA V5. A rotational acceleration ($\ddot{\theta}$ in the table) is applied to the Makrolon aerofoil that is clamped on one end and restricted from translating on the other end. The twist of the aerofoil mid-span location is shown under $\varphi_{\mathrm{Mak},c/2}$. The torque, equivalent to the aerofoil under angular acceleration, is applied to the axis, which is also clamped on one end. This twist is indicated under φ_b. Assuming the axis and the aerofoil are rigidly connected, the total twist ϕ is found. As can be seen, the twist of the axis contributes to more than 75% of the twist.

When assuming that it is purely the actuating axis that is twisting and not the aerofoil, a relative easy correction might be applied. Expected would be an underestimation of

Table 4.6: CATIA twist simulation

$\ddot{\phi}$ rad/s^2	φ_b (deg)	$\varphi_{\mathrm{Mak},c/2}$ (deg)	ϕ (deg)	$\varphi_{\mathrm{Mak},c/2}/\phi$
1 000	0.066	0.022	0.088	0.247
2 000	0.134	0.043	0.177	0.243
4 000	0.267	0.087	0.354	0.246
8 000	0.533	0.175	0.708	0.247
16 000	1.069	0.348	1.417	0.246
32 000	2.132	0.694	2.826	0.246
64 000	4.274	1.395	5.669	0.246

Table 4.7: Properties relevant for the twist model.

		aluminium / Makrolon
mass inertia		
mass inertia around pitch axis	J_a	$0.299{\cdot}10^{-3}$ / $1.16{\cdot}10^{-3}$ kg·m^2
pitch axis		
twisted length of pitch axis	d	0.10 m
polar moment (area) of inertia	I_p	$0.4021{\cdot}10^{-9}$ m^4
shear modulus	G	23 GPa
twisting axis stiffness	κ	92.5 Nm

25%. It will follow however, that completely neglecting the deformation of the aerofoil, returns a model that sufficiently corresponds to the PIV observation. For this the axis and aerofoil are simplified to two disks connected by a spring. The first disk is on the side of the axis where the actuation torque is applied. The second disk represents the aerofoil (and everything attached to it above the axis connection). The spring represents the actuated axis. The values of the relevant properties are shown in table 4.7.

The forces on the first disk are the actuation torque T_a and the the spring torque $\kappa\phi$. The mass of this disk is taken zero. In equation form $T_a = \kappa\phi$. This torque also acts on the second disk. This disk does have mass, the mass moment of inertia of the aerofoil around the pitch axis, which has the angular acceleration $\ddot{\alpha}_r$. In equation form

$$\kappa\phi = J_a\ddot{\alpha}_r \tag{4.1}$$

The spring torque is the product of the axial stiffness of the axis and the twist of the axis:

$$\kappa = \frac{GI_p}{d} \tag{4.2}$$

$$\phi = \alpha_a - \alpha_r \tag{4.3}$$

in which G is the shear modulus, I_p the polar moment of inertia and d the (twisted) length of the axis. The twist of the axis ϕ is the difference between the pitch angle measured at actuation level (α_a) and the that observed in the PIV plane (α_r). For the aluminium shaft the tortional stiffness κ can be estimated:

$$\kappa \approx \frac{23 \times 0.4021}{0.1} = 92.5 \text{ Nm}$$

For the first measurement campaign, there is no data on the real angle of attack of the aerofoil α_r, only the angle of attack measurements at the actuation level α_a are known. For these measurements the aluminium aerofoil was used, which had a different moment of inertia, J_{alu}. By rearranging equation 4.1 with equation 4.3 a differential equation for the real angle of attack α_r can be derived

$$\begin{aligned} J_a\ddot{\alpha}_r + \kappa\alpha_r &= \kappa\alpha_a && (4.4)\\ \text{or alternatively } \ddot{\alpha}_r + \omega_n^2\alpha_r &= \omega_n^2\alpha_a && (4.5)\\ \text{where } \omega_n &= \sqrt{\frac{\kappa}{J_a}} \end{aligned}$$

The homogeneous solution, though not really that relevant in this case, is

$$\alpha_h = \hat{\alpha}_r \sin(\omega_n t + \varphi)$$

What is relevant, is the response to the actuation. The angle of attack at the base is not perfectly sinusoidal, but it was found that α_a can be accurately expressed as a Fourier series with the actuation frequency and at least one multiple of this frequency (as handled by MATLAB fitting toolbox):

$$\alpha_a(t) = a_0 + \sum_{j=1}^{N} a_j \cos j\omega_a t + b_j \sin j\omega_a t$$

Solving the differential equation gives an expression for the real angle of attack,

$$\alpha_r(t) = a_0 + \sum_{j=1}^{N} \frac{\omega_n^2}{\omega_n^2 - j^2\omega_a^2}\left(a_j \cos j\omega_a t + b_j \sin j\omega_a t\right)$$

So for each frequency there is an amplification factor that depends on how close that mode is to the eigenfrequency of the aerofoil assembly. The eigenfrequency of the Makrolon aerofoil assembly is estimated to be 45 Hz. For a pitching frequency of 20 Hz, this gives an amplification factor of the first modes of

$$\begin{aligned} c_1 &= \frac{1}{1-\left(\frac{20}{45}\right)^2} = 1.25\\ c_2 &= \frac{1}{1-\left(\frac{2\cdot 20}{45}\right)^2} = 4.76\\ c_3 &= \frac{1}{1-\left(\frac{3\cdot 20}{45}\right)^2} = -1.28 \end{aligned}$$

which means the first mode is amplified 25% while the second is amplified almost 5 times! This method can now be used to correct the angles of attack for the cases where no PIV measurements were performed, i.e. the measurements with the aluminium aerofoil.

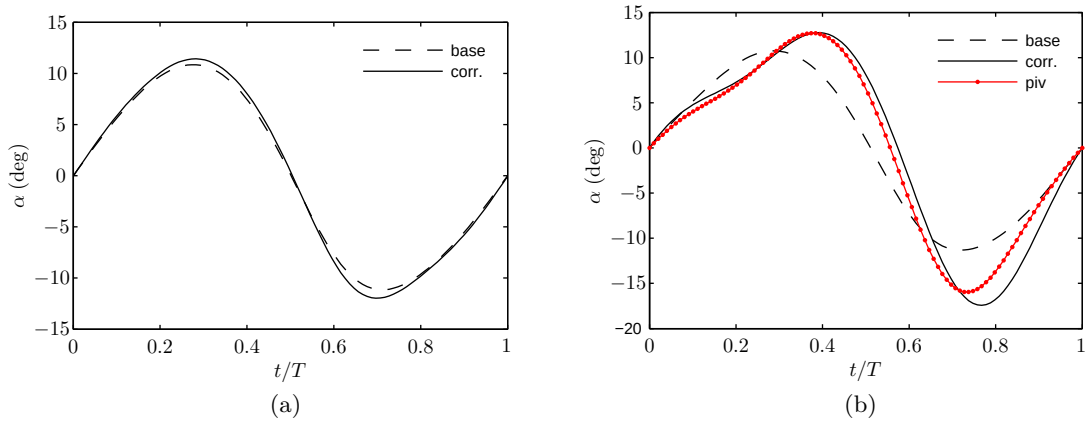

Figure 4.3: Effect of frequency dependent correction due to twisting of the pitch axis for a 20 Hz oscillation. The axis twists less severe with the aluminium (4.3a) aerofoil compared to the Makrolon aerofoil (4.3b). The latter also shows the pitch angle based on the PIV images.

For the aluminium aerofoil the eigenfrequency was estimated at 87 Hz. The amplification of the modes (also for the 20 Hz case) are now

$$c_1 = \frac{1}{1-\left(\frac{20}{87}\right)^2} = 1.056$$

$$c_2 = \frac{1}{1-\left(\frac{2\cdot 20}{87}\right)^2} = 1.27$$

$$c_3 = \frac{1}{1-\left(\frac{3\cdot 20}{87}\right)^2} = 1.90$$

which shows that the corrections needed are far less severe (and therefore probably also more reliable). In figure 4.3 the effect of the correction is demonstrated for the aluminium aerofoil (4.3a) and for the Makrolon aerofoil (4.3b), for both cases at 20 Hz pitch frequency (and wind tunnel velocity of 15 m/s). For the Makrolon aerofoil it can be seen that the twist model overshoots the real pitch angle observed from the PIV images at the lowest pitch angle. A first thought was that it might have something to do with damping, but just including damping into the model did not solve the problem. As can be seen, the first part of the motion agrees very well. Including damping severely compromises this agreement. However, the estimated twist with the aluminium aerofoil is very small. If the twist model suffers a proportionally comparable overshoot here, it would be very marginal. The twist model was only needed for the aluminium aerofoil cases (all Makrolon aerofoil case had PIV-data), so it was decided not to look for improvement of the twist model.

Something that should be noted, is the amount of twist of the aerofoil itself that can be expected, when comparing table 4.6 with the actual twist found from the PIV pitch angle data in figure 4.3b. The maximum difference between the measurement at actuation level and that from PIV, is about 5°. If 25% of this total twist, measured at the spanwise centre, is caused by the twist of the aerofoil itself, the aerofoil is twisted 2.5° from top to bottom. This is quite substantial, meaning that the lift distribution will probably not

be uniform. Also this compromises the frequency response correction described in section 4.1.2.

4.2 Processing of the PIV data

To get from the raw high speed images to the aerodynamic forces requires some additional steps, besides the standard correlation of the image pairs. First of all, there are four cameras with overlapping views. These views have to be aligned and merged. This process is described in 4.2.1. Additionally, the pitch angles can be extracted from the PIV images, which will be explained in 4.2.2. When the complete vector fields are available, the forces can be determined with the contour integral mentioned in 2.3. This method and preliminary results are described in 4.2.3.

4.2.1 Stitching four overlapping fields of view

Four cameras were used to increase the Field of View (FOV) and to overcome perspective blockage near the aerofoil. Each camera was positioned such that the individual FOV's overlapped by approximately 3 cm. The combined FOV of the cameras was therefore 208×198 mm^2, however the effective FOV was smaller due to the limited area illuminated by the light sheet (140×160 mm^2). Using a single calibration plate with a clear millimetre grid, each camera view was calibrated, i.e. a mapping to real world coordinates was determined, inside DaVis. On the calibration plate marks were placed in the overlapping areas, in order to visually link the individual coordinate systems to each-other.

For obtaining the full vector fields from PIV, the vector fields were first computed for each individual frame using DaVis. During this computation the data is mapped to real world coordinates. The computed vector fields were then exported to techplot format (*.DAT). These files could be read by MATLAB . With the real world coordinates of the markers in the overlapping areas, determined inside DaVis, the vector fields were mapped onto a uniformly spaced grid covering the combined FOV using linear interpolation. Then in each (remapped) vector field the aerofoil was masked, using the pitch angle obtained as described in 4.2.2. Additionally the areas blocked by the aerofoil are also masked. Following, the four vector fields were combined, the overlapping areas averaged.

The laser light passing through the transparent aerofoil caused an irregular (and unsteady) light sheet. This resulted into some poorly resolved regions in the flow field, as indicated in figure 4.4. Additionally also distortion due to the sloped edges of the end-plates was a cause for unresolved patches. These missing vectors were important in order to solve the contour integral, so these were interpolated from the surrounding points.

4.2.2 Determining pitch angle from PIV measurements

The pitch angle of the aerofoil was initially meant to be measured by the excursions of the actuation system, as described in 3.1.3. During the first measurement campaign this method proved to be flawed, as described in 4.1.5. With earlier PIV experiments with an oscillating aerofoil (Nati [2010]), the pitch angle was determined from tracking the aerofoil

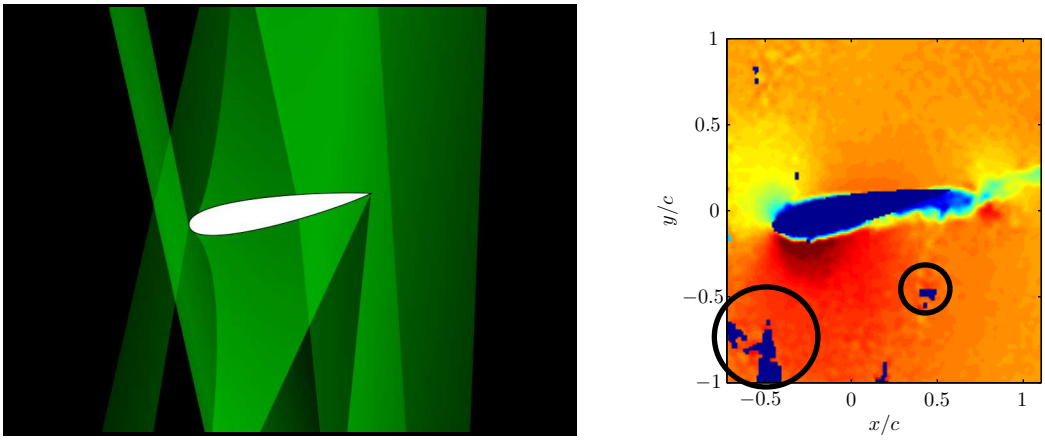

(a) (b)

Figure 4.4: Distortion of the light sheet due to the aerofoil lens working (4.4a) causing unresolved areas in the vector field (4.4b).

in the PIV images. This was possible because the laser sheet lights up the contour of the aerofoil. For the current experiments the trailing edge, having the highest intensity, was tracked. The rotation point of the aerofoil was known, so from these two points the pitch angle can be determined, as shown in figure 4.5

For the determination of the pitch angle, the images taken during the experiments were mapped to the real world and then exported as image files (*.TIFF). The top two frames were combined by identifying the pixel coordinates of the markers at the calibration plate in the overlapping areas. The result of this stitching combination is shown in figure 4.6.

4.2.3 Computing aerodynamic forces

Chapter 2.2 describes a method to derive the aerodynamic forces from velocity data. In the previous sections the process of constructing the vector fields is described. In this section it is explained how the forces are computed. Below is equation 2.2, where the viscous forces are neglected.

$$\begin{aligned}
\mathbf{F}(t) &= -\rho \iiint_{\mathcal{V}} \frac{\partial}{\partial t}\mathbf{V} d\mathcal{V} - \rho \oint_{\mathcal{S}} (\mathbf{V}\cdot\mathbf{n})\,\mathbf{V} d\mathcal{S} - \oint_{\mathcal{S}} p\mathbf{n} d\mathcal{S} \\
c_d &= -\frac{2}{V_\infty^2 c}\left(\iiint_{\mathcal{V}} \frac{du}{dt} d\mathcal{V} + \oint_{\mathcal{S}} u\,(u\,n_x + v\,n_y) + \frac{1}{\rho} p\,n_x d\mathcal{S}\right) \qquad (4.6) \\
c_l &= -\frac{2}{V_\infty^2 c}\left(\iiint_{\mathcal{V}} \frac{dv}{dt} d\mathcal{V} + \oint_{\mathcal{S}} v\,(u\,n_x + v\,n_y) + \frac{1}{\rho} p\,n_y d\mathcal{S}\right) \qquad (4.7)
\end{aligned}$$

The expressions 2.2 and 2.2 are respectively the horizontal and vertical components of $\mathbf{F}$ made non-dimensional with the free stream dynamic pressure $\frac{1}{2}\rho V_\infty^2$ and the chord length c, thereby representing the sectional drag and lift coefficients.

The numerical integration over the contour is done with the trapezoidal rule

$$\int_{x_j}^{x_{j+1}} f(x)\,dx \approx \Delta x \frac{f(x_{j+1}) + f(x_j)}{2},$$

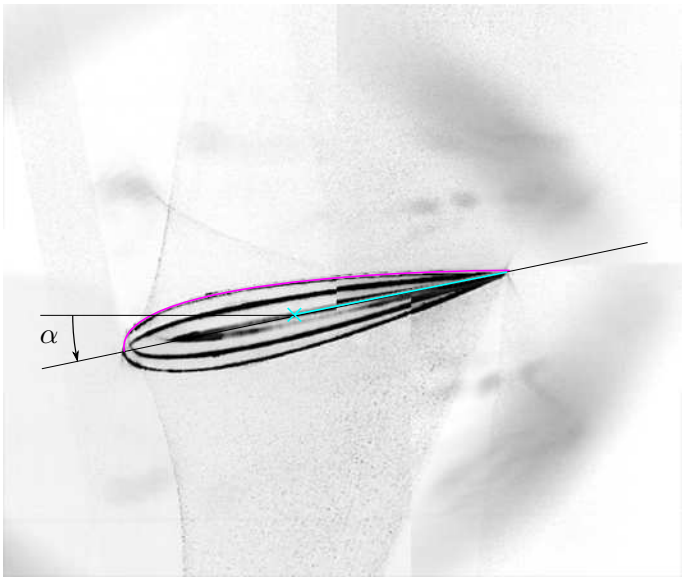

Figure 4.5: Determining the pitch angle from PIV data. Composite image of four PIV frames for one single time instant. Aerofoil is here pitching at 10 Hz in a 15 m/s free-stream flow. At this time instant it was determined to have a pitch angle of -11.4 degrees. (image intensities inverted, i.e. darkest regions are in fact most illuminated)

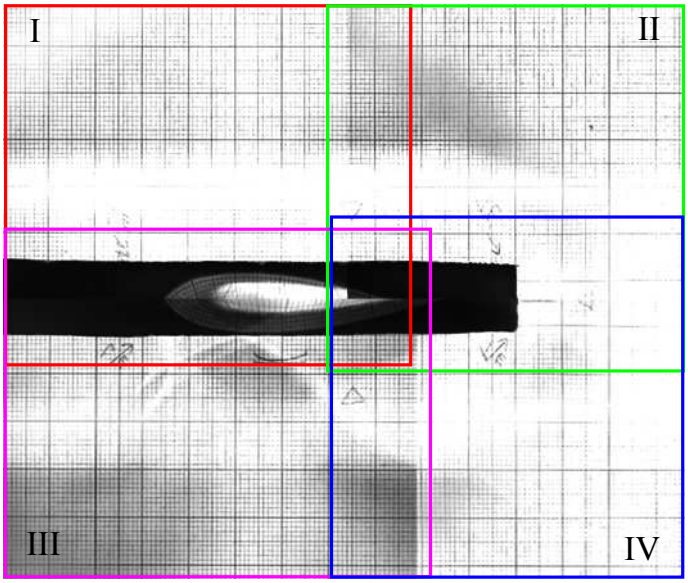

Figure 4.6: Stitched image of the calibration plate.

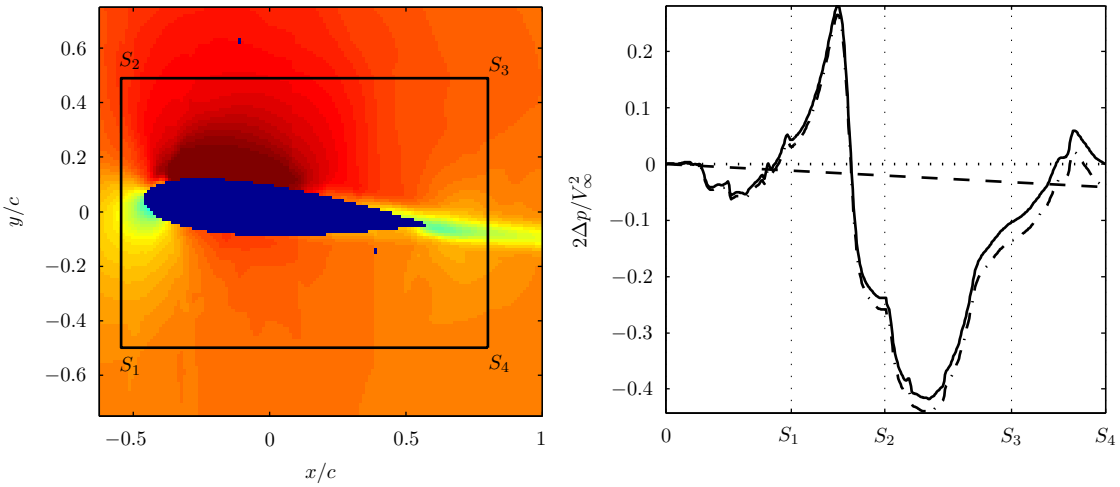

Figure 4.7: Effect of linear correction of the pressure computation over the contour (velocity data are obtained ensemble average of 1000 vector fields for static 5 degree pitch angle).

or for the interval $[a, b]$ divided into N uniform sub-intervals

$$\int_a^b f(x)\,dx \approx \Delta x \left[\frac{f(a)}{2} + \sum_{j=1}^{N-1} f(x_j) + \frac{f(b)}{2} \right],$$

using the MATLAB function `trapz()`.

Pressure term The pressure was determined with 2.3, as mentioned in 2.3. Again by neglecting the viscous term

$$\begin{aligned} -\nabla p &= \rho \frac{\partial}{\partial t}\mathbf{V} + \rho\,(\mathbf{V}\cdot\nabla)\,\mathbf{V} \\ -\frac{dp}{dx} &= \rho\left(\frac{du}{dt} + u\frac{du}{dx} + v\frac{du}{dy}\right) \\ -\frac{dp}{dy} &= \rho\left(\frac{dv}{dt} + u\frac{dv}{dx} + v\frac{dv}{dy}\right) \end{aligned}$$

This pressure gradient can be integrated along the contour. During the evaluation of the contour integral, the pressure is multiplied by the outward pointing normal to the contour, so that the constant pressure term cancels out. It is therefore not necessary to determine the absolute pressure along the contour.

This method of determining the pressure on the contour is susceptible to error propagation. The pressure at each location on the contour is only determined from the pressure at the previous location and the pressure gradient in between. However, that errors are present is easily detectable, since the contour is closed. The pressure at the last location has to be equal to the pressure at the first location. If it is now assumed that the build-up of errors happens evenly along the contour, the pressure can be linearly corrected, as shown in figure 4.7.

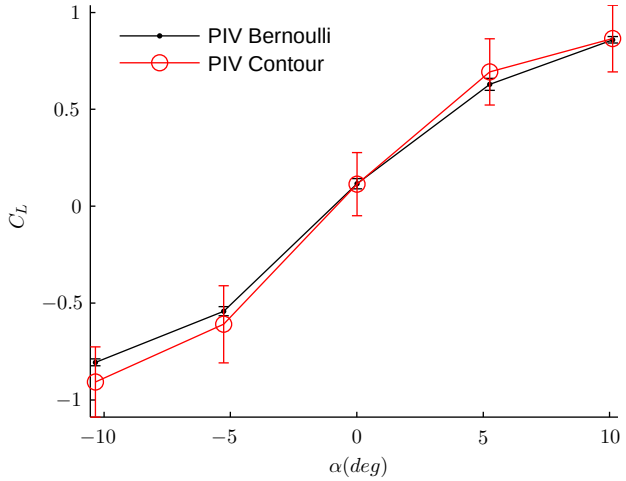

Figure 4.8: Comparison between non-pitching lift curves obtained using different methods for determining the pressure on the contour, i.e. integration of the pressure gradient and using the Bernoulli pressure. The errorbars indicate the fluctuation of the instantaneous forces.

Another way for obtaining a pressure, is using Bernoulli's equation. This method is not affected by error propagation, since the pressure at each location is only determined from the local velocity, $p = \frac{1}{2}\rho V^2$. The drawback of this method is that it is physically not valid for unsteady rotational flows. This method is therefore only applicable to the time-averaged non-pitching cases. Figure 4.8 shows a comparison of the lift curves obtained by using different methods for obtaining the pressure. Applied to the instantaneous flow, a large fluctuation, $\mathcal{O}\left(10^{-1}\right)$, can be observed with the contour integration method, while for the Bernoulli method the fluctuation is an order of magnitude smaller, $\mathcal{O}\left(10^{-2}\right)$. These fluctuations are indicated in figure 4.8 by the errorbars. It shows that the large fluctuation found with the first method is due to the pressure, but to what extent these fluctuations are actual pressure fluctuations is difficult to say. From the Bernoulli pressure method it was known it would not work with unsteady data, so the fluctuations with this method might be underestimated. Additionally the large fluctuations with the pressure gradient integration method could also be the result of the error propagation. The mean values, however, are deemed satisfactory similar, so the pressure gradient integration method is suitable to be used for the evaluation of the oscillating aerofoil cases.

Chapter 5

Results

In this chapter the results of the experiments will be discussed and compared to theoretical data. First the spanwise flow experiments are handled, thereby qualitatively indicating the expected coherence between the PIV measurements and balance measurements. Then in the second section, the static cases are discussed. In the last section the main subject, the forces on the oscillating aerofoil are shown and compared to Theodorsen's pure pitch model.

5.1 Validation two dimensionality of the flow

Experiments were performed to validate the effectiveness of the end-plates on the aerofoil. For proper comparison of the force measurements with the PIV measurements, it has to be investigated to what extent the sectional force from PIV can be expected to be uniform in spanwise direction. This check is performed using a camera positioned perpendicularly to the aerofoil plane. The considered area is positioned approximately at 3 mm distance from the maximum thickness of the aerofoil with one end-plate in the FOV. The presented results are those of the mean flow field which was the average of 1000 frames (1 second).

The result for a 0° pitch angle is shown in figure 5.1. From the contours of the parallel flow it seems that the flow is reasonably uniform (almost straight vertical isolines) in spanwise direction up to a distance of 1% of the aerofoil span from the end-plate. This means the flow is uniform over 98% of the span. The figure of the spanwise component shows a cross flow up to 5% of the test section velocity.

At a pitch angle of 10° figure 5.2 shows a still uniform flow parallel to the mean flow direction over the aerofoil, meaning that up to 98% of the span the flow is uniform. In the wake ($x/c > 1$) the non-uniform area increases significantly.

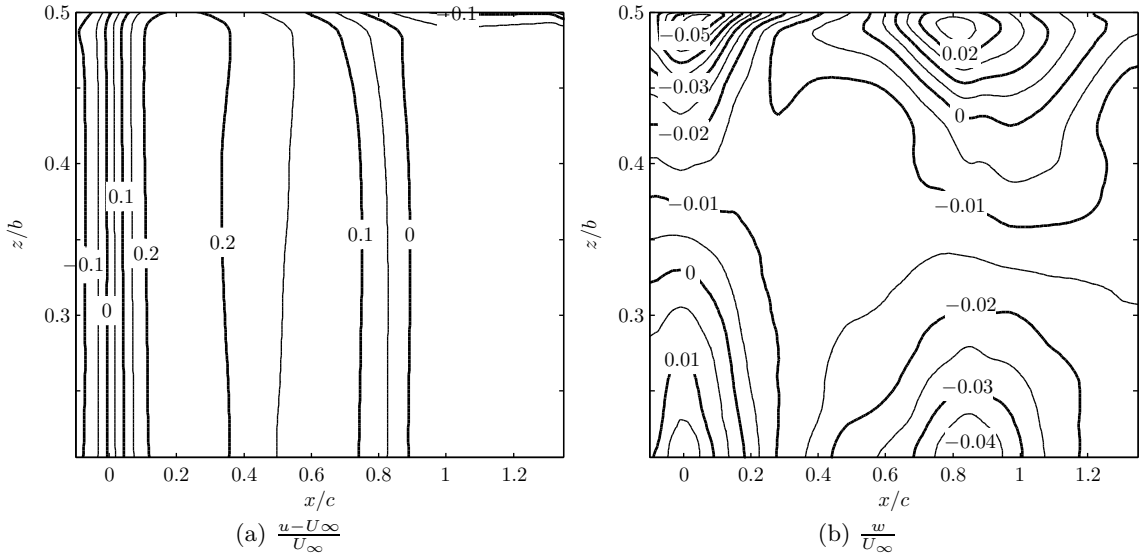

Figure 5.1: Spanwise flow evaluation at 0° pitch angle: Contour lines of parallel (u) and cross flow (w) at a test section velocity of 15 m/s. The vertical axis (z/b) is the spanwise location normalised with the span (360 mm) with the origin mid span, so $z/b = 0.5$ is the location of the end plate. In flow direction the coordinates are normalised with the chord length (80 mm) with the origin at the leading edge. The used contour steps in the figures is $0.05\Delta u/U_\infty$ and $0.005w/U_\infty$ respectively for chordwise and spanwise flow.

5.2 Static case

The static test cases are to serve as indicators of how the setup compares to the conventional static flow measurements. The results are compared to each other and to a theoretic/numeric 2 dimensional flow result computed with XFoil. The data points in the graph are tabulated in appendix B.2.

In the first measurement campaign static experiments were performed at test section velocities between 5 and 30 m/s, using only the force balance for measuring forces. The different lift curves obtained from these experiments are shown in figures 5.3a to 5.3f (solid line with dot markers). The theoretic lift curve obtained from XFoil is shown as a single solid line. To serve as a constant reference in each figure the theoretical slope of 2π is indicated by a dotted line.

For the Reynolds number 27 000, XFoil could not compute values beyond 6 degrees angle of attack. However, for the lowest pitch angles, the measured force and corresponds very well to the forces found from XFoil. Due to the large viscous effects at this low Reynolds number, the aerofoil can produce negative lift for positive angles of attack[1]. Figure 5.3c also shows the lift curves obtained using the PIV technique. All measurements seem to be quite coherent. The distinct change in slope near the lift coefficient of 0.7, as seen in the theoretic 2-D result from XFoil, can also be identified in the measurements.

[1] At very low Reynolds numbers, XFoil shows that laminar separation occurs on the top side of the aerofoil at 0.3 c from the leading edge. The separated flow remains laminar almost to the trailing edge and therefore does not reattach to the aerofoil.

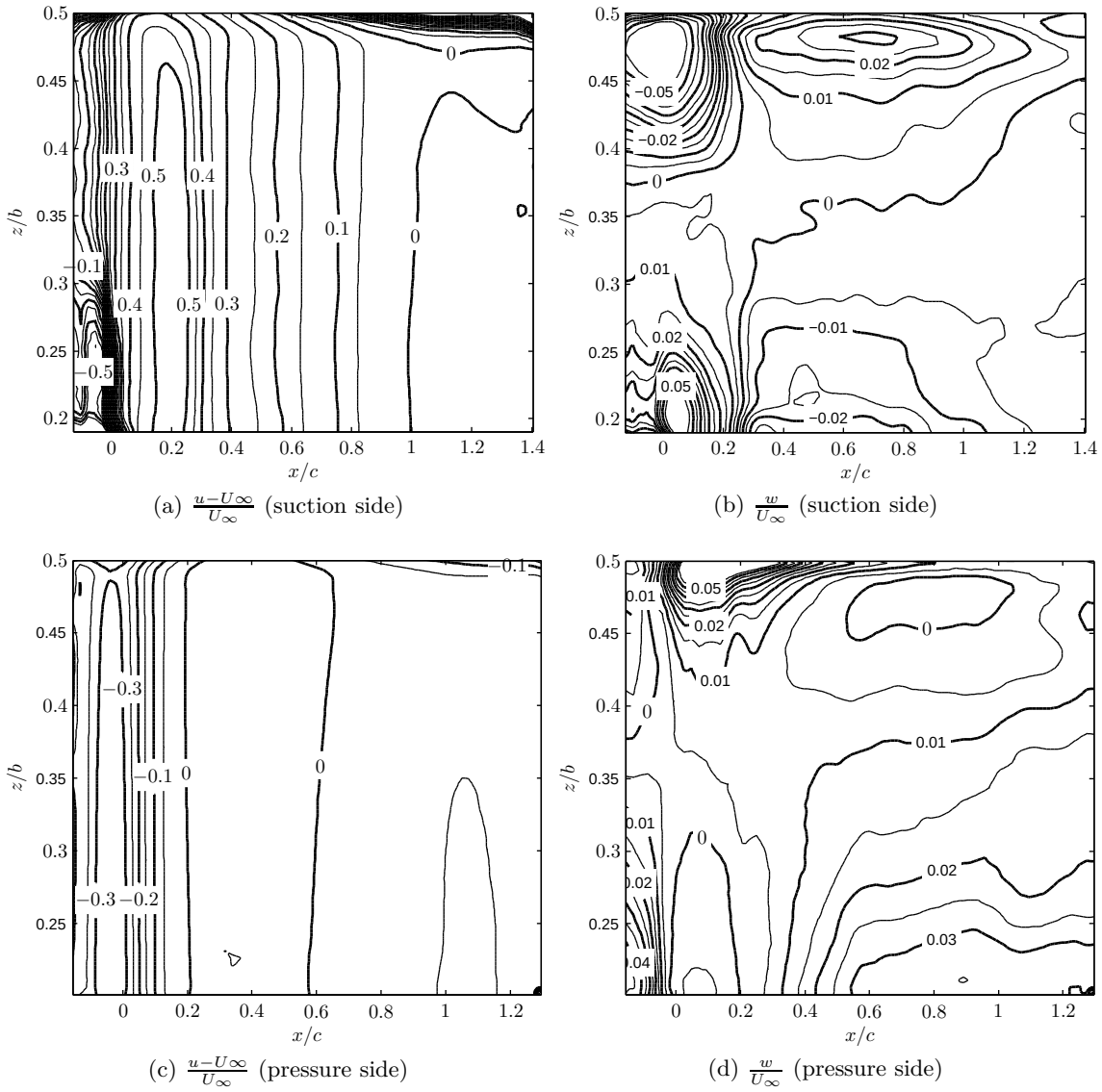

(a) $\frac{u-U\infty}{U_\infty}$ (suction side)

(b) $\frac{w}{U_\infty}$ (suction side)

(c) $\frac{u-U\infty}{U_\infty}$ (pressure side)

(d) $\frac{w}{U_\infty}$ (pressure side)

Figure 5.2: Spanwise flow evaluation at 10° pitch angle: Contour lines of parallel (u) and cross flow (w) at a test section velocity of 15 m/s. The vertical axis (z/b) is the spanwise location normalised with the span (360 mm) with the origin mid span, so $z/b = 0.5$ is the location of the end plate. In flow direction the coordinates are normalised with the chord length (80 mm) with the origin at the leading edge. The used contour steps in the figures is $0.05\Delta u/U_\infty$ and $0.005w/U_\infty$ respectively for chordwise and spanwise flow.

There is, however, a difference between actual slopes of the theoretic lift curve and the experimental. This change can most likely be fully ascribed to the test section being an open jet. It means that when the pitch angle is changed, the entire jet changes direction, which causes the effective angle of attack to decrease. This difference in slope is most noticeable in de first part of the curve (below $C_L = 0.7$). This indicates that the effective angle of attack can not just be calculated/corrected for.

The data points used for the lift curves are averaged values. The fluctuations around these mean values differ depending on the measurement method. The root-mean-square (rms) values of the fluctuations for the direct force measurements are in the range of 0.03-0.04 in lift direction, while 0.01-0.03 in drag direction for a test section velocity of 15 m/s. For lower speeds, these values increase, while they decrease for higher speeds. For the PIV measurements, with the pressure determined from the pressure gradient over the contour, the rms fluctuations are ranging between 0.15 to 0.20 in lift direction and 0.14 to 0.41 in drag direction. This is ten times larger than the direct force measurements. A large part of this increase can be ascribed to the determination of the pressure gradient, since when determining the pressure term with Bernoulli's equation, the fluctuations are in the same range as for the direct force measurements (figure 4.8 and appendix B.2).

Considering the drag measured by the two systems, the results are shown in figure 5.4 for 15 m/s. All aforementioned corrections have been applied to obtain these results. Also the theoretical curve from XFoil is shown in the same figure. For the negative pitch angles, the drag curve obtained from the balance measurements with the aluminium aerofoil correspond quite well will the theoretical curve. Strangely the curve is much higher for the positive angles. This same asymmetry is also observed for the drag curve from the balance measurements with the Makrolon aerofoil, but this curve is shifted up entirely, i.e. it shows higher drag for almost all pitch angles. One explanation for this difference might be in the difference in surface roughness. The aluminium aerofoil had a smoother finish than the Makrolon, because plastics are more difficult to pollish. This effect should, however, be marginal. An explanation for the asymmetry in the curve probably has to be found in mechanical forces at the actuation level, since the aerofoil is symmetric about the chord. The drag curve obtained from the PIV data with the control volume approach is much higher than all three other curves in the figure. Further it does not show the same characteristic shape, expected from a drag curve.

As with the lift-curves the data points shown in figure 5.4 are averages of instantaneous measurements. The fluctuations around these mean values are of the same order as for the forces measured in lift direction. For the force measurements that is in the order of 0.01 while for the PIV measurements it is in the order of 0.1. This means that for the PIV data the fluctuations in the instantaneous results are much larger than the expected variation in the drag curve. Because of these inconsistencies and large uncertainties in determining the drag on the aerofoil, for the remainder of this chapter the results of the drag forces are ignored.

5.3 Pitching cases

The following section will discuss the results obtained for the oscillating cases. First the results from the experiments with the Makrolon aerofoil are shown. For these experiments

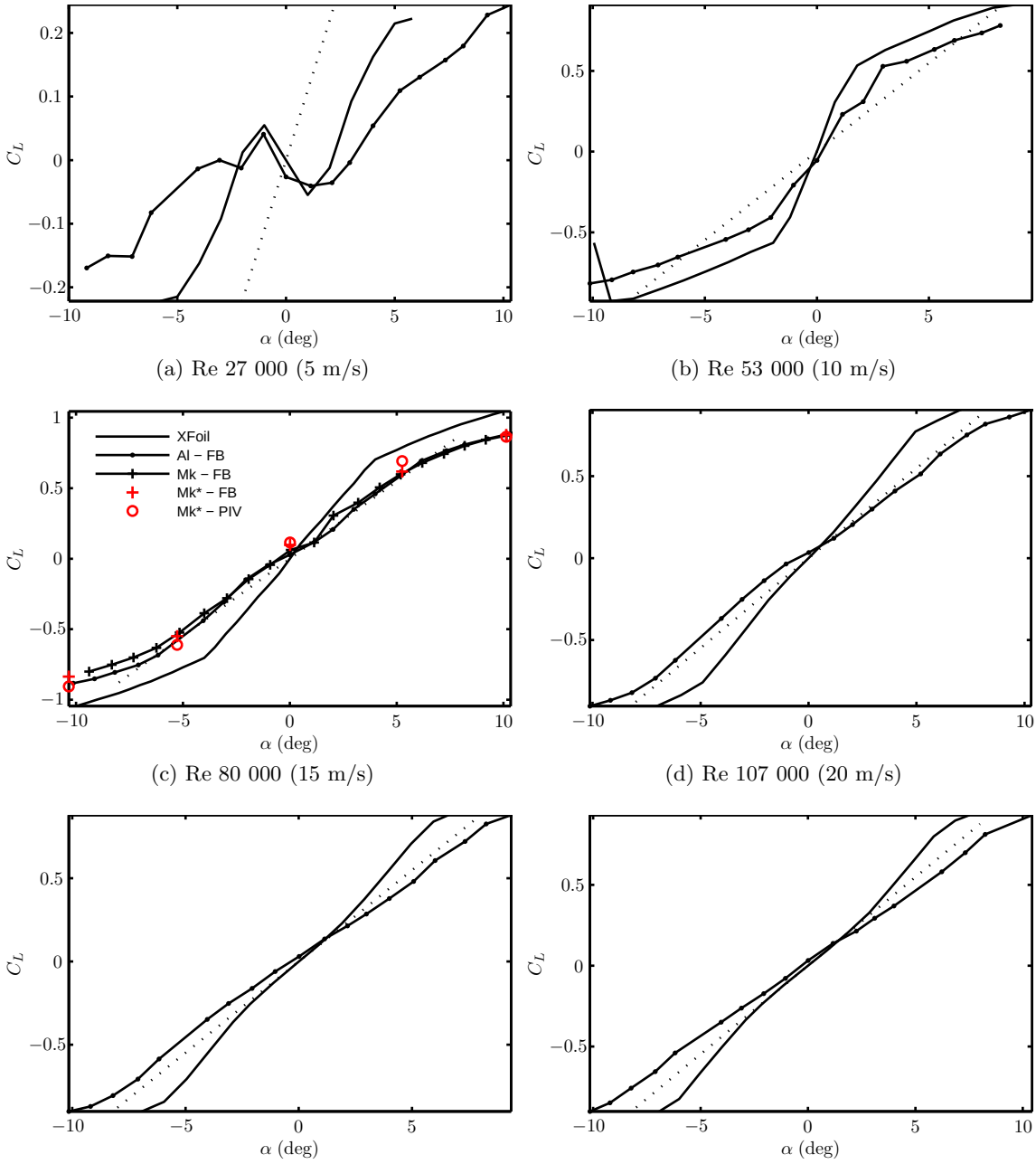

(a) Re 27 000 (5 m/s)

(b) Re 53 000 (10 m/s)

(c) Re 80 000 (15 m/s)

(d) Re 107 000 (20 m/s)

(e) Re 133 000 (25 m/s)

(f) Re 160 000 (30 m/s)

Figure 5.3: Lift curves of the NACA0018 for different Reynolds numbers.

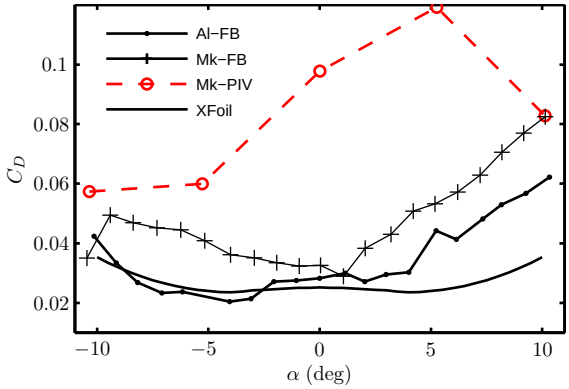

Figure 5.4: Drag curve of the NACA0018 aerofoil as measured by the force sensors and the PIV method. Re 80 000 (15 m/s)

both PIV and balance measurements were performed simultaneously. The problems with the unreliable clock, as discussed in chapter 4.1.5, can be avoided for these measurements, since the angle of attack could also (and more directly) be obtained from the PIV images.

In the second part the results from the balance measurements will be added. Also the outcome of the measurements with the aluminium aerofoil, were the full range of possible frequencies and velocities was tested, will be discussed. Here however, the unreliability of the clock could not be compensated for by using visual tracking of the aerofoil, so phase information is disregarded for these measurements.

5.3.1 PIV forces for the oscillating aerofoil

Figure 5.5 shows the pitch angle and the pitch velocity against time, where the time is normalised by the cycle period, starting at the upstroke through zero. Clearly the motion of the aerofoil is not the same as predicted based on the actuator motion (figure 3.6). This can be explained by the inertia of the aerofoil and the twisting of the axis. This effect is covered in chapter 4.1.5. What is quite evident from these figures is that the aerofoil obtains a higher speed during the downstroke than during the upstroke. In the case of 20 Hz, the maximum speed during the downstroke is actually double the speed during the upstroke, explaining the asymmetric pitch motion. Additionally, during the upstroke the change in velocity is much less severe; for the 20 Hz case it seems to be almost constant relative to downstroke motion. Another thing that should be noted, is the difference between 10 Hz and 20 Hz in the shape of the pitch velocity plot. For 10 Hz, starting from the lowest angle, the pitch speed increases to a local maximum before crossing the zero degree angle. The maximum pitch velocity during the upstroke than occurs nearly at (though just after) the crossing. A maximum velocity through the zero degree angle is expected of a nearly sinusoidal motion. The 20 Hz case already obtains maximum velocity well before crossing the zero degree angle. It then has a local maximum after the crossing, right before the maximum positive pitch angle.

The measured forces can also be displayed as a function of time, as shown in figure 5.6. In this figure both the balance measurements and PIV measurements are plotted. The balance data has been corrected for the actuation force and for frequency responses, as

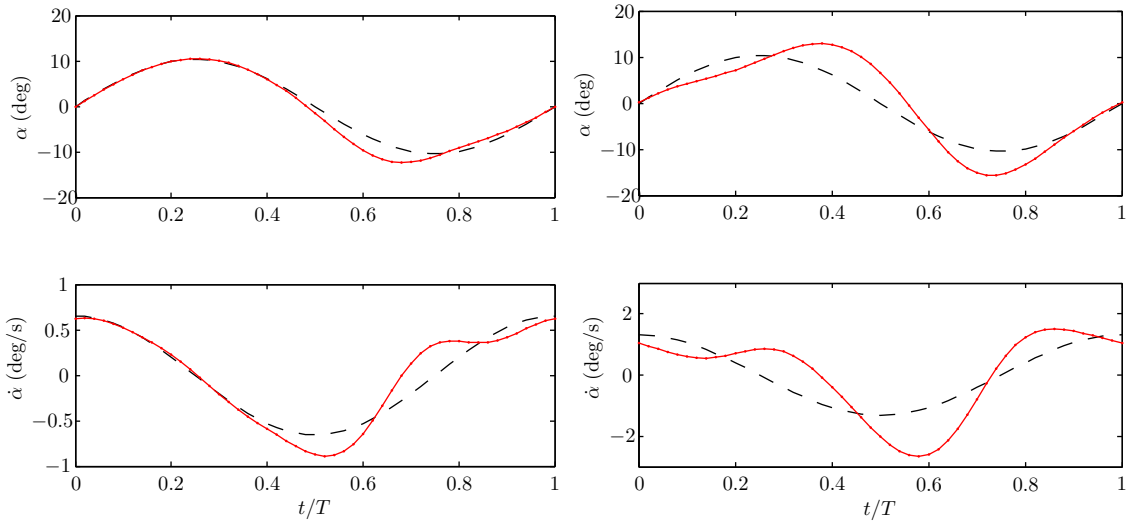

Figure 5.5: Actual aerofoil pitch motion from PIV images: pitch angle and pitch velocity for left 10 Hz and right 20 Hz, with the Makrolon aerofoil. The dashed line represents the theoretical motion expected in advance. The solid line is the actual motion as captured by the PIV cameras.

explained in chapter 4.1. Additionally, the force measured during pitching in still air has been subtracted, thereby assuming no significant aerodynamic forces are present in zero free stream flow[2]. For the 10 Hz case the experiment has been repeated three times. Displayed are the results of the average of these experiments. For the 20 Hz case, only two repetitions were performed, so the results here are the average of those two. The PIV results are the phase-averaged results for each measurement, with the forces determined as described in chapter 4.2.3. The length of each dataset is one second. The separate runs result in independent angle of attack measurements, so the PIV results shown in figure 5.6 contain 600 unique points for the 10 Hz case and 400 for the 20 Hz case.

Displayed in figure 5.7 is solely the PIV data in a way similar to the conventional static lift curves. The data is fitted with a Fourier fit of sixth order (both measured forces and measured angle of attack). The arrows point the direction of time. What stands out is that for the lower angles the upstroke and downstroke are very close to each other. At the maximum angles a larger loop is present, which is similar to a hysteresis loop. Different from a conventional hysteresis loop, however, the lift curve is not symmetric. The downstroke is, for both 10 Hz and 20 Hz, nearly a straight line. Near the maximum pitch angle, the curve bends upward (so less force). Continuing, during the upstroke, the curve is more irregular. Most clearly for the 20 Hz case, near the maximum pitch angle in the upstroke, the slope of the curve increases (instead of continuing in a straight line). Asymmetry in the lift curve is of course expected, since the pitch motion itself is severely asymmetric.

In figure 5.8 the lift curves predicted with Theodorsen's function (chapter 2.2, equation 2.1) are added to the plots. Here the pitch motion, as described by a second order Fourier fit, is used. For the 10 Hz case it can bee seen that the general shape of the curve is

[2]Placing the set-up in a vacuum chamber has been considered, but the size of the complete set-up made this impractical.

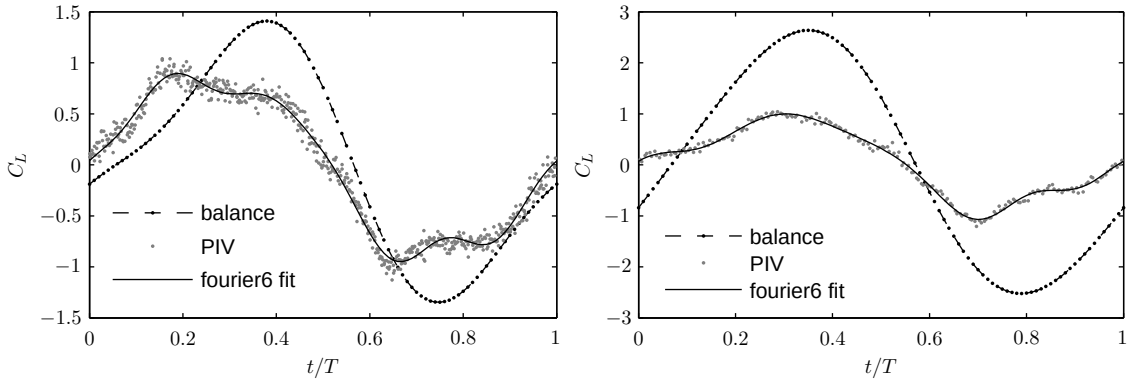

Figure 5.6: Aerodynamic force against the pitch cycle, starting at the upstroke through zero. Left for 10 Hz, right for 20 Hz. Balance measurements (corrected for frequency amplifications and residual forces at 0 m/s subtracted).

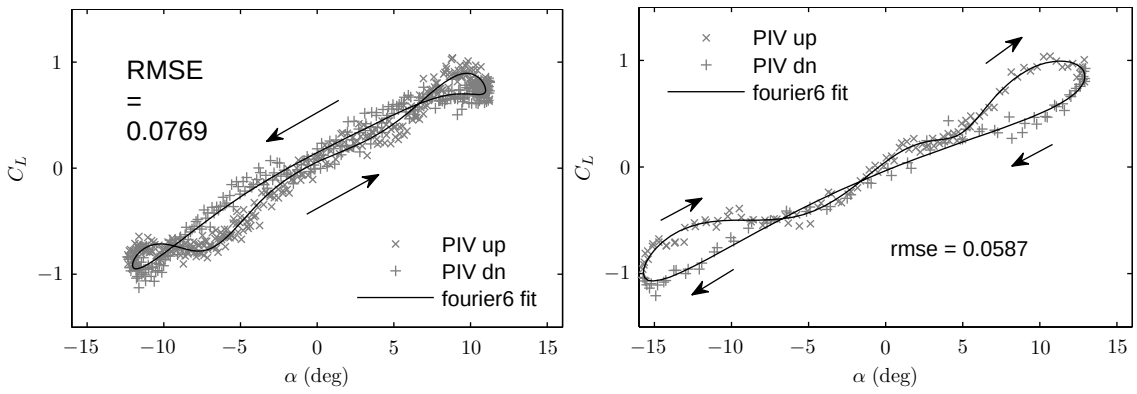

Figure 5.7: Dynamic lift curve from phase averaged PIV measurements. Left the 10 Hz case and right 20 Hz.

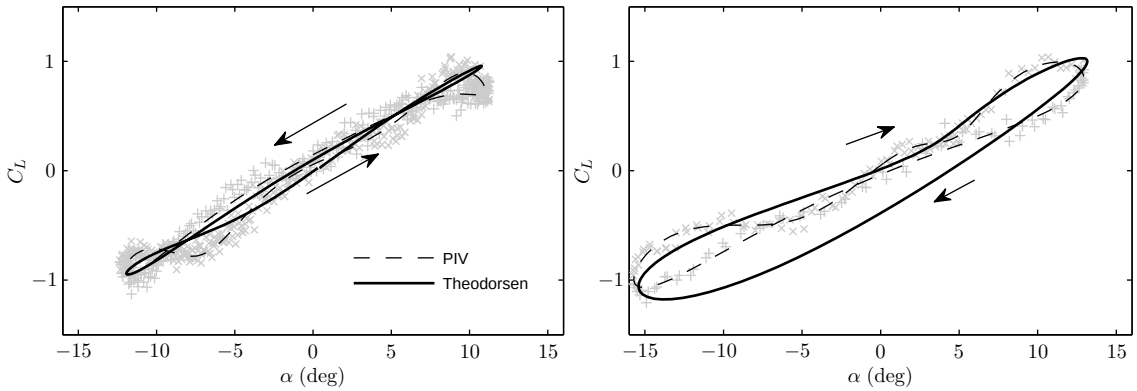

Figure 5.8: Theodorsen's function for $k = 0.168$ (10 Hz, left) and $k = 0.335$ (20 Hz right) based on the actual measured pitch angles.

similar to that found from PIV. Starting mid-upstroke, the force is lower than during the downstroke. At a certain point the upstroke curve crosses the down stroke curve, creating a loop, though, not as large as with the PIV curve. The downstroke then is a fairly straight line, just as with the PIV measurements. Another loop is created at the reversal of the motion. The PIV results then show a large outlier that is not found in the Theodorsen curve. The extrema of the curves correspond very well, near a C_L value of 1. Continuing with the 20 Hz case, there is a relative good agreement between the PIV measurements and the Theodorsen curve during the upstroke. There is, however, a large difference in the downstroke. During the downstroke the Theordorsen curve shows a more convex character. To explain the differences, it should be kept in mind that Theodorsen's theory was a solution to a potential flow problem, where the flow separates at the trailing edge and where all vorticity in the wake is on a single straight line. In the experiments the flow stays attached to the aerofoil during the upstroke, but near the highest pitch angle, when the pitch velocity decreases, the aerofoil stalls towards the leading edge. The lift is decreased more rapidly than predicted by Theodorsen's model. Another effect might be because of the open-jet test section. From the static measurements, the hypothesis arose that the jet might change direction under influence of the pitch angle. This would reduce the effective angle of attack. The oscillating case are likely also subjected to this effect, but now in a time dependent way.

Figures 5.9 and 5.10 show the magnitude of the velocity field around the aerofoil, respectively at 10 Hz and 20 Hz, for the pitch angles -10°, 0° and -10° during the upstroke and during down stroke. The are displayed in order as encountered during a cycle. In the 10 Hz case there is not a much difference between the upstroke and the down stroke, i.e. flipping the y-axis of the down stroke images, results in almost the same images as with the upstroke. What could be noted, is the difference between wakes during the upstroke and the downstroke. Except for -10°, the wakes seem to be more 'turbulent' during the upstroke. For 20 Hz a similar analysis can be made. Again the wake in the upstroke seems to be more 'turbulent' than that in the downstroke. This more irregular wake during the upstroke, can be explained by the fact that the upstroke takes more time.

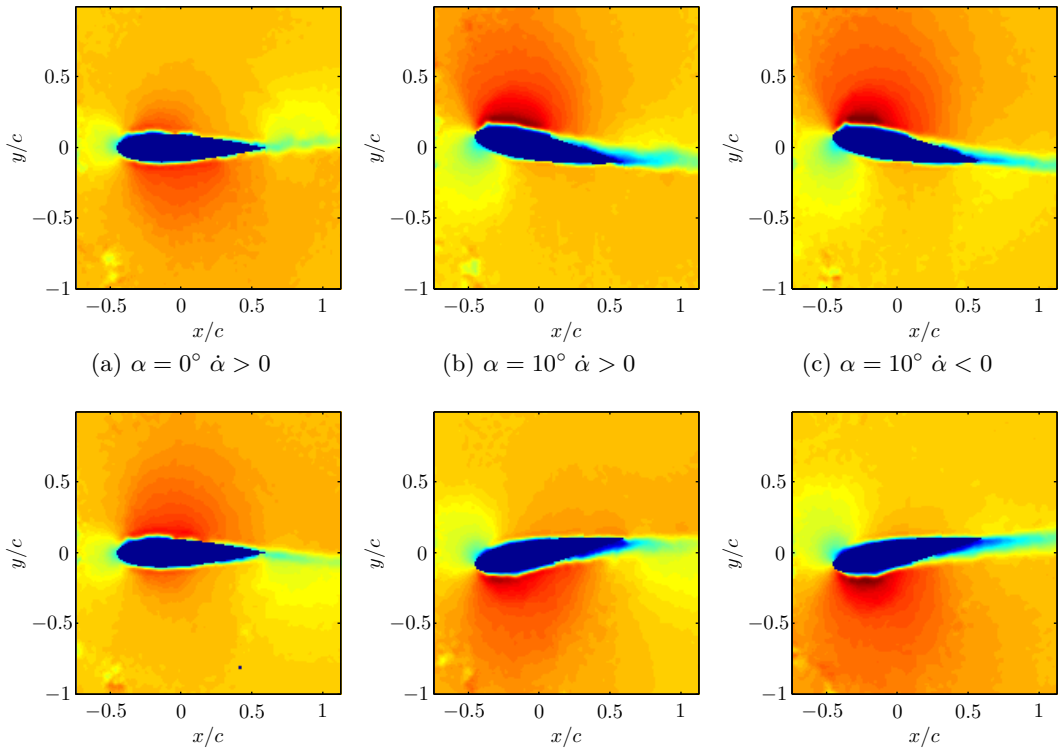

(a) $\alpha = 0^\circ\ \dot{\alpha} > 0$ (b) $\alpha = 10^\circ\ \dot{\alpha} > 0$ (c) $\alpha = 10^\circ\ \dot{\alpha} < 0$

(d) $\alpha = 0^\circ\ \dot{\alpha} < 0$ (e) $\alpha = -10^\circ\ \dot{\alpha} < 0$ (f) $\alpha = -10^\circ\ \dot{\alpha} > 0$

Figure 5.9: Magnitude of the flow velocity around the aerofoil oscillating at 10 Hz. The velocity scale is from zero (dark blue) to 1.5 times the free stream velocity (dark red).

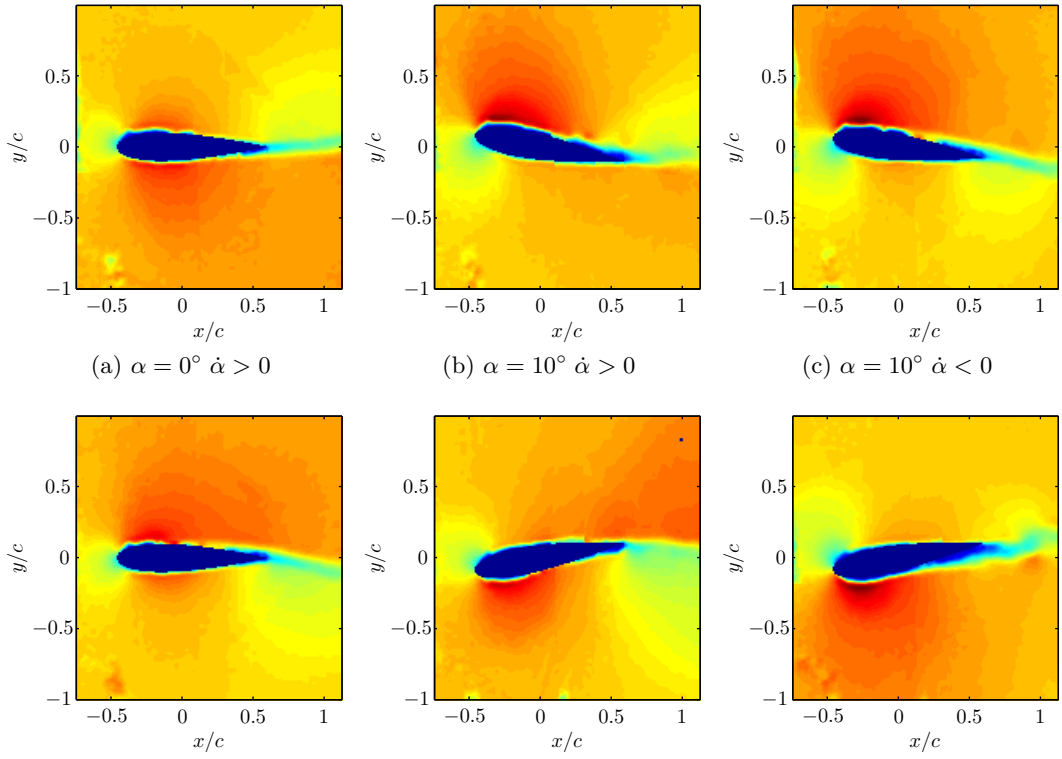

(a) $\alpha = 0^\circ\ \dot{\alpha} > 0$ (b) $\alpha = 10^\circ\ \dot{\alpha} > 0$ (c) $\alpha = 10^\circ\ \dot{\alpha} < 0$

(d) $\alpha = 0^\circ\ \dot{\alpha} < 0$ (e) $\alpha = -10^\circ\ \dot{\alpha} < 0$ (f) $\alpha = -10^\circ\ \dot{\alpha} > 0$

Figure 5.10: Magnitude of the flow velocity around the aerofoil oscillating at 20 Hz. The velocity scale is from zero (dark blue) to 1.5 times the free stream velocity (dark red).

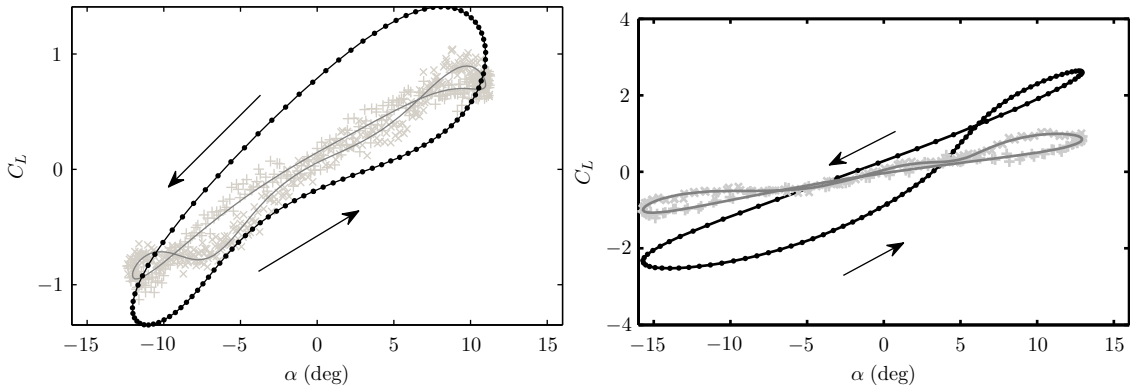

Figure 5.11: Dynamic lift curve from force balance measurements (corrected for frequency amplifications and residual forces at 0 m/s subtracted). In the background a single phase averaged PIV measurement. Left the 10 Hz case and right 20 Hz.

5.3.2 Balance measurements during oscillation

In figure 5.11 the results of the balance measurements have been added to figure 5.7. Clearly they do not match the PIV result. Besides the obvious difference in magnitude, also the shape of the curve is very different. Except for the loop in the 20 Hz result (which is actually in the same direction as the loop in the PIV lift curve), no hysteresis loops are present. With a little imagination, one similarity could be identified: the lift curve for downstroke is also for the balance measurements more linear than for the upstroke. The counter clockwise direction of the loop in the 10 Hz case does correspond to what was expected with Theodorsen's function, but the loop is far too wide. The loop in the 20 Hz case is for the main part also counter clockwise, which does not correspond with Theodorsen's function.

For the data obtained during the first measurement campaign, large deviations in the timing between the force measurement and the pitch angle measurement were observed, as was described in section 4.1.4, where table 4.5 gives a quantification of this uncertainty. Here it can be seen that the maximum deviation from the mean phaseshift is only 3.37 ms for the 3 Hz case at 25 m/s, which is much lower than at the other velocities. This small deviation raises the hope that the timing error is only small. The actuation force that was observed in the measurements in still air become necligible at these higher velocities. Therefore the result of these specific measurements are displayed in figure 5.12a. Also the lift curve obtained with Theodorsen's function, for that specific pitch motion, is shown. The curves are very similar. The slope of the loop is slightly lower for the balance measurements, but this can be expected, considering the open-jet effects. The effective angle of attack is reduced, so that also the extrema of the experimental curve are lower.

Another case shown in figure 5.12b, with a pitch frequency of 9 Hz and at a velocity of 30 m/s, was selected on the same criteria as the previous case. Here a more distinct asymmetry becomes appearent. For a considerable part of the loop the two curves are on top of each other, but near the end of the upstroke the experimental curve shows a sudden increase of the lift force. The maximum value obtained with the balance measurements is significantly higher than expected from Theodorsen's function. During the downstroke it then takes up to the zero pitch angle before the two curves meet again. The remaining

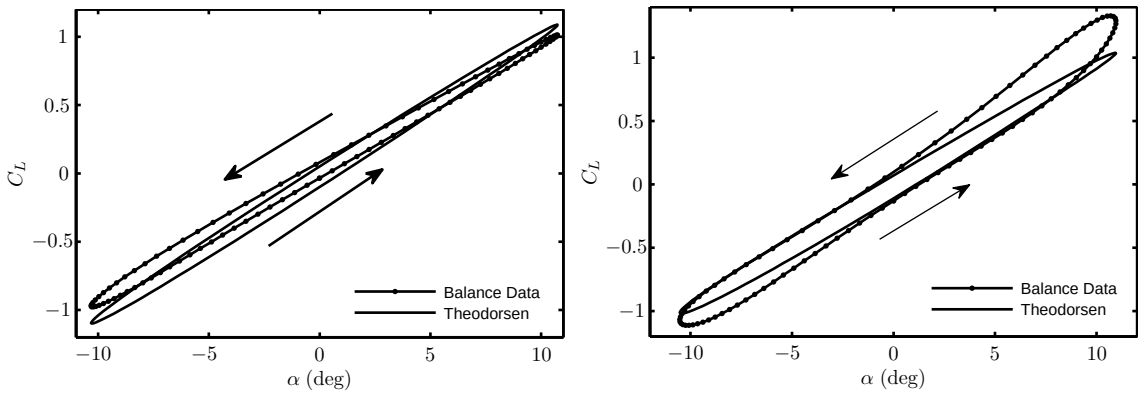

(a) 3 Hz at 25 m/s (Re = 132 000; k = 0.030)

(b) 9 Hz at 30 m/s (Re = 155 000; k = 0.075)

Figure 5.12: Lift curves from balance measurements with the oscillating aluminium aerofoil compared to Theodorsen's prediction method. The curves show the average lift curves from each five separate measurements. The presented cases were selected because the phase deviations between separate measurements was only small and the resulting mean phase shift resulted in a curve similar to that obtained with Theodorsen's function.

part of the downstroke the two curves are again overlapping. Then at the end of the downstroke, the same overshoot is observed, but now less extreme.

To demonstrate the sensitivity to the phaseshift, figure 5.13a shows again the case of a pitch frequency of 3 Hz at 25 m/s, while figure 5.13b shows the results from the measurements at 3 Hz and 15 m/s. As can be observed, for the measurements at 25 m/s the measurements are all close together and seem to only significantly differ from Theodorsen by amplitude. Now when observing the second figure, for 15 m/s, it seems that the differences are still not very large. There is, however, a larger variation between the phases of the individual measurements. The most delayed measurement actually crosses the zero value approximately at the same time. The curve of the mean value is shifted to the left, though. This shift of approximately 10 ms, has the result that the lift force during the upstroke would be higher than during the downstroke, opposite to what is observed from the prediction from Theodorsen's function.

Because the phaseshift appears to be the main problem, figures 5.14 and 5.15 show the extrema and mean of all balance measurements combined in a contour plot. These results have not been corrected for a residual force at 0 m/s, because of the uncertainty in the synchronisation. This will, however, only be significant for low flow velocities, as it should be independent from the flow velocity. The actual contours are constructed by interpolation using a radial basis function. At the measurement locations in the plot, the contour has the actual value of that measurement, but the further away from that point, the less reliable the contour will be. This said, looking at figure 5.14, it looks like the contours are stretched horizontally, with a distinct peak near 12 Hz. The horizontal alignment suggests that the lift coefficient depends primarily on frequency. This implies that the registered force is not just an aerodynamic force, but also an inertial force. The fact that there is a frequency for which the force coefficient has a maximum suggests a resonance frequency, which also indicates that the measured force is not purely an

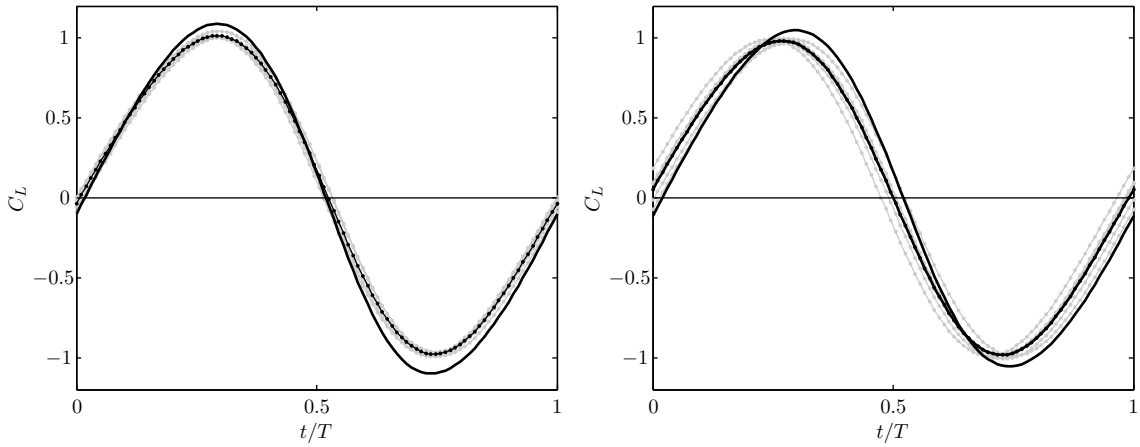

(a) 3 Hz at 25 m/s (as in 5.12a)

(b) 3 Hz at 15 m/s

Figure 5.13: Lift force from balance measurements during a pitch cycle for 3 Hz, showing the effect of the timing uncertainty. All 5 measurements are presented in grey. The lift curve from the averaging the phaseshifts is the dark line. Theodorsen is shown as the solid line without markers.

aerodynamic force.

In figure 5.16a the the amplitude of the lift coefficient from Theodorsen's prediction method is shown. The contours are clearly straigth lines. Considering that the reduced frequency, k, is proportional to the ratio of pitch frequency and free stream velocity, it follows that the amplitude is just a function of the reduced frequency. Because in the experiment the motion of the aerofoil was by far not perfectly sinusoidal, figure 5.16b shows the lift coefficient amplitudes corresponding to the pitch motion of the experiment. The variation of this pitch motion was frequency dependent, so the lines get severely distorted. The result is however still not comparable to the results from the balance measurements, especially when looking at the magnitude. The balance measurements are consistently and significantly higher.

Then figure 5.15 shows the mean force coefficient in lift direction. Here the contour lines are stretched vertically, which than means that apparently this mean force is primarily a function of the flow velocity. For increasing velocities the mean force increases. So this than suggests a significant part of this force is aerodynamic. With the method of Theodorsen, no significant mean force is found. There are a few explanations to think of: one is that the angle of attack measurement is biassed. This angle would then also not be taken into account with Theodorsen's method. A second explanation is that the aerofoil in fact does generate a resultant force, due to viscous mechanisms not incorporated in the potential flow solution.

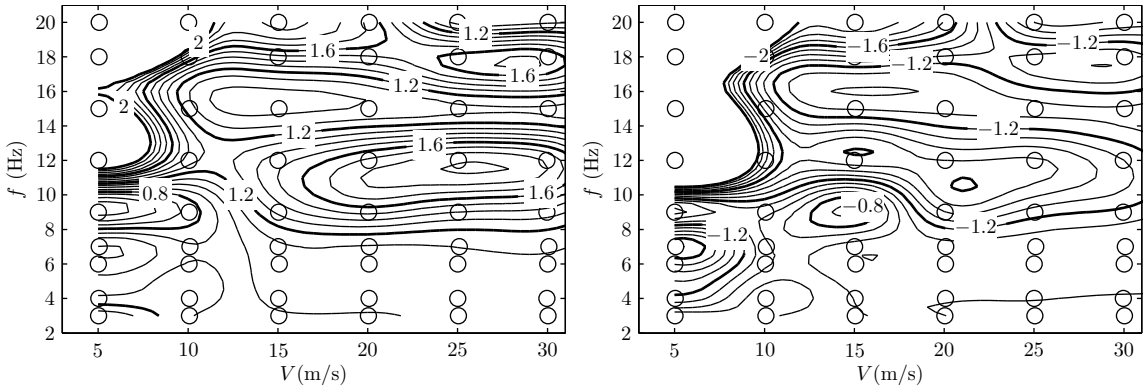

(a) $C_{L,\max}$ (b) $C_{L,\min}$

Figure 5.14: Extrema of the lift coefficient for the full range of Reynolds numbers and frequencies obtained using the balance data of the aluminium aerofoil. The results of the 0 m/s measurement are not subtracted.

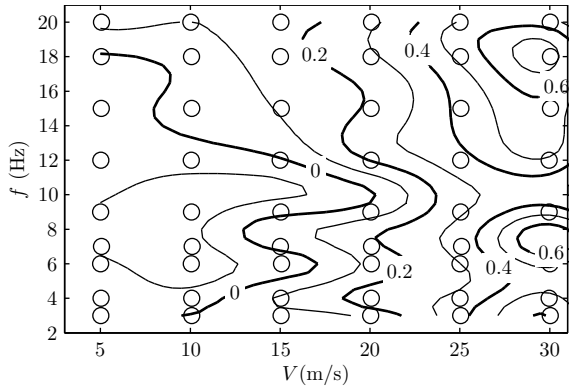

Figure 5.15: Cycle means of the lift coefficient for the full range of Reynolds numbers and frequencies obtained using the balance data of the balance and the aluminium aerofoil. The results of the 0 m/s measurement are not subtracted.

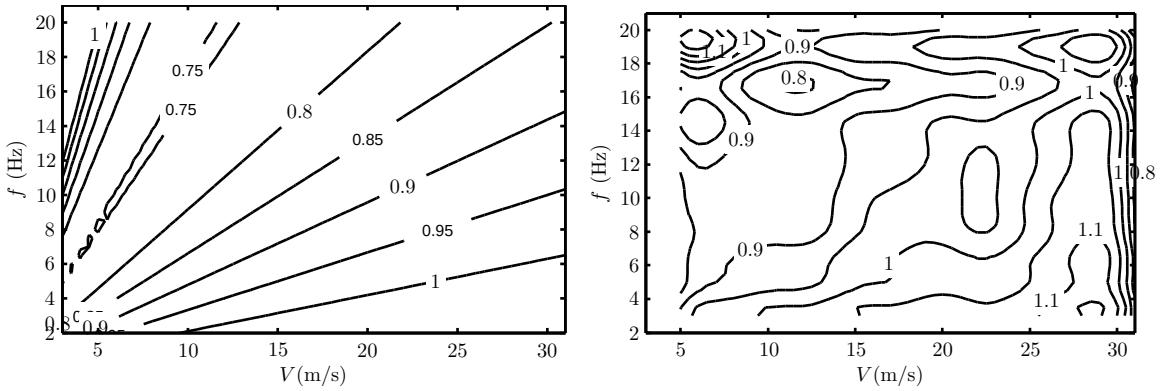

(a) (b)

Figure 5.16: Predicted amplitude of C_L, using Theodorsen's function. 5.16a, for a perfect sinusoidal motion with 10.1° amplitude, showing straight lines (the slopes proportional to the reduced frequency $k \propto f/U$). In 5.16b the experimentally observed pitch motion is used with Theodorsen's function.

Chapter 6

Conclusions

The main goal of this project was to construct a wind tunnel set-up which could be used for validating forces derived from Time-Resolved PIV measurements on an oscillating pitching aerofoil using direct force measurements. From the results found in chapter 5 different conclusions could be drawn. Based on those conclusions, some recommendations for future work are given in chapter 7.

First of all for the cases wherein the aerofoil was stationary submerged in the flow, the lift forces derived from PIV data on average show good agreement to the force measurements. Also the typical shape of the theoretic 2-D solution found from XFoil can be identified. This sudden change in the lift curve slope appears for approximately the same lift coefficient. The slope of the experimental lift curve is always more shallow than the theoretical curve. This is most likely explained by the fact that the experiments were conducted in an open jet facility. The aerofoil changes the direction of the flow, thereby reducing the effective angle of attack. At the start of this paragraph, it was stated that the PIV results on average agree with the mechanical results. However, the drawback of the used method, a contour integration of the momentum equation, is the large deviation from this mean result. The fluctuations of the PIV results are about 5 times larger than those found from the balance measurements. From these results it could therefore be concluded that for the static case the direct force measurements are more reliable than the PIV method.

In drag direction, the results of the stationary experiments were less convincing. Again the direct force measurements are showing the best results, were the drag curve at least has a shape that is more or less similar to a familiar parabolic drag curve. However, the curve of the experiments with the Makrolon aerofoil lies approximately 0.01-0.02 higher than the aluminium aerofoil. The mean values of the PIV measurements were nowhere near the drag curves of the direct measurements and more important, they were not showing a typical drag curve. The fluctuations were of the same order of magnitude as with the lift forces and therefore of the same order of magnitude of the drag force itself. It was therefore decided not to consider the drag any further.

Continuing to the oscillating cases, a problem arised by the aerofoil not folowing the expected motion, as shown in figure 3.6, but a more severely asymmetric motion as

shown in figure 5.5. It was found that this difference could be well explained by twisting of the pitching axis due to inertial loads. This effect was only as severe for the Makrolon aerofoil, due to its higher inertia. For the cases with the aluminium aerofoil, where the precise pitch data from PIV was not available, the twisting axis correction model would therefore be sufficient to estimate the real pitch angles for those cases.

From the oscillating aerofoil PIV measurements, interesting lift curved emerged. The interpretation of this lift curve is difficult, since the aerofoil motion was not perfectly sinusoidal. However, inserting the motion as a sum of harmonic functions into Theodorsen's model provides a lift curves that share characteristics with the experimentally determined curves from PIV. Especially the 10 Hz case ($k = 0.168$) is very similar. The small excursions of the experimental curve could be explained by separation effects, but might also be influenced by the side effects of an open-jet test section.

The original goal of this project was to validate PIV measurements with direct force measurements. However, performing force measurements on an aerofoil pitching at such high frequencies proved to be difficult. First of all the actuation forces were larger than anticipated. Additionally an unresolved timing problem occured. This not only made it difficult to link individual measurements, but also to link the pitch angle measurements to the force measurements. The third problem arose with natural frequencies of the combined system of load transfering platforms and the aerofoil, being excited by the pitch motion. Frequency response models did improve the results to more credible values. These results were, however, not comparable to the results obtained from PIV and the predicted results from Theodorsen. Additionally, the shear magnitude of corrections applied to the force measurement data, is so large that an error estimation would reveal an uncertainty of the result larger than the actual value. Other indicators for the unreliability of the force measurements are provided by figures 5.14 and 5.15, which imply that there is no relation between the lift coefficient and the reduced frequency, while a relation is expected based on Theodorsen's model.

Based on these observations, the conclusion would be that the project has been unsuccesful at validating the PIV method for determining the forces on a pitching aerofoil. However, this investigation has also shown that the PIV method does give results similar to predictions using Theodorsen's function.

Chapter 7

Recommendations

Based on the conclusions in chapter 6, several recommendations will be presented here.

The most important concerns the direct force measurements on the pitching aerofoil. The sensors used were load cells based on the bending properties of an aluminium beam. This means the amount of force is based on the displacement of the aerofoil. While this is inevitably the case with any type of force sensor, this particular solution requires a relative large displacement. Additionally the way that they were mounted, allowed for a considerable amount of movement. To avoid this problem, piezoelectric load cells could be used, which require much less displacement. These sensors were considered when designing the current set-up, but they are much more expensive compared to the bending beam sensors. Allowing less displacement also increases the natural frequency of the system, reducing the need for frequency response corrections.

Still considering the improvement of the direct force measurements, the pitch angle determination should be improved. First of all the timing of the pitch angle measurement and the force measurement should be synchronised. Further, the pitch angle should be measured at the aerofoil itself, possibly with an additional camera for motion tracking. Also, twisting of the aerofoil and/or axis should be minimised, for example by actuation at both ends of the aerofoil. This again was considered for the current project, but due to the requirement of optical acces, it was not continued. Also double actuation requires very exact synchronisation of the actuators, which is increasingly difficult at higher frequencies. Another option is using actuation at the mid-span location, but then an additional object is will be introduced to the flow.

With the static measurements, the direct force measurements appeared to give better results than the applied PIV methods. The most likely cause is the method of determining the pressure at the contour. A few attempts have been made to find a method less prone to error propagation (not reported in this thesis), but without succes. Bernoulli's equation, as used by Kurtulus et al. [2007] is not suitable in this situation, since the time derivative of the velocity potential is not negligible. Further the poor results for the drag force from PIV were to be expected. For steady flows, a wake survey approach is commonly used, where only the contour through the wake is used. There is, however, not a time

dependent term in that expression. It was chosen not to continue on this subject during this thesis, but it should be investigated if this approach is or can be made suitable for use with unsteady flows.

The lift curve from the static measurements indicated a possible deflection of the open-jet. To prevent this effect from occuring, one could add walls to the set-up. In that case (unsteady) wall corrections have to be applied to the results. Also blockage effects then have to be considered, most likely also being functions of time.

References

Anderson, J. D. J. (2007). *Fundamentals of Aerodynamics* (Fourth ed.). McGraw-Hill Education.

Casimiri, E. W. (2006). *Evaluation of a non-intrusive airfoil load determination method based on PIV*. M.sc. thesis, TU Delft, The Netherlands. Available from `http://www.lr.tudelft.nl/aerodynamics`

Hulshoff, S. J. (2009). *Lecture notes Aeroelasticity Course AE4930 - v09.*

Kang, C., Aono, H., Trizila, P., Baik, Y., Rausch, J., & Bernal, L. (2009). Modeling of Pitching and Plunging Airfoils at Reynolds Number between 10000 and 60000. *AIAA*(June), 1–23. Available from `http://shyylab.engin.umich.edu/files/papers/AIAA-2009-4100-988-KangSanAntonio.pdf`

Kuik, D. J. (2007). *Tomographic PIV investigation of a turbulent boundary layer*. Master thesis, TU Delft. Available from `http://www.lr.tudelft.nl/aerodynamics`

Kurtulus, D., Scarano, F., & David, L. (2007). Unsteady aerodynamic forces estimation on a square cylinder by TR-PIV. *Experiments in Fluids*, *42*(2), 185–196. Available from `http://www.springerlink.com/index/CM363615KT726W6H.pdf`

McCroskey, W. (1982). Unsteady airfoils. *Annual Review of Fluid Mechanics*, *14*(1), 285–311. Available from `http://arjournals.annualreviews.org/doi/abs/10.1146/annurev.fl.14.010182.001441`

Nati, A. (2010). *Time-resolved 3D PIV analysis of a laminar separation bubble on an unsteady pitching airfoil*. Master thesis, TU Delft.

Noca, F. (1997). *On the evaluation of time-dependent fluid-dynamics forces on bluff bodies*. Phd, California Institute of Technology.

Ol, M., Bernal, L., Kang, C., & Shyy, W. (2009). Shallow and deep dynamic stall for flapping low Reynolds number airfoils. *Experiments in Fluids*, *46*(5), 883–901. Available from `http://www.springerlink.com/index/N5685441W66066G2.pdf`

Oudheusden, B. van, Scarano, F., Roosenboom, E., Souverein, L., & Casimiri, E. W. (2007). Evaluation of integral forces and pressure fields from planar velocimetry data for incompressible and compressible flows. *Experiments in Fluids*, *43*(2-3), 153–162. Available from http://www.springerlink.com/index/10.1007/s00348-007-0261-y

Panda, J., & Zaman, K. (1994). Experimental investigation of the flow field of an oscillating airfoil and estimation of lift from wake surveys. *Journal of Fluid Mechanics*, *265*, 65–95.

Quantronix. (2011). *Quantronix Lasers Darwin-Duo product page.* Available from http://www.quantronixlasers.com/index.php?option=com_content&view=article&id=350&Itemid=141

Raffel, M., Kompenhans, J., & Wernert, P. (1995). Investigation of the unsteady flow velocity field above an airfoil pitching under deep dynamic stall conditions. *Experiments in Fluids*, *19*(2). Available from http://www.springerlink.com/index/10.1007/BF00193856

Read, D. (2003, January). Forces on oscillating foils for propulsion and maneuvering. *Journal of Fluids and Structures*, *17*(1), 163–183.

Rival, D., & Tropea, C. (2010). Characteristics of Pitching and Plunging Airfoils Under Dynamic-Stall Conditions. *Journal of Aircraft*, *47*(1), 80–86. Available from http://doi.aiaa.org/10.2514/1.42528

Scarano, F. (2007). *Lecture notes on Experimental Aerodynamics.* Delft.

Theodorsen, T. (1934). *General theory of aerodynamic instability and the mechanism of flutter (NACA Technical Report No. 496)* (Tech. Rep.). NACA.

Tsang, K., So, R., Leung, R., & Wang, X. (2008). Dynamic stall behavior from unsteady force measurements. *Journal of Fluids and Structures*, *24*(1), 129–150. Available from http://linkinghub.elsevier.com/retrieve/pii/S0889974607001120

Unal, M. (1997, November). Force Prediction By Piv Imaging: a Momentum-Based Approach. *Journal of Fluids and Structures*, *11*(8), 965–971. Available from http://linkinghub.elsevier.com/retrieve/pii/S0889974697901110

Appendix A

Derivation of frequency response corrections

A.1 Frequency corrections of the force measurements

The equations of motion for the model are

$$\begin{aligned} m\ddot{x} &= L - F_T - F_B - R_a - R'_a \\ J\ddot{\theta} &= \frac{b}{2}F_T - \frac{b}{2}F_B - \left(\frac{b}{2}+d\right)R_a - \left(\frac{b}{2}+d\right)R'_a \end{aligned}$$

The forces $F_{T,B}$ are the forces acting between the aerofoil axis and the force transfering plates. These forces can be divided into three components:

- inertial forces of the transfer plates, $m_{T,B}\ddot{x}_{T,D}$
- gravitational effect on the perturbed situation, $\frac{m_{T,B}g}{\ell}x_{T,B}$
- spring force from the load cells, $kx_{T,B}$ (which is the actual force measured with the load cells)

This way the forces $F_{T,B}$ can be transformed into terms of displacements and accelerations

$$\begin{aligned} F_T &= m_T\ddot{x}_T + \frac{m_T g}{\ell}x_T + kx_T \\ F_B &= m_B\ddot{x}_B - \frac{m_B g}{\ell}x_B + kx_B \end{aligned}$$

Another term that can be transformed into an acceleration, is the inertial force of the mass of the actuator connection

$$R'_a = m_a\ddot{x}_a$$

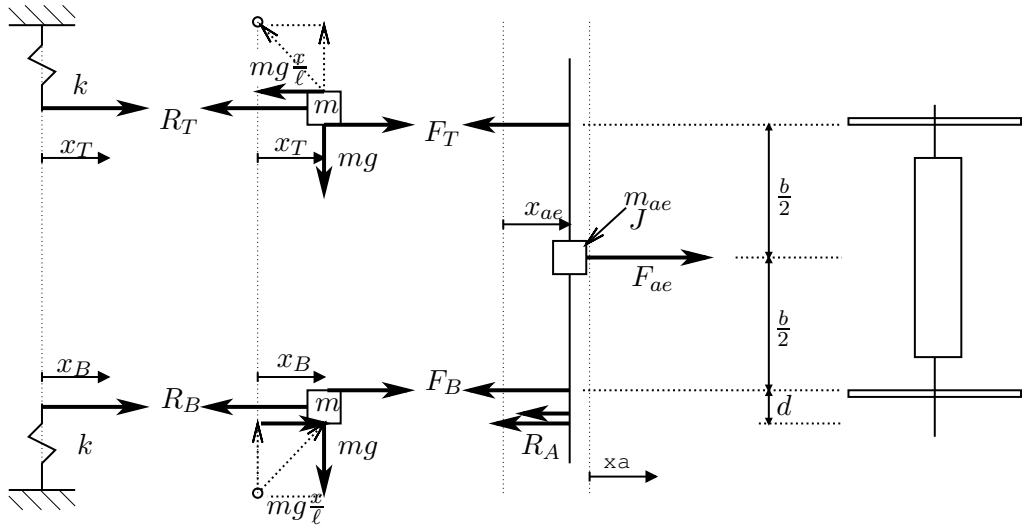

Figure A.1: Visual representation of the mass-spring model used for the dynamic response correction.

The equations of motion can now be written in terms of displacements

$$\begin{aligned} m\ddot{x} &= L - \left(m_T\ddot{x}_T + \frac{m_T g}{\ell}x_T + kx_T\right) - \left(m_B\ddot{x}_B - \frac{m_B g}{\ell}x_B + kx_B\right) - R_a - m_a\ddot{x}_a \\ J\ddot{\theta} &= \frac{b}{2}\left(m_T\ddot{x}_T + \frac{m_T g}{\ell}x_T + kx_T\right) - \frac{b}{2}\left(m_B\ddot{x}_B - \frac{m_B g}{\ell}x_B + kx_B\right) \\ &\quad - \left(\frac{b}{2}+d\right)R_a - \left(\frac{b}{2}+d\right)m_a\ddot{x}_a \end{aligned}$$

Now to relate the three displacements x_T, x_B and x_a can be related to the displacement (x) and rotation (θ) of the centre of gravity of the aerofoil by assuming a rigid axis

$$\begin{aligned} x_T &= x - \frac{b}{2}\theta \\ x_B &= x + \frac{b}{2}\theta \\ x_a &= x + \left(\frac{b}{2}+d\right)\theta \end{aligned}$$

Inserting these into the equations of motion gives

$$\begin{aligned} m\ddot{x} &= L - \left(m_T\left(\ddot{x} - \frac{b}{2}\ddot{\theta}\right) + \left(k + \frac{m_T g}{\ell}\right)\left(x - \frac{b}{2}\theta\right)\right)\ldots \\ &\quad - \left(m_B\left(\ddot{x} + \frac{b}{2}\ddot{\theta}\right) + \left(k - \frac{m_B g}{\ell}\right)\left(x + \frac{b}{2}\theta\right)\right) - R_a - m_a\left(\ddot{x} + \left(\frac{b}{2}+d\right)\ddot{\theta}\right) \\ J\ddot{\theta} &= \frac{b}{2}\left(m_T\left(\ddot{x} - \frac{b}{2}\ddot{\theta}\right) + \left(k + \frac{m_T g}{\ell}\right)\left(x - \frac{b}{2}\theta\right)\right)\ldots \\ &\quad - \frac{b}{2}\left(m_B\left(\ddot{x} + \frac{b}{2}\ddot{\theta}\right) + \left(k - \frac{m_B g}{\ell}\right)\left(x + \frac{b}{2}\theta\right)\right) - \left(\frac{b}{2}+d\right)R_a \\ &\quad - \left(\frac{b}{2}+d\right)m_a\left(\ddot{x} + \left(\frac{b}{2}+d\right)\ddot{\theta}\right) \end{aligned}$$

Rearranging the equations in such a way that the displacements are on the left hand side and the forces L and R_a on the right hand side

$$\begin{aligned} m\ddot{x} + m_T\left(\ddot{x} - \frac{b}{2}\ddot{\theta}\right) + m_B\left(\ddot{x} + \frac{b}{2}\ddot{\theta}\right) + m_a\left(\ddot{x} + \left(\frac{b}{2}+d\right)\ddot{\theta}\right) & \\ + \left(k + \frac{m_T g}{\ell}\right)\left(x - \frac{b}{2}\theta\right) + \left(k - \frac{m_B g}{\ell}\right)\left(x + \frac{b}{2}\theta\right) &= L - R_a \\ J\ddot{\theta} - \frac{b}{2}m_T\left(\ddot{x} - \frac{b}{2}\ddot{\theta}\right) + \frac{b}{2}m_B\left(\ddot{x} + \frac{b}{2}\ddot{\theta}\right) + \left(\frac{b}{2}+d\right)m_a\left(\ddot{x} + \left(\frac{b}{2}+d\right)\ddot{\theta}\right) & \\ - \frac{b}{2}\left(k + \frac{m_T g}{\ell}\right)\left(x - \frac{b}{2}\theta\right) + \frac{b}{2}\left(k - \frac{m_B g}{\ell}\right)\left(x + \frac{b}{2}\theta\right) &= -\left(\frac{b}{2}+d\right)R_a \end{aligned}$$

A mass matrix $[\mathbf{M}]$ and stiffness matrix $[\mathbf{K}]$ can now be identified

$$[\mathbf{M}]\left\{\begin{array}{c}\ddot{x}\\ \ddot{\theta}\end{array}\right\} + [\mathbf{K}]\left\{\begin{array}{c}x\\ \theta\end{array}\right\} = \left\{\begin{array}{c}L - R_a\\ -\left(\frac{b}{2}+d\right)R_a\end{array}\right\}$$

where the components of the mass matrix are

$$\begin{aligned} M_{1,1} &= m + m_T + m_B + m_a &&\rightarrow\quad m + 2m_{T,B} + m_a \\ M_{1,2} &= -\frac{b}{2}m_T + \frac{b}{2}m_B + \left(\frac{b}{2}+d\right)m_a &&\rightarrow\quad \left(\frac{b}{2}+d\right)m_a \\ M_{2,1} &= -\frac{b}{2}m_T + \frac{b}{2}m_B + \left(\frac{b}{2}+d\right)m_a &&\rightarrow\quad \left(\frac{b}{2}+d\right)m_a \\ M_{2,2} &= J + \frac{b^2}{4}m_T + \frac{b^2}{4}m_B + \left(\frac{b}{2}+d\right)^2 m_a &&\rightarrow\quad J + \frac{b^2}{2}m_{T,B} + \left(\frac{b}{2}+d\right)^2 m_a \end{aligned}$$

and the components of the stiffness matrix are

$$\begin{aligned} K_{1,1} &= 2k + \frac{m_T g}{\ell} - \frac{m_B g}{\ell} &&\rightarrow\quad 2k \\ K_{1,2} &= -\frac{b}{2}k - \frac{b}{2}\frac{m_T g}{\ell} + \frac{b}{2}k - \frac{b}{2}\frac{m_B g}{\ell} &&\rightarrow\quad -\frac{b m_{T,B} g}{\ell} \\ K_{2,1} &= -\frac{b}{2}k - \frac{b}{2}\frac{m_T g}{\ell} + \frac{b}{2}k - \frac{b}{2}\frac{m_B g}{\ell} &&\rightarrow\quad -\frac{b m_{T,B} g}{\ell} \\ K_{2,2} &= \frac{b^2}{4}k + \frac{b^2}{4}\frac{m_T g}{\ell} + \frac{b^2}{4}k - \frac{b^2}{4}\frac{m_B g}{\ell} &&\rightarrow\quad \frac{b^2}{2}k \end{aligned}$$

The eigenfrequencies of the system can be determined by solving the homogenious system, i.e. solving $\det\left(\mathbf{K} - \omega_n^2\mathbf{M}\right) = 0$. The resulting expressions are lengthy, but evaluation with the material properties, reveal eigenfrequencies of 30.4 and 31.0 Hz for two (coupled) modes for the aluminum aerofoil. For the Makrolon aerofoil these frequencies are 29.8 and 30.6 Hz.

The forced pitched motion of the aerofoil can be described by sum of sines or a Fourier series. The force response of the system is assumed to also follow a similar combined harmonic behaviour. The problem for each frequency of the Fourier series is

$$\left[\mathbf{K} - n^2\omega_a^2\mathbf{M}\right]\left\{\begin{array}{c}\hat{x}_n\\ \hat{\theta}_n\end{array}\right\} = \left\{\begin{array}{c}\hat{L}_n - \hat{R}_{a,n}\\ -\left(\frac{b}{2}+d\right)\hat{R}_{a,n}\end{array}\right\}$$

where ω_a is the actuation frequency (rad/s).

The required corrections should be of a form $[\mathbf{C}]\{\mathbf{R}\} = \{\mathbf{F}\}$, meaning that the measured forces multiplied by the correction give the actual force. To get to such a form, the displacements have to be transformed into the measured forces.

$$\begin{aligned} R_T &= kx_T = k\left(x - \frac{b}{2}\theta\right) \\ R_B &= kx_B = k\left(x + \frac{b}{2}\theta\right) \end{aligned}$$

This can be put into a transformation matrix $[\mathbf{R}]$ (not to be confused with the vector $\{\mathbf{R}\}$ which holds the forces themselves)

$$\begin{aligned} R_T + R_B &= 2kx \rightarrow x = \frac{R_T + R_B}{2k} \\ R_T - R_B &= -kb\theta \rightarrow \theta = \frac{R_B - R_T}{kb} \\ \left\{ \begin{array}{c} x \\ \theta \end{array} \right\} &= \underbrace{\left[\begin{array}{cc} \frac{1}{2k} & \frac{1}{2k} \\ -\frac{1}{kb} & \frac{1}{kb} \end{array} \right]}_{[\mathbf{R}]} \left\{ \begin{array}{c} R_T \\ R_B \end{array} \right\} \end{aligned}$$

The equations of motion can now be expressed as follows

$$\underbrace{\left[\mathbf{K} - n^2\omega_a^2\mathbf{M}\right] \cdot [\mathbf{R}]}_{[\mathbf{C}]} \left\{ \begin{array}{c} R_{T,n} \\ R_{B,n} \end{array} \right\} = \left\{ \begin{array}{c} L - R_a \\ -\left(\frac{b}{2} + d\right) R_a \end{array} \right\}$$

where the matrix on the left hand side can be identified as the correction matrix $[\mathbf{C}]$ having components

$$\begin{aligned} C_{1,1} &= 1 + \frac{mg}{k\ell} - \frac{1}{2}\frac{n^2\omega_a^2}{k/m_{ae}} - \frac{n^2\omega_a^2}{k/m} + \frac{d}{b}\frac{n^2\omega_a^2}{k/m_a} \\ C_{1,2} &= 1 - \frac{mg}{k\ell} - \frac{1}{2}\frac{n^2\omega_a^2}{k/m_{ae}} - \frac{n^2\omega_a^2}{k/m} - \frac{b+d}{b}\frac{n^2\omega_a^2}{k/m_a} \\ C_{2,1} &= -\frac{1}{2}b - \frac{1}{2}b\frac{mg}{k\ell} + b\frac{n^2\omega_a^2}{kb^2/J_{ae}} + \frac{1}{2}b\frac{n^2\omega_a^2}{k/m} + \frac{2d^2 + bd}{2b}\frac{n^2\omega_a^2}{k/m_a} \\ C_{2,2} &= \frac{1}{2}b - \frac{1}{2}b\frac{mg}{k\ell} - b\frac{n^2\omega_a^2}{kb^2/J_{ae}} - \frac{1}{2}b\frac{n^2\omega_a^2}{k/m} - \frac{b^2 + 3bd + 2d^2}{2b}\frac{n^2\omega_a^2}{k/m_a} \end{aligned}$$

The final goal is to find the aerodynamic force. The system can be solved for L, resulting in the expression $L = C_T R_T + C_B + R_B$

$$\begin{aligned} R_{a,n} &= -\left(\frac{b}{2} + d\right)^{-1} C_{2,1} R_{T.n} - \left(\frac{b}{2} + d\right)^{-1} C_{2,2} R_{B,n} \\ L_{a,n} &= C_{1,1} R_{T,n} + C_{1,2} R_{B,n} + R_{a,n} \\ &= \underbrace{\left(C_{1,1} - \left(\frac{b}{2} + d\right)^{-1} C_{2,1}\right)}_{C_T} R_{T,n} + \underbrace{\left(C_{1,2} - \left(\frac{b}{2} + d\right)^{-1} C_{2,2}\right)}_{C_B} R_{B,n} \end{aligned}$$

$$
\begin{aligned}
C_T &= \left(C_{1,1} - \left(\frac{b}{2}+d\right)^{-1} C_{2,1}\right) \\
&\quad \frac{2b+2d}{b+2d}\left(1 + \frac{mg}{k\ell} - \frac{n^2\omega_a^2}{k/m}\left(1 + \frac{1}{4}\frac{b+2d}{b+d}\frac{m_{ae}}{m} + \frac{b}{b+d}\frac{J_{ae}/b^2}{m}\right)\right) \\
C_B &= \left(C_{1,2} - \left(\frac{b}{2}+d\right)^{-1} C_{2,2}\right) \\
&= \frac{2d}{b+2d}\left(1 - \frac{mg}{k\ell} - \frac{n^2\omega_a^2}{k/m}\left(1 - \frac{b+2d}{d}\frac{m_{ae}}{m} - \frac{b}{d}\frac{J_{ae}/b^2}{m}\right)\right)
\end{aligned}
$$

A.2 Modelling axis twisting including damping

$$\ddot{\alpha}_r + 2\zeta\omega_n\dot{\alpha}_r + \omega_n^2\alpha_r = 2\zeta\omega_n\dot{\alpha}_a + \omega_n^2\alpha_a$$

Assuming form homogeneous solution $\alpha_h \propto e^{\lambda t}$:

$$
\begin{aligned}
\lambda^2 + 2\zeta\omega_n\lambda + \omega_n^2 &= 0 \\
\lambda_{1,2} &= -\zeta\omega_n \pm \omega_n\sqrt{\zeta^2-1} \\
\alpha_h(t) &= e^{-\zeta\omega_n t}\left(Ae^{-\omega_n\sqrt{\zeta^2-1}t} + Be^{\omega_n\sqrt{\zeta^2-1}t}\right)
\end{aligned}
$$

For under damped systems $\sqrt{\zeta^2-1}$ is complex. Defining $\omega_d = \omega_n\sqrt{1-\zeta^2}$,

$$\lambda_{1,2} = -\zeta\omega_n \pm i\omega_d$$

The homogeneous solution can thus be written as

$$
\begin{aligned}
\alpha_h(t) &= e^{-\zeta\omega_n t}\left(Ae^{-i\omega_d t} + Be^{i\omega_d t}\right) \text{ which is harmonic, so} \\
\alpha_h(t) &= e^{-\zeta\omega_n t}\left(A'\cos\omega_d t + B'\sin\omega_d t\right) \\
\text{or } \alpha_h(t) &= e^{-\zeta\omega_n t}\sin\left(\omega_d t + \phi\right), \text{ with } \phi = \arctan\frac{A'}{B'}
\end{aligned}
$$

Now for the particular solution again assuming a motion described by a Fourier series

$$
\begin{aligned}
\ddot{\alpha}_p + 2\zeta\omega_n\dot{\alpha}_p + \omega_n^2\alpha_p &= 2\zeta\omega_n\dot{\alpha}_a + \omega_n^2\alpha_a \\
\alpha_a &= a_0 + \sum_{n=1}^{k} a_n\cos n\omega_a t + b_n\sin n\omega_a t \\
\dot{\alpha}_a &= -\omega_a\sum_{n=1}^{k} n a_n\sin n\omega_a t - n b_n\cos n\omega_a t
\end{aligned}
$$

Table A.1: Fitted eigenfrequencies and damping ratios.

session	f_n (Hz)	f_n^d (Hz)	ζ^d	φ_{base} (ms)	comment
10Hz_15m-s_run1	52.9			0	
10Hz_15m-s_run2	60.9			−11.7	
20Hz_15m-s_run1	48.7	48.4	0.0395	6.5	poor fit...
20Hz_15m-2_run2	49.0	48.5	0.0439	3.5	poor fit...

The particular solution can be expressed as

$$\begin{aligned}
\alpha_p(t) &= a_0 + \sum_{n=1}^{k} A_n \cos n\omega_a t + B_n \sin n\omega_a t, \text{ with} \\
A_n &= \frac{1}{1+(nr)^4+\left(4\zeta^2-2\right)(nr)^2}\left[\left(1+\left(4\zeta^2-1\right)(nr)^2\right)a_n - 2\zeta(nr)^3 b_n\right] \\
B_n &= \frac{1}{1+(nr)^4+\left(4\zeta^2-2\right)(nr)^2}\left[2\zeta(nr)^3 a_n + \left(1+\left(4\zeta^2-1\right)(nr)^2\right)b_n\right] \\
r &= \frac{\omega_a}{\omega_n}
\end{aligned}$$

If this function can be fitted to the pitch angle data obtained from PIV, the damping and eigenfrequency might be determined relating the angle of attack measured at the base to the angle of attack at the aerofoil. However, the damping coefficient ζ introduces a phaseshift. Then the problem of the unreliable synchronisation of the pitch angle measurement at the base comes in again, which also introduces a phaseshift (this one however is varying between measurements, while the damping should be constant).

In table A.1 the results of curve fitting with the above expressions is shown. In the column labelled f_n the results by assuming zero damping are shown. The next two columns show the eigenfrequencies and damping coefficients obtained using the full expression. The column labelled φ_{base} notes the amount of time delay that was added to synchronise the base excitation with the PIV data. To eliminate the arbitrary inserting of time delays, the phase shift can be eliminated by rewriting the combination of sines and cosines to sines with a phase angle:

$$\begin{aligned}
\alpha_p(t) &= a_0 + \sum_{n=1}^{k} C_n \sin\left(n\omega_a t + \phi_n\right) \\
C_n &= \sqrt{A_n^2 + B_n^2} \\
&= \sqrt{\frac{4(nr)^2\zeta^2+1}{1+(nr)^4+\left(4\zeta^2-2\right)(nr)^2}}\underbrace{\sqrt{a_n^2+b_n^2}}_{c_n}, \text{ with } c_n \text{being the amplitude of the actuation...} \\
\phi_n &= \arctan\left(\frac{A_n}{B_n}\right) + \begin{cases} 0 & B_n \geq 0 \\ \pi & B_n < 0 \end{cases}
\end{aligned}$$

This way the amplitude and phase can be separated for each mode. It follows that each mode of the base excitation can be multiplied by a specific amplification factor to get to

the response amplitude for that mode. The response amplitude obtained from PIV can be described by a third order Fourier series, so from that C_n can be determined. For the same cases also the excitation amplitude is measured, which can also be described by the same order Fourier series.

20Hz_15m-s_run1

n	$\sqrt{A_n^2 + B_n^2}$	$\sqrt{a_n^2 + b_n^2}$	C_n/c_n
1	12.44	10.92	1.139
2	3.993	1.207	3.310
3	0.3844	0.1508	2.550

Using this method the results do not get much better: the obtained eigenfrequencies still range from 40 to 50 Hz. It does seem that the damping is either zero or close to 0.1.

Appendix B

Coefficient tables

B.1 XFoil static coefficients

B.1.1 XFOIL coefficients of the NACA0018 aerofoil for Reynolds numbers 83k to 166k

Re	83,000		110,000		139,000		166,000	
α (deg)	C_L	C_D	C_L	C_D	C_L	C_D	C_L	C_D
0.0	0.0000	0.02516	0.0000	0.01848	0.0000	0.01516	0.0000	0.01336
0.5	0.1051	0.02502	0.0632	0.01873	0.0552	0.01522	0.0535	0.01341
1.0	0.1919	0.02502	0.1344	0.01896	0.1128	0.01550	0.1070	0.01360
1.5	0.2727	0.02479	0.2026	0.01937	0.1692	0.01582	0.1608	0.01387
2.0	0.3648	0.02458	0.2776	0.01978	0.2293	0.01628	0.2183	0.01431
2.5	0.4531	0.02438	0.3617	0.02015	0.2980	0.01683	0.2794	0.01483
3.0	0.5337	0.0242	0.4419	0.02043	0.3719	0.01739	0.3449	0.01538
3.5	0.6285	0.02379	0.5199	0.02067	0.4512	0.01788	0.4165	0.01595
4.0	0.7033	0.02351	0.6072	0.02084	0.5372	0.01834	0.4941	0.01651
4.5	0.7384	0.02362	0.6949	0.02091	0.6163	0.01873	0.5716	0.01704
5.0	0.7714	0.02396	0.7767	0.02098	0.6991	0.01909	0.6499	0.01754
5.5	0.8066	0.02436	0.8098	0.02127	0.7853	0.01938	0.7304	0.01801
6.0	0.8376	0.02495	0.8426	0.02174	0.8458	0.01975	0.8129	0.01847
6.5	0.8701	0.02567	0.8731	0.02229	0.8762	0.02021	0.8804	0.01893
7.0	0.8969	0.02659	0.9035	0.02302	0.9051	0.02086	0.9084	0.01950
7.5	0.9269	0.02755	0.9290	0.02386	0.9310	0.02154	0.9344	0.02016
8.0	0.9534	0.02881	0.9537	0.02481	0.9544	0.02235	0.9573	0.02088
8.5	0.9762	0.0302	0.9777	0.02587	0.9757	0.02328	0.9771	0.02170
9.0	0.9996	0.03172	1.0012	0.02707	0.9956	0.02430	0.9944	0.02262
9.5	1.0229	0.03343	1.0241	0.02840	1.0144	0.02542	1.0101	0.02363
10.0	1.0456	0.03536	1.0461	0.02986	1.0331	0.02667	1.0252	0.02476

B.2 Experimentally determined lift and drag coefficients

In the following sections the results of the measurements are tabulated. The values in brackets indicate the root-mean-square of the fluctuations around the mean. This includes measurement errors as well as actual fluctuations of the flow.

B.2.1 Mechanical balance experiments NACA0018 aerofoil

Tabulated results of the force measurements performed with the aluminium aerofoil. For these measurements a sample rate of 5 kHz was used and a measurement time of 5 seconds, so the values are averaged over 25 000 samples.

Re	28 000 (5 m/s)			
α (deg)	C_L		C_D	
-9.17	-0.1695	(0.0550)	0.2039	(0.0293)
-8.20	-0.1507	(0.0469)	0.1976	(0.0306)
-7.09	-0.1354	(0.0519)	0.2001	(0.0253)
-6.21	-0.0825	(0.0522)	0.1791	(0.0403)
-4.06	-0.0139	(0.0531)	0.1470	(0.0231)
-3.06	-0.0002	(0.0464)	0.1447	(0.0255)
-2.06	-0.0123	(0.0340)	0.1379	(0.0296)
-1.04	0.0405	(0.0260)	0.1406	(0.0227)
-0.00	-0.0280	(0.0272)	0.1372	(0.0175)
1.14	-0.0406	(0.0271)	0.1397	(0.0211)
2.12	-0.0356	(0.0274)	0.1334	(0.0215)
2.93	-0.0041	(0.0281)	0.1423	(0.0223)
4*	0.0538	(0.0325)	0.1456	(0.0185)
5.24	0.1091	(0.0503)	0.1581	(0.0208)
6.15	0.1304	(0.0352)	0.1591	(0.0186)
7.33	0.1572	(0.0425)	0.1782	(0.0195)
8.15	0.1795	(0.0365)	0.1868	(0.0205)
9.26	0.2279	(0.0569)	0.1980	(0.0198)
10.34	0.2443	(0.0532)	0.2117	(0.0228)

*incorrect measurement of angle

Re	55 000 (10 m/s)			
α (deg)	C_L		C_D	
-10.13	-0.8166	(0.0335)	0.0565	(0.0249)
-9.15	-0.7945	(0.0407)	0.0364	(0.0244)
-8.20	-0.7462	(0.0516)	0.0537	(0.0300)
-7.09	-0.7023	(0.0435)	0.0613	(0.0227)
-6.21	-0.6537	(0.0394)	0.0700	(0.0251)
-4.07	-0.5438	(0.0410)	0.0560	(0.0208)
-3.06	-0.4840	(0.0440)	0.0523	(0.0259)

Re	55 000 (10 m/s)			
α (deg)	C_L		C_D	
-2.06	-0.4087	(0.0513)	0.0496	(0.0274)
-1.04	-0.2082	(0.0393)	0.0405	(0.0230)
-0.00	-0.0524	(0.0475)	0.0497	(0.0236)
1.14	0.2306	(0.0518)	0.0503	(0.0232)
2.06	0.3087	(0.0355)	0.0431	(0.0267)
2.94	0.5285	(0.0339)	0.0535	(0.0271)
4*	0.5600	(0.0332)	0.0575	(0.0261)
5.24	0.6331	(0.0315)	0.0618	(0.0304)
6.14	0.6888	(0.0292)	0.0658	(0.0294)
7.36	0.7345	(0.0326)	0.0670	(0.0239)
8.18	0.7805	(0.0355)	0.0629	(0.0277)
9.27	0.4457	(0.0864)	0.1153	(0.0353)
10.35	0.3945	(0.0707)	0.1315	(0.0409)

*incorrect measurement of angle

Re	80 000 (15 m/s)			
α (deg)	C_L		C_D	
-10.13	-0.8841	(0.0350)	0.0424	(0.0180)
-9.14	-0.8529	(0.0339)	0.0334	(0.0142)
-8.18	-0.8074	(0.0284)	0.0268	(0.0187)
-7.09	-0.7537	(0.0351)	0.0233	(0.0181)
-6.17	-0.6843	(0.0280)	0.0237	(0.0164)
-4.05	-0.4400	(0.0423)	0.0204	(0.0162)
-3.09	-0.3082	(0.0486)	0.0214	(0.0180)
-2.06	-0.1489	(0.0294)	0.0271	(0.0156)
-1.05	-0.0472	(0.0325)	0.0275	(0.0166)
-0.00	0.0285	(0.0371)	0.0292	(0.0134)
1.15	0.1174	(0.0304)	0.0300	(0.0177)
2.02	0.2082	(0.0319)	0.0271	(0.0151)
2.99	0.3502	(0.0382)	0.0295	(0.0150)
4*	0.4600	(0.0272)	0.0303	(0.0161)
5.23	0.5923	(0.0305)	0.0442	(0.0159)
6.14	0.6931	(0.0413)	0.0413	(0.0124)
7.33	0.7667	(0.0318)	0.0482	(0.0163)
8.17	0.8097	(0.0360)	0.0529	(0.0156)
9.26	0.8516	(0.0262)	0.0567	(0.0176)
10.33	0.8885	(0.0335)	0.0622	(0.0122)

*incorrect measurement of angle

Re	110 000 (20 m/s)			
α (deg)	C_L		C_D	
-10.13	-0.9029	(0.0358)	0.0360	(0.0139)
-9.18	-0.8685	(0.0246)	0.0305	(0.0138)
-8.18	-0.8215	(0.0250)	0.0245	(0.0147)
-7.09	-0.7332	(0.0251)	0.0197	(0.0134)
-6.17	-0.6240	(0.0254)	0.0145	(0.0170)
-4.04	-0.3689	(0.0276)	0.0018	(0.0137)
-3.08	-0.2523	(0.0244)	0.0030	(0.0153)
-2.06	-0.1379	(0.0235)	0.0112	(0.0131)
-1.05	-0.0358	(0.0237)	0.0180	(0.0147)
0.01	0.0338	(0.0246)	0.0197	(0.0119)
1.17	0.1209	(0.0267)	0.0171	(0.0205)
2.04	0.2042	(0.0228)	0.0110	(0.0159)
2.94	0.2990	(0.0267)	0.0163	(0.0143)
4*	0.4090	(0.0277)	0.0224	(0.0138)
5.19	0.5137	(0.0246)	0.0321	(0.0148)
6.09	0.6356	(0.0245)	0.0362	(0.0146)
7.33	0.7515	(0.0229)	0.0451	(0.0132)
8.19	0.8181	(0.0260)	0.0505	(0.0135)
9.29	0.8617	(0.0268)	0.0542	(0.0137)
10.30	0.9059	(0.0290)	0.0608	(0.0149)

*incorrect measurement of angle

Re	138 000 (25 m/s)			
α (deg)	C_L		C_D	
-10.15	-0.9001	(0.0196)	0.0427	(0.0139)
-9.19	-0.8703	(0.0174)	0.0375	(0.0167)
-8.20	-0.8050	(0.0195)	0.0303	(0.0146)
-7.10	-0.7067	(0.0199)	0.0241	(0.0166)
-6.17	-0.5848	(0.0162)	0.0145	(0.0138)
-4.04	-0.3471	(0.0209)	0.0022	(0.0153)
-3.10	-0.2521	(0.0168)	0.0028	(0.0139)
-2.06	-0.1608	(0.0187)	0.0069	(0.0156)
-1.05	-0.0605	(0.0303)	0.0152	(0.0157)
-0.00	0.0312	(0.0263)	0.0189	(0.0165)
1.14	0.1359	(0.0223)	0.0133	(0.0148)
2.15	0.2142	(0.0292)	0.0145	(0.0151)
2.99	0.2859	(0.0326)	0.0184	(0.0162)
4*	0.3784	(0.0219)	0.0220	(0.0147)
5.07	0.4816	(0.0239)	0.0282	(0.0153)
6.02	0.6066	(0.0283)	0.0354	(0.0177)
7.34	0.7216	(0.0179)	0.0447	(0.0146)
8.27	0.8262	(0.0271)	0.0517	(0.0170)

Re	138 000 (25 m/s)			
α (deg)	C_L		C_D	
9.37	0.8805	(0.0201)	0.0570	(0.0180)
10.46	0.9232	(0.0217)	0.0623	(0.0155)

*incorrect measurement of angle

Re	166 000 (30 m/s)			
α (deg)	C_L		C_D	
-10.15	-0.9020	(0.0149)	0.0436	(0.0097)
-9.22	-0.8497	(0.0159)	0.0388	(0.0137)
-8.23	-0.7583	(0.0143)	0.0292	(0.0115)
-7.11	-0.6562	(0.0155)	0.0219	(0.0136)
-6.19	-0.5403	(0.0173)	0.0142	(0.0115)
-4.04	-0.3493	(0.0148)	0.0029	(0.0122)
-3.09	-0.2627	(0.0190)	0.0028	(0.0152)
-2.06	-0.1735	(0.0174)	0.0029	(0.0106)
-1.05	-0.0780	(0.0148)	0.0124	(0.0171)
-0.00	0.0326	(0.0172)	0.0163	(0.0114)
1.17	0.1378	(0.0145)	0.0120	(0.0140)
2.25	0.2139	(0.0136)	0.0134	(0.0102)
3.10	0.2932	(0.0188)	0.0147	(0.0125)
4*	0.3694	(0.0182)	0.0179	(0.0113)
6.23	0.5812	(0.0142)	0.0323	(0.0105)
7.32	0.6995	(0.0160)	0.0433	(0.0098)
8.25	0.8124	(0.0152)	0.0512	(0.0092)
9.46	0.8923	(0.0160)	0.0588	(0.0088)
10.43	0.9328	(0.0208)	0.0644	(0.0106)

*incorrect measurement of angle

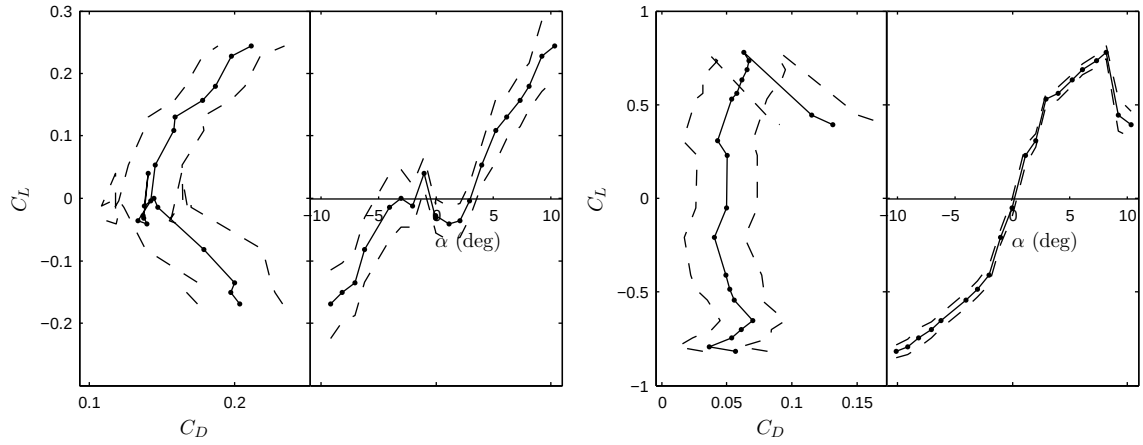

(a) Re 28 000 (5 m/s)

(b) Re 55 000 (10 m/s)

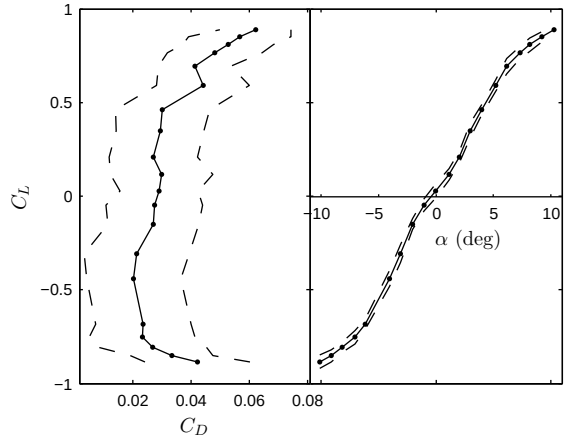

(c) Re 80 000 (15 m/s)

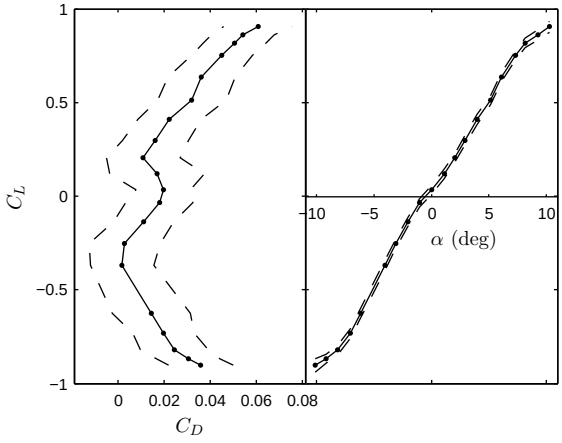

(d) Re 110 000 (20 m/s)

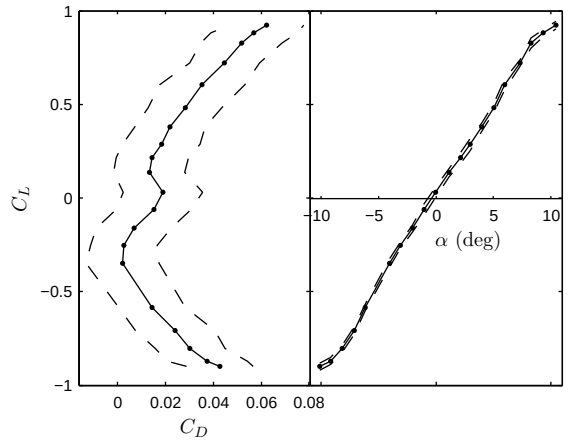

(e) Re 138 000 (25 m/s)

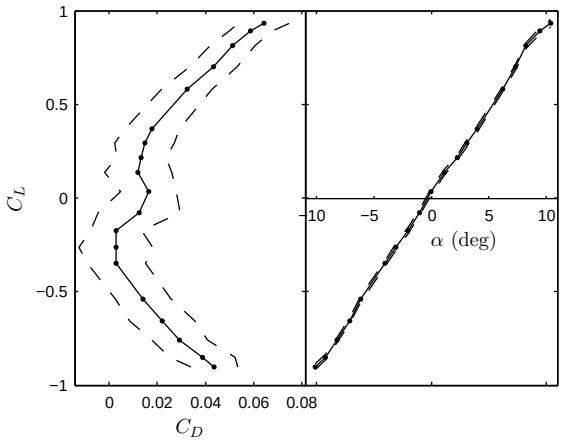

(f) Re 166,000 (30 m/s)

Figure B.1: Experimental lift and drag curves from balance measurements, aluminium aerofoil. The rms values of the instantaneous variations around the mean is indicated by the dashed lines.

B.2.2 PIV experiments with NACA0018 aerofoil

Tabulated results of the PIV measurements with the Makrolon aerofoil. A sample rate of 1 kHz was used with a sample time of one second. The results of three different methods are shown in three separate tables. The first two involve determining the forces from the integral momentum equation (2.2). These two differ by the method of determining the pressure on the contour. The first, Presure Gradient Integration, is obtained by first determining the pressure gradient field from the velocity and acceleration data and then integrating this gradient along the contour. For the second, the Bernoulli pressure method, the pressure is obtained by Bernoulli's equation $p = \frac{1}{2}\rho V^2$, which is known not to be valid for unsteady flows. The third table shows the results for the lift coefficient from using the Kutta-Joukowski law $\ell = -\rho V\Gamma$, where Γ is the bound circulation around an aerofoil section. This circulation is calculated by integration of the velocity component parallel to the contour along the contour in counter clockwise direction. Since this is a potential flow solution, there is no drag coefficient calculated.

Re	Pressure Gradient Integration			
α (deg)	C_L		C_D	
-10.343	-0.9063	(0.1812)	0.05734	(0.23302)
-5.269	-0.6092	(0.1991)	0.05997	(0.36686)
0.010	0.1144	(0.1629)	0.09777	(0.27087)
5.258	0.6932	(0.1705)	0.11920	(0.41021)
10.124	0.8655	(0.1725)	0.08278	(0.14086)

Re	Bernoulli pressure method			
α (deg)	C_L		C_D	
-10.343	-0.8054	(0.0179)	0.08033	(0.02164)
-5.269	-0.5418	(0.0232)	0.08528	(0.02292)
0.010	0.1167	(0.0264)	0.03602	(0.02690)
5.258	0.6291	(0.0310)	0.08440	(0.02029)
10.124	0.8588	(0.0167)	0.06970	(0.03472)

Re	Kutta-Joukowski ($C_L = 2\Gamma/U_\infty c$)	
α (deg)	C_L	
-10.343	-0.8024	(0.0155)
-5.269	-0.5378	(0.0234)
0.010	0.1152	(0.0237)
5.258	0.6255	(0.0275)
10.124	0.8510	(0.0135)

B.3 Experimentally determined lift coefficients oscillating aerofoil

The following table contains the experimental results obtained from the balance measurements on the aluminium aerofoil, expressed in maximum, minimum and mean lift coefficient values. Corresponding with this table, a table with the lift coefficient values obtained with Theodorsen's function is presented.

Re ($\times 10^3$)	V (m/s)	k	f (Hz)	$C_{L,\max}$	$C_{L,\min}$	$C_{L,\text{mean}}$	t' (ms)	($\pm\sigma$)
27	5.0	0.150	3	0.58	-0.69	0.02	-19.08	(4.20)
26	5.0	0.200	4	0.78	-0.83	0.02	-13.89	(1.26)
26	5.0	0.301	6	1.24	-1.11	0.09	6.06	(5.49)
27	5.1	0.348	7	0.70	-1.34	-0.29	2.89	(-)
26	5.0	0.452	9	1.29	-1.54	-0.11	-3.37	(5.22)
26	5.0	0.600	12	1.62	-3.84	-0.04	5.39	(6.18)
26	5.0	0.748	15	1.29	-1.56	-0.10	-2.56	(6.70)
26	5.0	0.897	18	4.06	-4.42	-0.06	-4.94	(6.58)
26	5.1	0.994	20	3.08	-2.71	0.28	-6.06	(3.68)
53	10.1	0.075	3	0.88	-0.87	0.01	4.71	(6.93)
53	10.1	0.100	4	0.81	-0.77	-0.02	0.00	(2.53)
53	10.1	0.150	6	0.87	-0.90	-0.02	-1.35	(1.26)
53	10.1	0.174	7	0.77	-0.89	-0.08	-7.22	(5.77)
52	10.1	0.225	9	1.51	-1.47	-0.04	-9.65	(6.61)
52	10.1	0.300	12	1.10	-1.11	-0.01	0.51	(3.47)
52	10.1	0.374	15	0.91	-0.96	0.01	-1.48	(3.70)
52	10.1	0.450	18	1.72	-1.74	0.01	-6.85	(5.12)
52	10.0	0.501	20	1.86	-1.83	0.06	-2.40	(4.69)
79	15.0	0.050	3	0.98	-0.98	0.02	-3.37	(4.76)
79	15.0	0.067	4	1.02	-0.97	0.03	-5.05	(2.53)
79	15.1	0.100	6	1.05	-1.04	0.02	0.34	(2.47)
79	15.0	0.117	7	1.01	-1.01	0.00	0.72	(3.61)
78	15.0	0.150	9	1.40	-1.25	0.01	-3.59	(9.48)
78	15.0	0.201	12	1.33	-1.24	0.01	2.36	(2.68)
78	15.1	0.250	15	0.83	-0.79	0.02	2.29	(3.65)
77	15.0	0.301	18	1.46	-1.39	0.04	-3.59	(4.94)
78	15.0	0.334	20	1.69	-1.63	0.04	0.13	(2.56)
106	20.0	0.038	3	0.99	-0.99	0.02	-4.71	(5.04)
105	20.1	0.050	4	1.02	-0.99	0.04	-	(-)
106	20.1	0.075	6	1.06	-1.04	0.03	0.34	(5.15)
105	20.1	0.088	7	1.05	-1.04	0.02	-0.72	(2.16)
102	19.7	0.115	9	1.43	-1.27	0.02	0.22	(9.40)
104	20.1	0.150	12	1.66	-1.36	0.04	-5.56	(4.54)
103	20.1	0.188	15	0.89	-0.91	0.03	5.12	(4.98)
103	20.1	0.225	18	1.48	-1.28	0.04	2.92	(14.43)
Re	V	k	f	$C_{L,\max}$	$C_{L,\min}$	$C_{L,\text{mean}}$	t'	($\pm\sigma$)

Re ($\times 10^3$)	V (m/s)	k	f (Hz)	$C_{L,\max}$	$C_{L,\min}$	$C_{L,\text{mean}}$	t' ($\pm\sigma$) (ms)	
104	20.1	0.250	20	1.37	-1.30	0.04	-4.80	(6.69)
132	25.0	0.030	3	1.01	-0.98	0.04	3.37	(2.13)
131	25.0	0.040	4	1.02	-0.99	0.03	2.53	(2.53)
132	25.0	0.060	6	1.06	-1.04	0.04	-8.42	(3.53)
131	25.1	0.070	7	1.08	-1.04	0.03	-2.89	(1.44)
130	25.0	0.090	9	1.31	-1.14	0.03	-2.69	(5.71)
130	25.0	0.120	12	1.85	-1.39	0.04	7.07	(3.39)
129	25.1	0.150	15	1.01	-0.97	0.04	2.83	(1.50)
129	25.0	0.181	18	1.63	-1.32	0.05	-4.94	(4.40)
130	25.0	0.201	20	1.64	-1.56	0.05	1.26	(3.82)
158	30.0	0.025	3	1.02	-0.97	0.04	4.71	(4.57)
157	30.0	0.034	4	1.03	-0.98	0.04	5.05	(5.05)
158	30.0	0.050	6	1.07	-1.03	0.04	-2.36	(5.28)
157	30.1	0.058	7	1.10	-1.02	0.04	5.77	(4.33)
155	30.0	0.076	9	1.33	-1.11	0.03	2.24	(3.69)
155	30.0	0.101	12	1.75	-1.21	0.03	2.36	(7.78)
154	30.0	0.125	15	1.05	-1.02	0.04	-1.35	(2.89)
155	30.0	0.151	18	1.67	-1.36	0.05	1.68	(10.78)
156	30.0	0.167	20	1.61	-1.56	0.04	-3.16	(3.56)
Re	V	k	f	$C_{L,\max}$	$C_{L,\min}$	$C_{L,\text{mean}}$	t' ($\pm\sigma$)	

The following tabulated data represents the lift coefficients obtained with Theodorsen's function based on the aerofoil motion observed for each measurement. The data correspond to the results in the previous table with the lift coefficients obtained from the balance measurements.

Re ($\times 10^3$)	V (m/s)	k	f (Hz)	$C_{L,\max}^{\text{Theo.}}$	$C_{L,\min}^{\text{Theo.}}$	$C_{L,\text{mean}}^{\text{Theo.}}$	t' (ms)
27	5.0	0.150	3	0.89	-0.90	-0.01	6.25
26	5.0	0.200	4	0.89	-0.83	0.01	1.42
26	5.0	0.301	6	0.82	-0.80	-0.00	-1.91
27	5.1	0.348	7	0.83	-0.78	0.01	-3.60
26	5.0	0.452	9	0.75	-0.87	-0.07	-3.67
26	5.0	0.600	12	0.89	-0.90	0.03	-7.47
26	5.0	0.748	15	0.97	-1.09	0.02	-7.88
26	5.0	0.897	18	1.03	-1.29	0.02	-7.40
26	5.1	0.994	20	0.90	-1.71	-0.23	-5.47
53	10.1	0.075	3	0.98	-1.02	-0.02	8.25
53	10.1	0.100	4	0.99	-0.95	0.01	4.69
53	10.1	0.150	6	0.92	-0.90	-0.00	2.90
53	10.1	0.174	7	0.90	-0.88	-0.00	2.02
52	10.1	0.225	9	0.80	-0.90	-0.07	2.03
Re	V	k	f	$C_{L,\max}^{\text{Theo.}}$	$C_{L,\min}^{\text{Theo.}}$	$C_{L,\text{mean}}^{\text{Theo.}}$	t'

Re ($\times 10^3$)	V (m/s)	k	f (Hz)	$C_{L,\max}^{\text{Theo.}}$	$C_{L,\min}^{\text{Theo.}}$	$C_{L,\text{mean}}^{\text{Theo.}}$	t' (ms)
52	10.1	0.300	12	0.88	-0.80	0.03	-1.37
52	10.1	0.374	15	0.89	-0.82	0.03	-2.30
52	10.1	0.450	18	0.98	-0.78	0.11	-3.78
52	10.0	0.501	20	0.67	-1.16	-0.23	-0.43
79	15.0	0.050	3	1.04	-1.07	-0.01	7.35
79	15.0	0.067	4	1.04	-1.01	0.02	4.65
79	15.1	0.100	6	0.98	-0.98	-0.01	3.76
79	15.0	0.117	7	0.97	-0.95	0.00	2.90
78	15.0	0.150	9	0.87	-0.97	-0.06	3.15
78	15.0	0.201	12	0.94	-0.85	0.03	0.33
78	15.1	0.250	15	0.92	-0.85	0.02	-0.30
77	15.0	0.301	18	1.01	-0.74	0.11	27.96
78	15.0	0.334	20	0.63	-1.09	-0.24	-28.15
106	20.0	0.038	3	1.07	-1.09	-0.01	6.50
105	20.1	0.050	4	1.07	-1.05	0.01	4.52
106	20.1	0.075	6	1.01	-1.03	-0.01	3.99
105	20.1	0.088	7	0.99	-1.02	-0.02	3.60
102	19.7	0.115	9	0.92	-1.01	-0.06	3.45
104	20.1	0.150	12	0.98	-0.91	0.03	1.03
103	20.1	0.188	15	0.96	-0.90	0.02	0.57
103	20.1	0.225	18	1.04	-0.79	0.10	28.74
104	20.1	0.250	20	0.65	-1.13	-0.25	-27.43
132	25.0	0.030	3	1.09	-1.10	0.00	5.63
131	25.0	0.040	4	1.08	-1.09	-0.00	4.73
132	25.0	0.060	6	1.04	-1.05	-0.01	3.73
131	25.1	0.070	7	1.02	-1.05	-0.02	3.48
130	25.0	0.090	9	0.96	-1.05	-0.06	3.44
130	25.0	0.120	12	1.02	-0.96	0.03	1.32
129	25.1	0.150	15	1.00	-0.94	0.02	0.95
129	25.0	0.181	18	1.06	-0.83	0.10	29.17
130	25.0	0.201	20	0.69	-1.18	-0.25	-26.88
158	30.0	0.025	3	1.10	-1.11	-0.00	5.37
157	30.0	0.034	4	1.09	-1.10	-0.00	4.46
158	30.0	0.050	6	1.07	-1.07	0.00	3.39
157	30.1	0.058	7	1.05	-1.06	-0.01	3.19
155	30.0	0.076	9	0.99	-1.07	-0.05	3.35
155	30.0	0.101	12	1.04	-0.99	0.02	1.47
154	30.0	0.125	15	1.04	-0.96	0.03	0.97
155	30.0	0.151	18	1.11	-0.86	0.11	29.53
156	30.0	0.167	20	0.72	-1.21	-0.25	-26.47
Re	V	k	f	$C_{L,\max}^{\text{Theo.}}$	$C_{L,\min}^{\text{Theo.}}$	$C_{L,\text{mean}}^{\text{Theo.}}$	t'